Imperial College London

TOPOLOGICAL PHYSICS IN ONE-DIMENSIONAL CHAINS OF METALLIC NANOPARTICLES

SIMON R POCOCK

Condensed Matter Theory Group
Department of Physics
Imperial College London

Thesis submitted in partial fulfillment for the degree of
Doctor of Philosophy

DECLARATION OF ORIGINALITY

All material presented in this thesis is my own work, except where otherwise noted.

— Simon R Pocock

COPYRIGHT DECLARATION

ABSTRACT

The focus of this thesis is the study of a chain of metal nanoparticles with alternating spacing, an artistic impression of which is given in figure 0.1. At first glance, this seems like a fairly simple system but, in reality, its study is a dive into two of the most exciting fields in modern condensed matter physics: topological insulators and light-matter interactions. In fact, the properties of light lead us to consider some of the most pressing questions in the field of topological insulators today.

The first half of the thesis covers all of the theory needed to understand the original work presented in the second half. The first chapter includes a historical review of topological insulators, an introduction to some of the fundamental concepts in the field, and an overview of photonic and non-Hermitian topological insulators. This is followed, in the second chapter, by a detailed discussion of the famous Su-Schrieffer-Heeger model and important results from the theory of scattering of light by nanoparticles.

In the remaining chapters, which make up the second half of the thesis, we present models for the chain which take into account the nature of light and result in a wealth of interesting topological physics. The polarisation of light affects the topology dramatically, with stable topology and protected plasmonic edge states in one polarisation and the complete breakdown of bulk-edge correspondence in another. The absorption of light and its phase properties force the system to be non-Hermitian. This, combined with the long range coupling of the metal nanoparticles, leads to unexpected topological phase transitions. These results are elaborated on in the following work, along with extinction cross sections of the chain, a non-Hermitian next-nearest-neighbour Su-Schrieffer-Heeger model extension, and a minimal model for the non-Hermitian phase transitions.

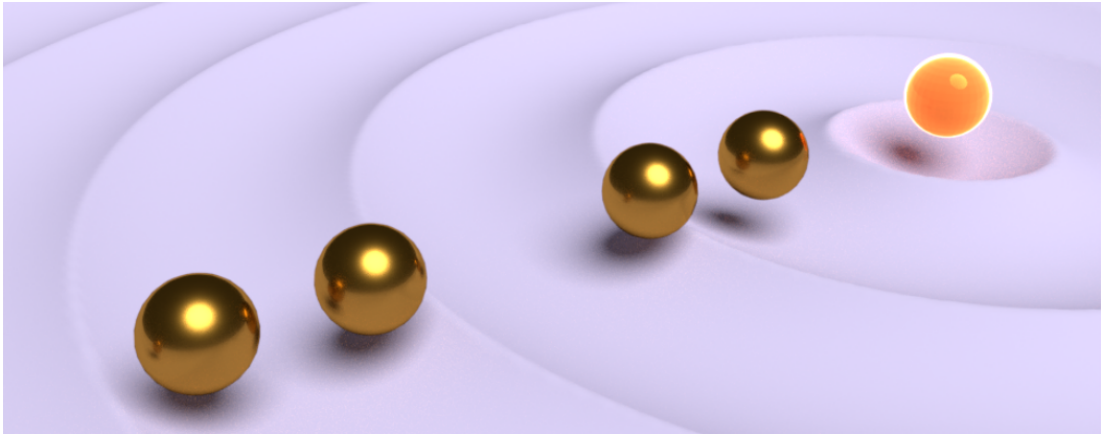

Figure 0.1: Artistic impression of the chain of metallic nanoparticles with a plasmonic edge mode, reproduced from [1]

ACKNOWLEDGEMENTS

I am not unique in having found my PhD an incredibly challenging experience, although perhaps for different reasons to most. Certainly, this thesis would not exist without the support of the many incredible people in my life, to whom I owe a great debt of gratitude. Including them here is a totally insufficient gesture towards its payment.

I would like to thank Vincenzo Giannini for being such a wonderful supervisor. Your insight and guidance have been invaluable over these four years, and your patience and positivity were always there when I needed them most. Every time we spoke, I found my doubts allayed and I stood a little taller. I am similarly grateful to Paloma A Huidobro for acting as a fantastic unofficial secondary supervisor for a large portion of my time at Imperial. Your wisdom and warmth were always a welcome addition to the day. My final academic thanks go to Simon Lieu, who influenced the path of my PhD for the better during our many discussions on topological insulators.

To all of my friends, thank you for being so brilliant. I consider myself very lucky to spend so much of my time with you. Those of you in CMTH feel like a second family to me, and made the office feel like home. I will always remember our long conversations in the common room, and I hope that we will find time to have many more. It was a pleasure to work alongside you. To everyone else, thank you so much for every little bit of help you gave me. Every evening spent together, every climbing trip, every meal, every pub quiz, every board or video game, every gig and band practice, every quiet word, every difficult conversation; these were all a kind of therapy to me, even if it didn't always seem like it at the time.

To my family, thank you for supporting me. Thank you for the phone calls when I was struggling, for the good advice, and for welcoming me home when the world was too much. My father is caring, wise, and an incredible source of strength; I have relied on these qualities for all of my life, especially this last handful of years. My mother was smart, compassionate, and unbelievably strong, and also my greatest cheerleader; she was always spurring me on to greater heights. Mum, I hope I can keep making you proud.

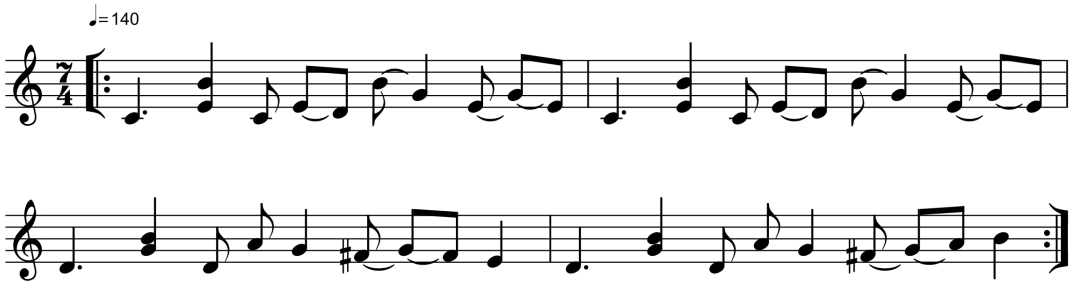

Figure 0.2: A short guitar piece for the people mentioned above

In loving memory of Susan Pocock

CONTENTS

LIST OF FIGURES

LIST OF TABLES

LIST OF ACRONYMS

AZ Altland-Zirnbauer

BEC Bulk-edge correspondence

BZ Brillouin Zone

CDE Coupled dipole equation

FDTD Finite Difference Time Domain

FEM Finite Element Method

FQHE Fractional Quantum Hall Effect

MLWA Modified long wavelength approximation

NNN Next nearest neighbour

ODE Ordinary different equation

PC Photonic crystal

PTI Photonic topological insulator

QAHE Quantum Anomalous Hall Effect

QHE Quantum Hall Effect

QS Quasistatic

QSHE Quantum Spin Hall Effect

SLS Sublattice symmetry

SPP Surface plasmon polariton

SPR Surface plasmon resonance

SSH Su-Schrieffer-Heeger

SVD Singular-value decomposition

TI Topological insulator

LIST OF SYMBOLS

a	Particle radius
α	Polarisability
β	Intracell spacing parameter
c	Speed of light
C	Chern number
C_{ext}	Extinction cross section
d	Unit cell spacing
E	Electric field
$\mathcal{E}$	Energies and Eigenvalues
$\epsilon(\omega)$	Dielectric function
ϵ_0	Free space permittivity
ϵ_∞	High frequency permittivity limit
ϵ_B	Relative background permittivity
G	Green's dyadic or function
$\mathcal{G}$	Hamiltonian of Green's functions
$\tilde{g}$	Reduced green's function
H, $\mathcal{H}$	Hamiltonians
k	Wavevector
λ	Wavelength
ω	Angular frequency
ω_P	Bulk plasmon frequency
ω_{sp}	Surface plasmon resonance frequency
$\Phi(z, s, \nu)$	Lerch transcendent
$\mathbf{p}$	Dipole moment
$\mathbf{q}$	Bloch wavevector
Q_{ext}	Extinction efficiency
$\bar{r}$	Dimensionless distance parameter
$\sigma_x, \sigma_y, \sigma_z$	Pauli spin matrices
$t = \beta d/2$	Intracell spacing
τ	Decay time of plasmon excitations

PUBLICATIONS

This thesis contains work drawn from the following publications:

- Simon R Pocock, Xiaofei Xiao, Paloma A Huidobro and Vincenzo Giannini. Topological Plasmonic Chain with Retardation and Radiative Effects *ACS Photonics* **5**, 2271-2279 (2018)
- Simon R Pocock, Paloma A Huidobro and Vincenzo Giannini. Bulk-edge correspondence and long range hopping in the topological plasmonic chain *Nanophotonics* **8**, 1337-1347 (2019)

The author also contributed to the following publication:

- Marie S Rider, Samuel J Palmer, Simon R Pocock, Xiaofei Xiao, Paloma Arroyo Huidobro, and Vincenzo Giannini. A perspective on topological nanophotonics: Current status and future challenges *Journal of Applied Physics* **125**, 120901 (2019)

1 INTRODUCTION

Topological insulators (TIs) are often described as materials which have an insulating bulk and support edge or surface states, which are protected from defects and disorder by bulk properties of the system. These have applications in spintronics and quantum computing [2], but TIs are perhaps most exciting because they exist outside of the traditional spontaneous symmetry breaking paradigm of condensed matter theory.

Although TIs are traditionally electronic systems, photonic versions can be built out of dielectric or metallic particles. The resultant structures manipulate the flow of light, and their protected edge states have applications in optical response [3], lasing [4, 5], and waveguides [6–9]. Over the course of the thesis we show that the chain of metal nanoparticles with alternating spacing is a photonic TI whose behaviour depends on its parameters and the polarisation of light.

It is intended that this thesis be accessible to a recent physics graduate with some knowledge of the band structure theory of condensed matter physics. This is covered in several undergraduate textbooks, for example Hook and Hall [10].

1.1 OVERVIEW

In this chapter, we aim to provide an introduction to TIs that could be useful for anyone new to the field. The hope is that this might prove useful even beyond the context of this thesis. This means that there is more here than strictly necessary for understanding the original work in later chapters, but this extra information gives a flavour of the field and provides some context for the work. We discuss the field of TIs and the closely related field of photonic topological insulators (PTIs), as well as the part played by non-Hermiticity. A summary of how these concepts are linked is presented in figure 1.1.

In chapter 2, we begin to focus on the specific theory needed for the rest of the thesis. This includes a detailed description of the Su-Schrieffer-Heeger model and a discussion of Mie theory and the Green's function formulation of the vector wave equation.

In chapter 3, we build upon this theory to describe the alternating chain of metallic nanoparticles. We discover that the topology of the chain depends on the polarisation of the modes and examine the edge modes in the longitudinal case. We see that these edge modes are well protected against disorder.

In chapter 4, we use a slightly different model to understand the topological properties of the transverse polarisation of the system. We elaborate on how symmetry breaking can lead to the breakdown of bulk-edge correspondence and develop a measure for where, in parameter space, breakdown occurs.

In chapter 5, we move past the question of bulk-edge correspondence and instead explore the topological phases of the transverse system regardless of edge modes.

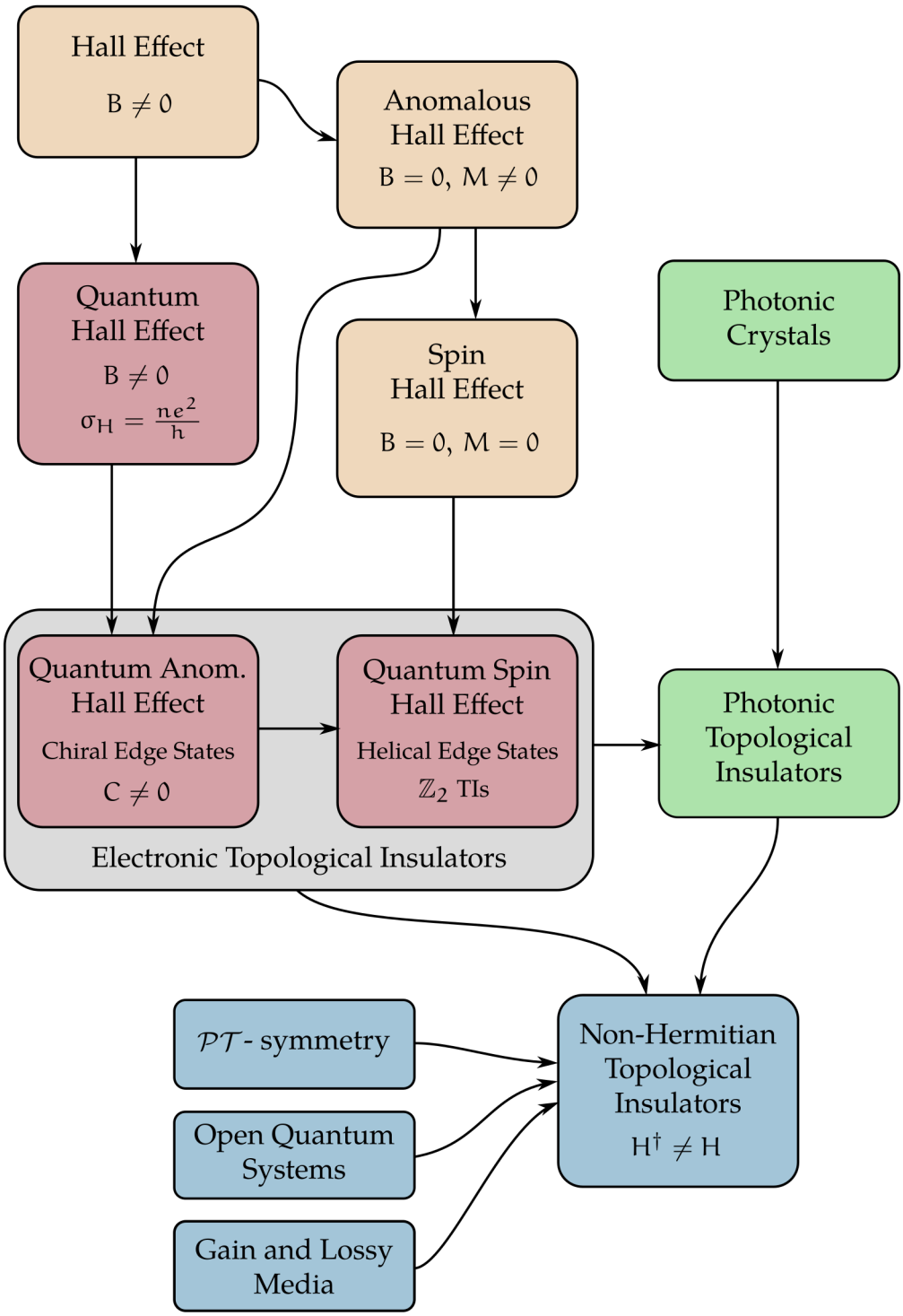

Figure 1.1: Diagram of the links from the Hall effect to the rich physical phenomena surrounding topological insulators, discussed in detail in section 1.2. Chern and $\mathbb{Z}_2$ TIs (red) are quantum versions of the Hall effect and its cousins (orange). PTIs emerge as a natural consequence of photonic crystals (green) and analogies to electronic TIs. Non-Hermitian TIs are an extension of traditional electronic and photonic TIs with added non-Hermitian ingredients (blue), such as $\mathcal{PT}$-symmetry, open quantum systems, and gain and lossy media.

We propose a 'minimal model' to describe the same topological phases and show preliminary work in understanding the band structures of this model.

1.2 A CRASH COURSE ON TOPOLOGICAL INSULATORS

We start with an introduction to electronic TIs. First, we outline the historical emergence of TIs, from the Quantum Hall Effect (QHE) to the burgeoning modern field that exists today [11–13], and then address fundamental concepts in topological physics, such as topological numbers and bulk-edge correspondence. This section culminates in the symmetry ideas that lead to the classification of topological insulators, the so-called 'topological periodic table'.

We then discuss the analogues between electronic crystals and photonic crystals, which give rise to photonic topological insulators [14–16]. These systems often come with in-built non-Hermiticity, motivating further discussion on the thriving topic of non-Hermitian TIs. We conclude this introductory chapter with an outline of the very recent non-Hermitian topological periodic table.

1.2.1 History of TIs

In 1980, a mysterious discovery by von Klitzing, Dorda, and Pepper [17, 18] set off the first domino in a chain that would lead to the establishment of the diverse and exciting field of Topological Insulators (TIs). Von Klitzing *et al.* found that under certain conditions the well known Hall effect behaves unexpectedly. In the Hall effect, current I flows through a two-dimensional plate with a magnetic field $\mathbf{B}$ applied perpendicular to the plate axis, much like the set-up in figure 1.2(a) [19]. The magnetic field diverts electrons to one side of the plate via the Lorentz force, $\mathbf{F} = -e(\mathbf{E} + \mathbf{v} \times \mathbf{B})$, and a potential difference V_H is measured perpendicular to the plate. Classically this potential difference increases proportional to the strength of the magnetic field, $V_H \propto B$.

Von Klitzing *et al.* discovered that for extremely low temperatures ($T < 3\,K$) and strong magnetic fields ($B > 1\,T$), the Hall resistance $R_H = V_H/I$ has striking plateaus, as depicted in figure 1.2(b). At these plateaus the Hall resistance is given to incredible accuracy by $R_H = h/\nu e^2$, where ν is an integer. This has since allowed the measurement of the fundamental constants h/e^2 with relative errors on the order of 10^{-10} [20]. In addition to this, conducting edge states which are immune to backscattering exist around the edge of the plate. These states are called 'chiral' because they move in only one direction around the plate [21]. This was dubbed the Quantum Hall Effect (QHE).

A semi-classical explanation is that the large magnetic field forces electrons into cyclotron orbits with frequencies given by $\omega_c = eB/m_e$, as shown in figure 1.2(a). These have energies $\mathcal{E}_n = \hbar\omega_c(n + 1/2)$, called Landau levels. In the simplest model they are highly degenerate, as many electrons can have the same energy if they are separated by the magnetic length $\sqrt{\hbar/eB}$. In reality, they are smeared out in energy due to temperature, disorder and electron interaction effects. A sketch of these levels is depicted in figure 1.2(c).

If the Fermi level $\mathcal{E}_F$ lies between the Landau levels, the bulk of the system acts as an insulator and R_H is at a plateau. Here the on-diagonal elements of the resistivity

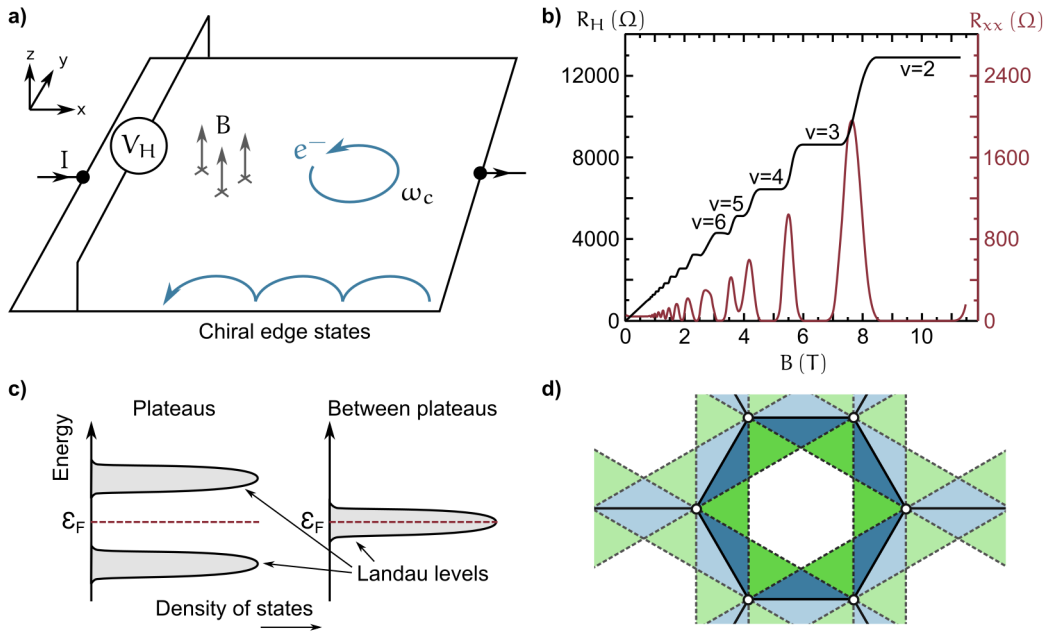

Figure 1.2: a) Diagram of the Quantum Hall Effect (QHE). b) Sketch of the Hall and longitudinal resistances, R_H and R_{xx}, measured in a QHE experiment, based on a figure for GaAs at $T = 0.3\,K$ with permission from Schurr [22]. c) Sketch of the densities of states of electrons in the QHE. d) The Haldane model with circles representing electron sites, black solid lines representing nearest neighbour hopping and grey dashed lines representing next-nearest neighbour hopping. Green and blue regions have equal and opposite amounts of magnetic flux passing through them due to a staggered magnetic field perpendicular to the plane, and the white regions have zero magnetic flux passing through them.

and conductance tensors are zero, meaning that the resistance and conductance in the x direction are both zero. Figure 1.2(b) shows the zeroes for the resistance in the x direction, R_{xx}, occurring at the plateas of the Hall resistance, R_H. If the Fermi level lies on a band, the system acts as a conductor and R_H changes smoothly between plateaus.

In the semi-classical picture, the electrons can't complete a full orbit at the edges and instead skip along the boundary, creating the chiral edge modes depicted in figure 1.2(a). The number of edge modes is equal to the number of Landau levels below the Fermi energy because each level contributes a different skipping orbit along the boundary. This in turn is equal to the corresponding value of ν for the Hall resistance plateau because each new edge state increases the conductivity across the plate by e^2/h. In this way, the QHE has a property of the bulk, given by topological number ν, which corresponds to the existence of edge states. This is bulk-edge correspondence (BEC), a key ingredient in the world of TIs.

This picture is a little naive because it requires the magnetic field to be very finely tuned, or the systems to be translationally symmetric [23]. This contradicts the fact that the most striking thing about the QHE is just how insensitive it is to the magnetic field. In 1982, Thouless, Kohmoto, Nightingale, and den Nijs presented a theory for the QHE which was later shown to be intimately related to the mathematics of topology [24]. Inspired by the famous Hofstadter butterfly [25], they defined a magnetic unit cell on the 2 dimensional electron gas of the plate through which the

magnetic flux is an integer multiple of e/h. This allowed them to apply Bloch's theorem and define a magnetic Brillouin Zone (BZ).

Bloch's theorem states that in a system with, in this case magnetic, unit cells the single electron wavefunction $\Psi(\mathbf{q}, \mathbf{r})$ can be written as a product of the unit cell wavefunction $u_n(\mathbf{q}, \mathbf{r})$ and a phase factor $e^{i\mathbf{q}\cdot\mathbf{r}}$ as follows,

$$\Psi_n(\mathbf{q}, \mathbf{r}) = u_n(\mathbf{q}, \mathbf{r}) e^{i\mathbf{q}\cdot\mathbf{r}}, \tag{1.1}$$

where u_n is periodic in the unit cell and n is a label for the n^{th} band. The Bloch momentum is given by $\mathbf{q}$. Using the Kubo formula for bulk conductivity of 2d systems, and treating the system as if it has no particle interactions, this gave an equation for the Hall conductance at $T = 0\,K$,

$$\sigma_H = \frac{e^2}{h} \sum_n \frac{i}{2\pi} \iint_{BZ} \iint_{UC} \left(\frac{\partial u_n^*}{\partial q_x} \frac{\partial u_n}{\partial q_y} - \frac{\partial u_n^*}{\partial q_y} \frac{\partial u_n}{\partial q_x} \right) d^2\mathbf{r}\, d^2\mathbf{q}, \tag{1.2}$$

where the sum is over filled Landau levels n and UC is the real space unit cell. The summand in the above equation evaluates only to integers, which guarantees the plateaus seen in figure 1.2(b) and ultimately can be used to explain the existence of the edge states. The summand is sometimes called the TKNN invariant, after its discovers, and is equal to the Chern number C_n, a concept already understood in the mathematics of topology [26, 27]. The total Chern number, $C = \sum_n C_n$, predicts the number of edge states in the system and is equal to ν. If two materials with different Chern numbers are interfaced, then the number of edge states at the interface is equal to the difference between their Chern numbers, with free space acting as a trivial insulator with Chern number zero. This relationship between properties of the bulk and the existence of edge states is commonly called bulk-edge correspondence (BEC) [28, 29]. These ideas will be elaborated upon in the next section of the introduction, but for now we continue with the historical perspective.

Alongside these theoretical developments others had already found systems where the Hall conductance had plateaus at fractional values of ν [30]. This Fractional Quantum Hall Effect (FQHE) was shown to be due to electron-electron interactions, where the systems could be framed as non-interacting quasiparticles with fractional charge [31–33]. In this work we will focus mostly on single electron, or non interacting, systems because these systems are more analogous to the photonic systems we consider later, as photons do not self-interact.

As we have seen, the classical Hall Effect requires an applied magnetic field. However, shortly after its discovery the Anomalous Hall Effect was measured, where a material with an intrinsic magnetisation $M \neq 0$ would exhibit a non zero Hall voltage, even in the absence of an external magnetic field [34]. In 1988, Haldane introduced a simple toy model which reproduced the Quantum Hall Effect with no net applied magnetic field, setting the stage for the Quantum Anomalous Hall Effect (QAHE).

Haldane used a tight binding, nearest neighbour hopping model for graphene as the base for his system, years before the material was isolated and subsequently exploded in popularity [35]. This model produces a dispersion relation with linear regions $\mathcal{E} \propto |\mathbf{q}|$, called Dirac cones, at its K and K′ points. Haldane introduced a staggered magnetic field piercing the hexagonal unit cell and considered next-nearest neighbour hopping, as shown in figure 1.2(d). In the diagram, white circles represent sites, black solid lines represent nearest neighbour hopping, and grey dashed lines

represent next nearest neighbour hopping. The blue and green areas are pierced by equal but opposite amounts of magnetic flux due to a magnetic field perpendicular to the 2d sheet. The white areas are pierced by zero magnetic flux. Importantly, this staggered magnetic field is designed in such a way that the average field is zero.

Due to the Aharonov-Bohm effect, where particles moving in a closed path pierced by magnetic flux pick up a phase depending on the flux [36], the next-nearest neighbour hopping is complex valued. Each next-nearest neighbour hop gains a $-\phi$ phase in the clockwise direction and the opposite $+\phi$ phase in the counterclockwise direction. This opens up a band gap and, in a similar manner to the QHE, each of the bands has an associated Chern number. In this way, Haldane presented a model with the same topological properties as the QHE, featuring quantised Hall conductivity and edge states linked to the total Chern number, without Landau levels or a net external magnetic field.

Several researchers expanded on this theoretical work on the QAHE [13, 37–39], calling this type of topological insulator 'Chern insulators' because of their associated topological number. It's worth noting that the QHE is also sometimes called a Chern insulator. The first experimental example of a QAHE Chern insulator was identified by Chang *et al.* in 2013 [40].

In the mean time, a more ubiquitous type of two dimensional TI had already come into prominence, namely the Quantum Spin Hall Effect (QSHE). In the classical Spin Hall Effect there is no applied magnetic field or magnetisation. Instead, up and down electrons are displaced towards opposite edges of the plate by spin-orbit coupling effects. This leads to no net Hall voltage, but one can consider a non-zero spin Hall voltage where the spins of the electrons are taken into account. Similarly, in the quantum case there is no net edge current, but up and down electrons flow in opposite directions around the edge. This pair of opposite direction chiral edge states is called a helical edge state. The first theoretical examples of the QSHE built upon Haldane's work by considering graphene with the staggered magnetic field replaced by spin-orbit coupling [41, 42]. There have been several experimental realisations of such systems, the first of which was by Bernevig and Hughes in 2006 [43]. Such systems are time-reversal symmetric and feature a net zero Chern number, meaning that they are described by a different topological invariant. For reasons which will become clear later, there is either one pair of protected counter-propagating edge states or no protected edge states at all, so that their topological number can be thought of as either 1 or 0. For this reason these systems are often referred to as $\mathbb{Z}_2$ topological insulators, where $\mathbb{Z}_2$ is the set containing 0 and 1.

From these building blocks, the field of TIs blossomed. One- and three-dimensional materials exhibiting topological properties were discovered alongside geometric structures leading to topological effects. The scope of TIs expanded to include classical photonic and acoustic systems whose behaviour in regular structures is analogous to electrons in crystals, and to include systems described by Hamiltonians which do not fit under the usual quantum mechanical requirement of Hermiticity.

The discovery of topological insulators represents a paradigm shift, moving beyond the spontaneous symmetry breaking ideas that dominated condensed matter physics in the past. Partly in recognition of this, Thouless, Haldane, and Kosterlitz won the Nobel prize for physics in 2016 for their contributions to topological physics, including the 1982 description of the QHE and the Haldane model [44]. Von Klitzing won his for the discovery of the QHE in 1985 [45]. In the next few sections we go

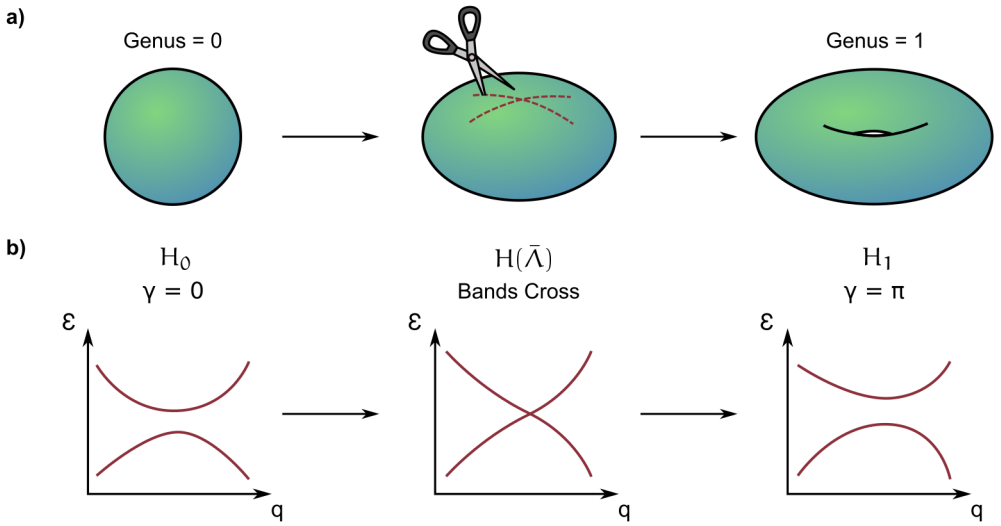

Figure 1.3: a) Diagram of the equivalence classes of mathematical topology. b) Diagram of equivalence classes of gapped Hamiltonians

on to discuss important concepts in TIs and examine photonic topological insulators (PTIs) and non-Hermiticity in greater detail.

1.2.2 Bands and Topological Numbers

In this subsection we introduce some of the basic ideas of topological insulators: the topological invariant and bulk edge correspondence. First, we start with their link to the mathematical concept of topology.

In mathematics, topology is the study of the properties of spatial objects which are preserved by distortion, but not by cutting or stitching. For example, a sphere can be distorted into a cube, so the two are topologically equivalent. As in figure 1.3(a), a sphere must be cut or stitched in order to morph into a torus, so the two are topologically distinct. We can label the different topological classes by their genus g, equal to the number of 'holes' in the shape. Shapes with the same genus are topologically equivalent. According to the Gauss-Bonnet theorem the Gaussian curvature, K, of the closed 2d surface, S, of a shape is closely related to its genus,

$$\frac{1}{2\pi}\iint_S K \, dA = 2 - 2g. \tag{1.3}$$

How might we apply some of the ideas of topology to physics? We are interested in insulators; materials which, at 0 Kelvin, have a band gap separating a filled band of valence electrons with an empty band of conduction electrons. So, instead of spatial objects, let's consider two gapped Hamiltonians H_0 and H_1 and ask how we might deform one to another. Figure 1.3(b) shows illustrative band structures and a possible method of transformation between the two. First we define a linear interpolation, $H(\Lambda) = (1-\Lambda)H_0 + \Lambda H_1$, and see what happens as we change Λ adiabatically. If, for some value $\Lambda = \bar{\Lambda}$, the gap in the band structure of Hamiltonian $H(\Lambda)$ closes, we have left the space of gapped Hamiltonians. This is equivalent to cutting or stitching when

transforming spatial objects. If there is no way to move between two Hamiltonians without the bands crossing, then those two Hamiltonians are topologically distinct, much like a sphere and a torus. A topological number can be defined which classifies the Hamiltonians into two different categories: much like the genus, Hamiltonians with different topological numbers are topological distinct.

For example, the Zak phase is a commonly used topological number in 1d systems like the ones we study in chapters 3, 4 and 5. In higher dimensions the same phase is referred to as the Berry phase, which is related to the Chern number, commonly used in 2d systems. Here we introduce the Berry phase and, for completeness, discuss the Chern number.

Consider a quantum state $|\Psi(\mathbf{R})\rangle$, where $\mathbf{R}$ is an element of some d-dimensional parameter space. Berry showed that, if $\mathbf{R}$ moves adiabatically in a closed loop through parameter space the state picks up a phase γ, which is gauge independent. This phase can be non zero and is known as the geometric phase or the Berry phase. This can be calculated by considering the phase picked up over a tiny step $\delta\mathbf{R}$ and then integrating over a closed directed curve in parameter space, labelled Q. Doing so gives

$$\gamma = \oint_{Q} \mathbf{A}(\mathbf{R}) \cdot d\mathbf{R}, \tag{1.4}$$

where

$$\mathbf{A}(\mathbf{R}) = i\langle\Psi(\mathbf{R})|\nabla_{\mathbf{R}}|\Psi(\mathbf{R})\rangle \tag{1.5}$$

is called the Berry connection.

We can apply this geometric phase to a Hamiltonian whose parameters are in Bloch space, $\mathcal{H}(\mathbf{q})$, by considering its eigenvalue equation

$$\mathcal{H}(\mathbf{q})|u(\mathbf{q})\rangle = \mathcal{E}(\mathbf{q})|u(\mathbf{q})\rangle, \tag{1.6}$$

where $\mathcal{E}(\mathbf{q})$ are the eigenvalues and $|u(\mathbf{q})\rangle$ the eigenfunctions. Now the Berry phase integral is over a closed curve in the BZ,

$$\gamma = \oint_{Q} \mathbf{A}(\mathbf{q}) \cdot d\mathbf{q} = \oint_{Q} i\langle u(\mathbf{q})|\nabla_{\mathbf{q}}|u(\mathbf{q})\rangle \cdot d\mathbf{q}. \tag{1.7}$$

In some systems the Berry phase is quantised, so that it cannot change under adiabatic deformations of the Hamiltonian unless the bands cross. For example, in figure 1.3(b) the Hamiltonian H_0 has Berry phase $\gamma = 0$, and H_1 has Berry phase $\gamma = \pi$. This indicates that the two Hamiltonians have different topological properties, again in much the same way that the genus indicates that two shapes are in different topological classes. Each Hamiltonian is said to have different 'topological phases', with a 'topological phase transition' occurring where the bands cross. We will see an example of how the Berry phase is applied in a 1d system in section 2.1.

Another useful concept is the Berry curvature, given by the curl of the Berry connection,

$$\mathbf{B}(\mathbf{q}) = \nabla_{\mathbf{q}} \times \mathbf{A}(\mathbf{q}). \tag{1.8}$$

In the context of Hamiltonians, if the eigenfunctions $|u(\mathbf{q})\rangle$ are smooth enough the Berry phase can be written as an integral over the entire BZ instead of a closed curve,

$$\gamma = \oint_{Q} \mathbf{A}(\mathbf{q}) \cdot d\mathbf{q} = \int_{BZ} \mathbf{B}(\mathbf{q})\, d\mathbf{q}. \tag{1.9}$$

This results from Stokes' theorem. If $|u_n(\mathbf{q})\rangle$ are not smooth, the Berry phase is equal to the right hand side of equation 1.9 up to an integer multiple of 2π.

The Berry connection allows us to introduce the formula for the Chern number, given by

$$C = \frac{1}{2\pi} \int_{BZ} \mathbf{B}(\mathbf{q})\, d\mathbf{q}. \tag{1.10}$$

For a 2d system, this leads to

$$C = \frac{i}{2\pi} \iint_{BZ} \left(\frac{\partial A_y}{\partial q_x} - \frac{\partial A_x}{\partial q_y} \right) d^2\mathbf{q}. \tag{1.11}$$

As alluded to earlier, this is the same as the summand in the equation for the Hall conductance, equation 1.2. Each band has an associated Chern number given by equation 1.11, and the sum runs over each band, leading to a total Chern number.

In a 2d system like the QHE system, the BZ is a torus due to the periodicity of q_x and q_y. This means that, if it is possible to define $\mathbf{A}(\mathbf{q})$ continuously over the BZ, then the Chern number is zero. A non-zero Chern number indicates the existence of singularities in the Berry connection, sometimes called vortices because the arrows of the $\mathbf{A}(\mathbf{q})$ vector field swirl around the singularities. Each vortex contributes an integer to the Chern number, given by the number of times it swirls around the singularity, with the direction dictating whether the contribution is positive or negative. Plus-minus pairs of vortices can mutually annihilate, which makes no difference to the Chern number. Individual vortices don't disappear easily under small distortions of the Hamiltonian, so that the Chern number does not change unless the Hamiltonian leaves the space of gapped Hamiltonians.

This very brief explanation has left out some of the subtleties involved in these calculations. We recommend chapter 2 of *A Short Course on Topological Insulators* for the interested reader [46].

From this process we have seen that the Chern number is calculated purely from properties of the bulk Bloch Hamiltonian. One of the most intriguing aspects of Hermitian TIs is that this number is so closely linked to the number of edge states of the system through bulk-edge correspondence (BEC), with no need for specific information about the edge. We have seen this is true for the QHE, but it is in fact a general property of Hermitian topological insulators.

A commonly used illustration of why edge states exist at the boundary between two materials with different topological numbers is to consider an interface between two such materials, as in figure 1.4(a). Either side of the interface the bands are gapped, with the bulks acting as insulators. As we move across the interface in real space there is a transition between topological numbers, which can only happen if the bands close at some point, sketched in figure 1.4(b). Edge states have energies in

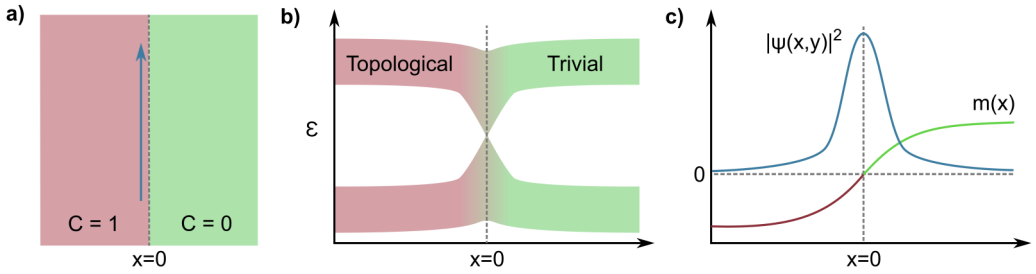

Figure 1.4: a) Sketch of two half planes with different topological numbers interfaced at $x = 0$. b) Sketch of band structures closing at the interface between two systems of different topological numbers. c) Sketch of $m(x)$ and $|\psi(x,y)|^2$ for the Dirac Hamiltonian model for (a).

the gap of the bulk band structure, and therefore exist in the region where the bands close at the interface.

A more advanced picture based on work by Jackiw and Rebbi [47] is to consider a Dirac Hamiltonian with some additional mass term. Here a Dirac Hamiltonian means a Hamiltonian linear in $\mathbf{q}$, like graphene near its K and K′ points. The added non-zero mass term creates a gap in the band structure, and in various 1d and 2d examples [11, 46, 48] negative and positive masses are equivalent to different topological phases. This is represented in Haldane's model; near the Dirac cone a positive mass is trivial, $C = 0$, and a negative mass has Chern number $C = 1$. Let's consider the linearised real space Hamiltonian for Haldane's model,

$$\mathcal{H} = \hbar v_F(-i\boldsymbol{\sigma}\cdot\nabla) + m\sigma_z, \tag{1.12}$$

where v_F is the Fermi velocity of electrons in graphene, $\boldsymbol{\sigma}$ is the vector of Pauli matrices $(\sigma_x, \sigma_y, \sigma_z)$, and m is the mass term. We examine a system where two half-planes of this material meet at an interface $x = 0$, and m is only dependent on x. We can choose these two half planes to have different Chern number by choosing $m(x) > 0$ for $x > 0$ and $m(x) < 0$ for $x < 0$. This has an exact solution,

$$\psi(x,y) \propto e^{iq_y y} \exp\left(-\int_0^x m(x')dx'\right)\begin{pmatrix}1\\1\end{pmatrix}, \tag{1.13}$$

a state which is confined in the x direction but moves in the positive y direction. In other words, this is a chiral edge state. Figure 1.4(c) provides a sketch of $m(x)$ and the confined $|\psi(x,y)|^2$.

TIs have been shown to exist in multiple dimensions, beyond the original 2d systems inspired by the Hall effect. In a TI with dimension d the edge states are typically of dimension $d-1$, in both the physical system and the inverse Fourier space of the BZ. This is because the edge is one fewer dimension than the bulk. What do edge states look like in a band structure?

Say we wish to study the edge modes of a 1d TI. We might do this by solving a finite chain for all of its modes, providing a range of energies but with no associated bulk Bloch q value. This makes it hard to picture bulk and edge modes at the same time. Later in the thesis we use a fun solution to this problem where modes are assigned q values based on their mode profiles. In the mean time, we superpose

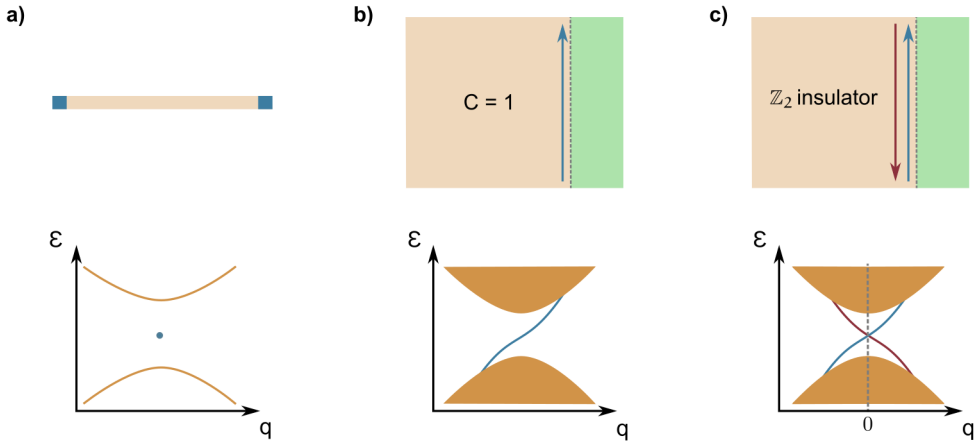

Figure 1.5: a) Upper: sketch of a finite 1d chain with blue edge modes. Lower: sketch of an 1d orange bulk band structure overlaid with blue edge modes in the gap. b) Upper: sketch of a strip of $C = 1$ material with an edge mode indicated by a blue arrow. Lower: sketch of the corresponding band structure with the bulk modes in orange and the edge mode in blue. c) Upper: sketch of a strip of $\mathbb{Z}_2$ insulator with edge modes in blue and red. Lower: sketch of the corresponding band structure with the edge modes in blue and red.

edge modes (blue) onto bulk modes (orange) in figure 1.5(a), and see that edge modes simply sit in the gap between the valence and conduction bands.

In 2d systems we can perform the same trick of superposition of solutions of bulk and finite systems, or avoid this by considering a strip of the 2d material, made finite in the x direction and infinite in the y direction. When we apply Bloch's theorem in the y direction we get something which looks like the sketches in figure 1.5(b) and (c), although for the sake of clarity we have removed the edge mode(s) which correspond to the left hand side of the strips. Figure 1.5(b) shows the right hand side of a strip with Chern number $C = 1$, with a single edge mode (blue) connecting the lower and upper bands (orange). The group velocity of any mode is given by $d\mathcal{E}/dq$, indicating that this edge mode travels only in the $+y$ direction and is protected from backscattering. Although not shown here, the left side mode would connect the two bands in a similar way, but with a negative slope and group velocity.

Figure 1.5(c) shows a strip of $\mathbb{Z}_2$ TI, with a pair of edge modes confined to the right hand side of the strip. Each mode has opposite spin and travels in opposite directions corresponding to two modes in the gap with opposite slopes in the band structure sketch. The key property of electronic $\mathbb{Z}_2$ topological insulators is that they have a special type of time reversal symmetry, whose operator $\mathcal{T}$ obeys $\mathcal{T}^2 = -1$. This emerges from the spin-orbit coupling and the Fermi-Dirac statistics of spin-1/2 electrons. Due to the nature of the time reversal symmetry, Kramers' theorem applies, which says that every eigenstate has an orthogonal time reversed partner eigenstate with the same energy. This means that every edge state has an orthogonal partner edge state which travels in the opposite direction and has the same energy, causing the band structure to be symmetric in q. Therefore every state which sits on the centre or edge of the BZ must be doubly degenerate at that point.

Edge states at a generic q value can be deformed out of the gap adiabatically by coupling with an edge state travelling in the reverse direction. Doing so causes the number of edge states to decrease by 4, because an orthogonal pair at $-q$ must

also deform out of the gap. However, edge states which cross the center or edge of the BZ cannot annihilate as they would break the double degeneracy requirement of Kramers' rule. This is the protected pair of edge states, allowing for either 0 or 1 pair of protected edge states in a $\mathbb{Z}_2$ TI. In addition, it can be shown that the $\mathcal{T}^2 = -1$ property means that these edge states are protected from backscattering by any impurity or deformation that doesn't break time reversal symmetry.

In three dimensions, TIs feature multiple topological invariants and can generally be characterised as weak or strong. Weak TIs act like stacked 2d systems and strong TIs feature protected conducting surface states. Originally the study of these 3d TIs emerged by extending the 2d QSHE [49–51]. It's beyond the focus of this thesis to describe all of these properties, but detailed information can be found in several review papers [11, 12, 52].

1.2.3 The periodic table of Hermitian topological insulators

A necessary ingredient for a Chern insulator is the breaking of time reversal symmetry by an external magnetic field or some innate property of the material. In a $\mathbb{Z}_2$ insulator, the requirement is that the time reversal symmetry operator $\mathcal{T}$ squares to -1. This is fulfilled by spin-orbit coupling due to the Fermi-Dirac statistics of spin-1/2 electrons. The topological properties of these two systems are tied in some way to their symmetry properties.

In fact, these are just examples of a wider, fundamental result: a few discrete symmetries can be used to classify *all* TIs in *any* number of dimensions [53, 54]. Topological phases are defined by the conservation of certain discrete symmetries, as opposed to traditional condensed matter phase transitions occurring due to spontaneous symmetry breaking. The categorisation of topological classes is often referred to as the periodic table of topological insulators. This is a powerful tool which allows the topological class of any Hermitian Hamiltonian to be identified relatively easily.

Schnyder, Ryu, Furusaki and Ludwig showed that one way to classify topological insulator Hamiltonians was to study random gapped matrices [55]. TI Hamiltonians can be represented as gapped matrices, and although these are not often random because they are constructed from models of regular lattices, they can become random under small deformations which do not close the gap. Therefore, there are random gapped matrices which have the same topology as typical TI matrices. In their study of random matrices, Altland and Zirnbauer (AZ) showed that there were a total of ten different symmetry classes under which such a Hamiltonian could fall, known as the ten-fold way [56].

Each of these ten symmetries is constructed out of time reversal symmetry, $\mathcal{T}$, and particle-hole symmetry, $\mathcal{C}$. Both of these symmetries are anti-unitary, meaning that they are equal to the product of a unitary matrix, $\mathcal{U}_T$ and $\mathcal{U}_C$ respectively, and the complex conjugation operator $\mathcal{K}$. Their effects on a first quantised Hamiltonian is as follows:

$$\mathcal{T}: \qquad \mathcal{H} = \mathcal{U}_T^\dagger \mathcal{H}^* \mathcal{U}_T, \tag{1.14}$$

$$\mathcal{C}: \qquad \mathcal{H} = -\mathcal{U}_C^\dagger \mathcal{H}^T \mathcal{U}_C. \tag{1.15}$$

Symmetry				Dimension							
Cartan	$\mathcal{T}$	$\mathcal{C}$	$\mathcal{S}$	1	2	3	4	5	6	7	8
A	0	0	0	0	$\mathbb{Z}$	0	$\mathbb{Z}$	0	$\mathbb{Z}$	0	$\mathbb{Z}$
AIII	0	0	1	$\mathbb{Z}$	0	$\mathbb{Z}$	0	$\mathbb{Z}$	0	$\mathbb{Z}$	0
AI	1	0	0	0	0	0	$2\mathbb{Z}$	0	$\mathbb{Z}_2$	$\mathbb{Z}_2$	$\mathbb{Z}$
BDI	1	1	1	$\mathbb{Z}$	0	0	0	$2\mathbb{Z}$	0	$\mathbb{Z}_2$	$\mathbb{Z}_2$
D	0	1	0	$\mathbb{Z}_2$	$\mathbb{Z}$	0	0	0	$2\mathbb{Z}$	0	$\mathbb{Z}_2$
DIII	−1	1	1	$\mathbb{Z}_2$	$\mathbb{Z}_2$	$\mathbb{Z}$	0	0	0	$2\mathbb{Z}$	0
AII	−1	0	0	0	$\mathbb{Z}_2$	$\mathbb{Z}_2$	$\mathbb{Z}$	0	0	0	$2\mathbb{Z}$
CII	−1	−1	1	$2\mathbb{Z}$	0	$\mathbb{Z}_2$	$\mathbb{Z}_2$	$\mathbb{Z}$	0	0	0
C	0	−1	0	0	$2\mathbb{Z}$	0	$\mathbb{Z}_2$	$\mathbb{Z}_2$	$\mathbb{Z}$	0	0
CI	1	−1	1	0	0	$2\mathbb{Z}$	0	$\mathbb{Z}_2$	$\mathbb{Z}_2$	$\mathbb{Z}$	0

Table 1.1: The periodic table of topological insulators [54]. The first column represents Cartan's labels for matrices which obey the next three column's symmetry constraints. $\mathcal{T}$ represents time reversal symmetry, $\mathcal{C}$ represents particle-hold symmetry and $\mathcal{S}$ represents sublattice, or chiral, symmetry. For a certain dimension of the system and a certain symmetry class the material has a certain number of topological phases available to it. 0 means there is only the trivial phase, $\mathbb{Z}$ means there are infinitely many integer topological phases, corresponding to a Chern insulator, $2\mathbb{Z}$ represents infinitely many even integer topological phases, another type of Chern insulator, and $\mathbb{Z}_2$ allows for two topological phases, corresponding to a spin hall type effect.

In the second of these equations we use the transpose, which, for a Hermitian Hamiltonian, is identical to the conjugate, $\mathcal{H}^T = \mathcal{H}^*$. The reason for this will become clear when discussing symmetry properties of non-Hermitian Hamiltonians. In addition to time reversal and particle-hole symmetry, the product of the two operators $\mathcal{S} = \mathcal{T} \cdot \mathcal{C}$ is known as the chiral or sublattice symmetry (SLS) operator. Its effect on the Hamiltonian is given by

$$\mathcal{S}: \qquad \mathcal{H} = -\mathcal{U}_S^\dagger \mathcal{H} \mathcal{U}_S. \tag{1.16}$$

Both the time reversal symmetry and particle-hole symmetry operators square to either plus or minus one, so that any one matrix can have $\mathcal{T} = 0$, no time reversal symmetry, or $\mathcal{T}^2 = \pm 1$. Each matrix can also have $\mathcal{C} = 0$, no particle-hole symmetry, or $\mathcal{C}^2 = \pm 1$. The combination of these allows for 9 different symmetry classes. The sublattice symmetry operator is fixed in all but 1 of these combinations. If a random matrix has no time reversal or particle-hole symmetry, it is possible for sublattice symmetry to be absent or present, represented by $\mathcal{S} = 0, 1$. This adds up to the ten different symmetry classes of the ten-fold way, which are summarised in table 1.1. In the $\mathcal{T}$ column, ± 1 represents time reversal symmetry where the operator squares to ± 1 respectively. The same is true for the $\mathcal{C}$ column for particle-hole symmetry.

Each of these symmetry classes puts constraints on the time evolution operator of the $N \times N$ Hamiltonian, $\exp(it\mathcal{H})$, forcing it to be an element of a certain matrix group. The simplest example of this is when $\mathcal{T} = 0$, $\mathcal{C} = 0$ and $\mathcal{S} = 0$. Then there are no restrictions on $\exp(it\mathcal{H})$ except that it is unitary by nature, so it is an element of

the unitary group $U(N)$. Cartan classified these matrix groups in 1926, and Cartan's labels corresponding to the symmetry properties are given by the first column of table 1.1.

For each symmetry class there are a certain number of Hamiltonians which cannot be deformed into each other without closing the gap. Each of these Hamiltonians must therefore be in a different topological phase, so that the number of inequivalent Hamiltonians in each symmetry class therefore indicates the corresponding type of topological insulator for this class. In table 1.1 these are labelled either 0 for always trivial, $\mathbb{Z}$ for Chern insulators, $2\mathbb{Z}$ for Chern insulators which can only have an even topological number, and $\mathbb{Z}_2$ for QSHE TIs.

Multiple methods can be used to populate the periodic table for topological insulators [53–55, 57]. Some include the use of the fact that edge modes do not experience Anderson localisation to reduce the study of TIs in d dimensions to a study of Anderson localisation in $d-1$ dimensions. Other ideas applied to create this table are those of homotopy groups, K-theory and dimensional reduction.

Kitaev showed that the TI classes are periodic in $d = 8$ dimensions using K-theory. The rows in table 1.1 are arranged in such as way to show the periodicity of the system vertically. We see that there is some periodicity in A and AIII above the horizontal line, as well as a periodicity in the cycle AI $\rightarrow$ BDI $\rightarrow$ D $\rightarrow \ldots \rightarrow$ CI $\rightarrow$ AI. This is known as Bott periodicity and also emerges from K-theory. The two groups which have no time reversal or particle-hole symmetry and $\mathcal{S} = 0, 1$, A and AIII, are sometimes called 'complex' because no constraints are placed on the reality of the Hamiltonian by $\mathcal{T}$ or $\mathcal{C}$. All other classes are 'real' in that there is some reality condition applied. We can see that this table ties nicely in with our already understood TIs, for example the 2-dimensional examples of the QHE and QSHE belong to groups A and AII respectively.

Ultimately, this table provides a powerful tool to identify the strong topological properties of any single particle Hermitian Hamiltonian using its dimensions and symmetry properties. On a conceptual level it also highlights that topological properties are related very closely to symmetry properties of a system. Although not discussed here, all of this information directly corresponds to topological superconductors as well.

Limitations of this periodic table are in so-called weak topological insulators, and the possibility of topological properties which do not directly correspond to edge states. Additionally, the table ignores non-Hermitian systems, the final topic of this introductory chapter. In fact, the Hamiltonian of the system we study in later chapters is non-Hermitian, largely because it is a type of TI called a photonic topological insulator (PTI). We therefore first introduce PTIs, which will provide a nice stepping stone to further discussion of non-Hermiticity.

1.3 PHOTONIC TOPOLOGICAL INSULATORS

Although TIs historically emerged from quantum effects, we have seen that topology in physics is tied instead to a Hamiltonian and its symmetries, allowing classical effects such as photonics and acoustics to exhibit topological properties [58]. Here our focus is on photonics. The approaches one can take to involve topology with photonic systems are too many to include in this short section, so we instead present a

basic overview and recommend several excellent reviews for the interested reader [16, 59–61].

To motivate their study, we note that photonic topological insulators differ from their electronic counterparts in a few key ways. There is no photon-photon interaction, making single particle treatments a natural fit, although non-linearity can be used to couple photons and mimic many body behaviour. There is no Fermi level and no natural ground state, so the systems have to be pumped with photons in order to see their effects. Typically PTIs exist at larger scales and are manufactured directly, making studies of disorder and defects, as well as the topology of finite systems, more accessible. In addition, there are exciting potential applications for protected electromagnetic edge states such as lasing and sensing [4, 62].

In 1987, the concept of a photonic crystal (PC) was introduced independently by Yablonovitch [63] and John [64]. Yablonovich was interested in reducing losses in a semiconductor, caused by the emission of light at a certain frequency, by embedding it in a medium where the light could not propagate. The central idea is that a material in which the dielectric function $\epsilon(\mathbf{r})$ varies periodically in space, for example an array of glass pillars in air, acts in a similar manner to a crystal lattice in an electronic system. The dispersion relation of the light in reciprocal space can be found, giving a band structure, which could be gapped. Light of the frequency in the gap cannot propagate, making it the perfect medium in which to embed the semiconductor in question. The first PC in which an optical frequency band gap existed in all directions was fabricated in 1991 by Lin *et al.* using an arrangement of silicone rods [65] after theoretical and experimental progress in the intervening years [66, 67].

Evidently, gapped photonic band structures can exist in a photonic crystal. In 2008 Haldane and Raghu identified PCs as a possible avenue for topological properties and proposed a crystal made up of a gyromagnetic materials, where the permittivity tensor is affected by an applied external magnetic field [68, 69]. By construction this breaks time reversal symmetry and creates a band gap, setting up the conditions necessary for a Chern insulator. Haldane and Raghu's original concept featured Dirac cones which were gapped by a magnetic field, but it was shown that more general broken time reversal symmetry gapped systems also work [70, 71]. A realistic system was suggested and the first photonic Chern insulator experimentally demonstrated in 2009 by Wang *et al.* [72]. Figure 1.6(a) shows simulations of a protected edge state in this type of system. Like the electronic system, the photonic edge states are unidirectional and protected from scattering by defects.

Many gyromagnetic experiments have been performed since, but they are all in the microwave frequency band of the electromagnetic spectrum. Ideally, we would like to be able to manipulate visible light in this way as well. Although efforts are being made to change the status quo, currently magneto-optic effects are significantly weaker in the visible part of the spectrum.

It is important to note that photonic Chern insulators do not always require an external magnetic field. Introducing a third dimension in which the light propagates, allowing this dimension to be treated as if it was a time dimension, is also a favourable method [73, 77]. Theory for this type of so called Floquet TI takes advantage of the paraxial equation, which describes the propagation of light in a manner analogous to Schrödinger's equation, with the third dimension substituted for time. Figure 1.6(b) shows an experimental design of a Floquet TI. Other ideas such as those of optomechanics or cavities can also be used to probe photonic Chern insulators.

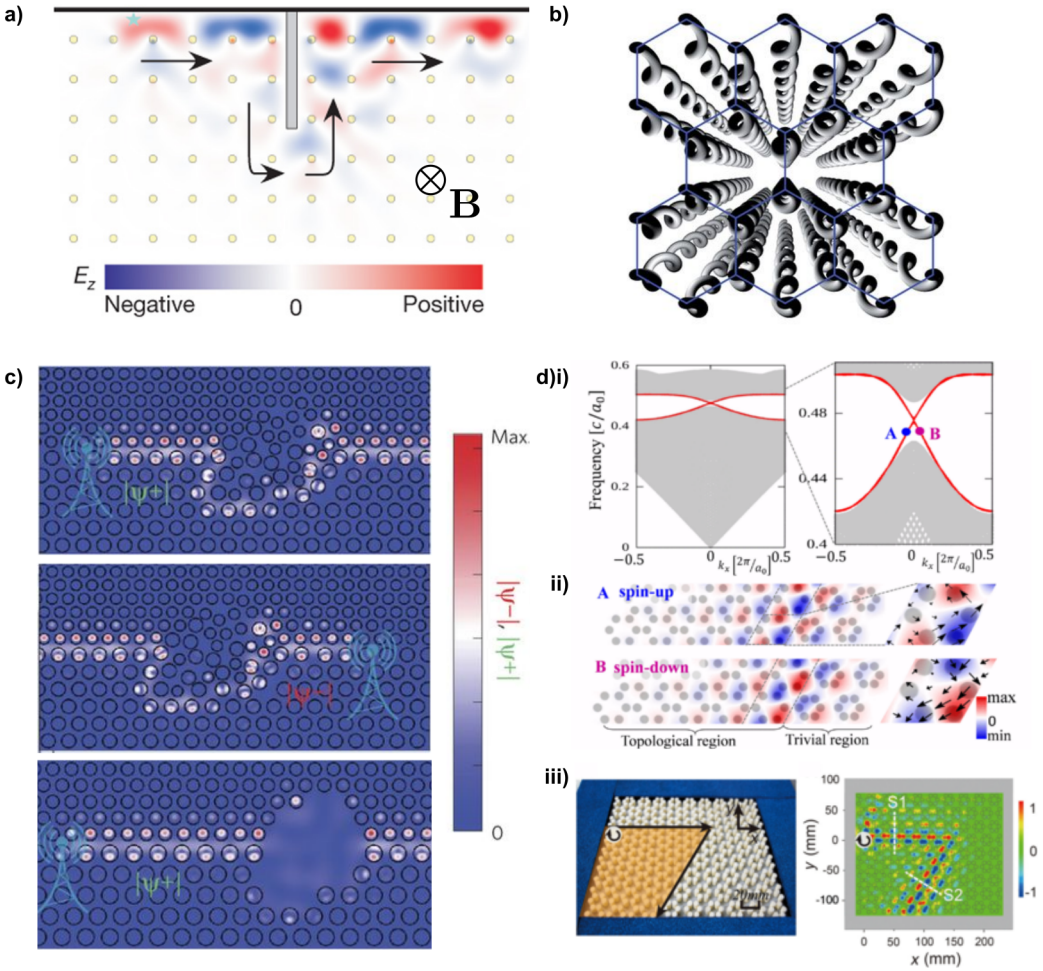

Figure 1.6: a) Electric field distribution in a PTI using an applied magnetic field **B** and a square lattice of gyromagnetic pillars. Edge states travel around defects. Reprinted by permission from Springer Nature: Springer Nature, Observation of unidirectional backscattering-immune topological electromagnetic states, Wang *et al.*, copyright 2009 [72]. b) Floquet TI, in which helical waveguides are arranged in a hexagonal lattice. The helix shape opens up a band gap and breaks time reversal symmetry. Reprinted by permission from Springer Nature: Springer Nature, Photonic Floquet topological insulators, M. C. Rechtsman *et al.*, copyright 2013 [73]. c) Pseudo-spin up, $|\Psi^+|$ and down $|\Psi^-|$ travelling at the interface between a bianisotropic PTI and a trivial material. The edge states are protected from defects and disorder. Reprinted by permission from Springer Nature: Springer Nature Materials, Photonic topological insulators, A. B. Khanikaev *et al.*, copyright 2012 [74]. d) Geometric TI constructed from hexamer unit cells. i) Band structure. ii) Simulation of the up and down spins between topological and trivial regions. i and ii reprinted figures with permission from L.-H. Wu *et al.*, PRL, 114, 223901 (2015). Copyright 2019 by the American Physical Society [75]. iii) Experimental set up and results, with a sharp turn showing edge states. Reprinted figures with permission from Yang *et al.*, PRL, 120, 217401 (2018). Copyright 2019 by the American Physical Society [76].

We begin to run into problems when extending PTIs to include $\mathbb{Z}_2$ insulators, because photons are bosons and therefore obey $\mathcal{T}^2 = +1$ time reversal symmetry instead of the necessary $\mathcal{T}^2 = -1$ symmetry. The solution is to construct some kind of spin-like behaviour using the building blocks of the lattices themselves, or properties

of the crystalline structure. For example, in a system of coupled resonator optical waveguides each resonator contains modes which propagate clockwise or counterclockwise. The clockwise and counterclockwise modes replicate the physics of the two different spins. The problem can also be circumvented using bianisotropic materials, which have equal electric permittivity ϵ and magnetic permeability μ [74, 78]. In PCs made up of these materials, linear combinations of the out-of-plane component of the electric and magnetic fields can be treated as up and down spins, which have the necessary $\mathcal{T}^2 = -1$ time reversal symmetry. These form Kramers pairs, which have robust transportation, as demonstrated by results depicted in figure 1.6(c).

It is also possible to construct $\mathbb{Z}_2$ PTIs using purely geometric considerations. In 2015 Wu and Hu showed that in a triangular lattice of hexagonal unit cells containing six dielectric pillars, as in figure 1.6(d), one could treat the unit cell as a type of atom with a pseudo-spin that replicates the $\mathcal{T}^2 = -1$ requirement and leads to Kramers pairs [75]. In these unit cells, the spacing from the centre of the cell to the pillars R could be varied. For R greater than a third of the lattice constant the material is topological, and for R less than a third of the lattice constant it is trivial. This was experimentally verified shortly afterwards in 2016 [76], shown in figure 1.6(d)iii. Multiple similar designs have been demonstrated since [79, 80]. Notably the existence of edge states in this type of PTI depends on the shape of the edge, and the PTI must be embedded in a topologically trivial medium which obeys the same six-fold rotational symmetry in order to preserve the edge states. This has led to some contention about whether such materials are true TIs.

PTIs in 1d are more easily accessible than their 2d cousins. Unit cells containing 2 identical particles or other similar constructions produce sublattice symmetry and time reversal symmetry with $\mathcal{T}^2 = +1$, falling under the BDI classification in the TI periodic table. Dielectric pillars or slabs can therefore produce the desired effect [81–83]

Photonic media can often feature some form of loss or gain, which causes the field to decrease or grow in amplitude. One common avenue for losses is electron scattering in metals, called Ohmic losses. This is tied closely to the phenomenon of plasmons, which are propagating bulk excitations of electrons in a metal. In quantum many body theory they are described by quasiparticles which are poles of the density-density Green's function, but when we come to discuss them we will circumvent much of the heavy theory using some simplifications.

A surface plasmon polariton (SPPs) is a propagating electric field confined evanescently to a metal-dielectric interface, such as a gold-air interface [84]. A sketch is depicted in figure 1.7(a). This is caused by the coupling of the electric field with the conduction electrons in the metal, and has the effect of squeezing electromagnetic fields to subwavelength scales, beating the classical diffraction limit. SPPs have their electric field perpendicular to the plane of the surface, called s or TM polarisation. Bliokh *et al.* have proposed that SPPs are actually a manifestation of a quantum spin hall effect of light, with the metal acting as a 3d topological insulator [85] and the SPPs as surface modes. In this case the right and left handed circular polarisations of light in free space are treated as opposite pseudospins.

Surface plasmons can also be localised on the surfaces of small metallic particles, in which a surface plasmon resonance between the electric field and electrons is set up [89]. A depiction of this oscillating field is shown in figure 1.7(b). Plasmonic nanoparticles feature very strong near fields and large scattering cross sections, which

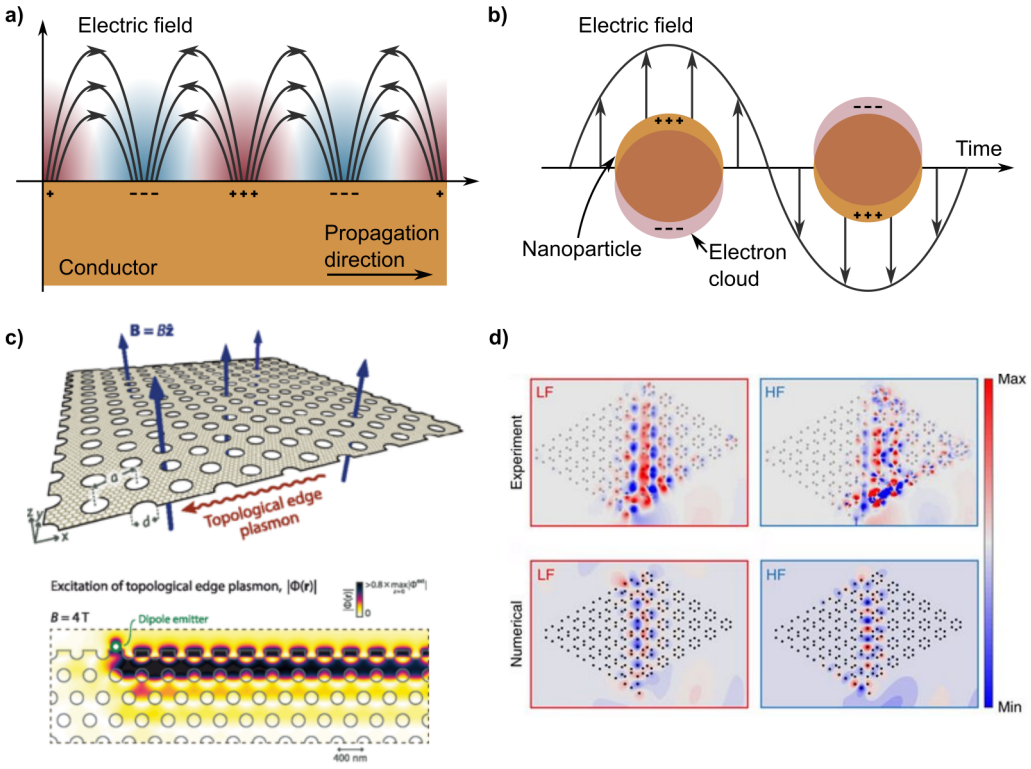

Figure 1.7: a) Surface plasmon polariton (SPP) propagating at the interface between a dielectric and a conductor. b) Localised surface plasmon oscillating in time with an applied electric field. c) Upper: diagram of a plasmonic Chern insulator, featuring a magnetic field passing through holes punched in a hexagonal lattice in graphene. Lower: experimentally demonstrated edge modes. Reprinted figures with permission from D. Jin *et al.*, PRL, 118, 245301 (2017). Copyright 2019 by the American Physical Society [86]. d) Experimental and simulated edge modes for a geometric topological insulator interfaced with a trivial insulator, constructed out of metal nanowires, adapted from [87] under CC BY 4.0 [88].

have uses in sensing [90], medicine [91, 92] and surface enhanced Raman scattering [93]. Some theory of electric fields in metallic nanoparticles will be covered in the next chapter.

SPPs can couple between waveguides or nanoparticles, allowing for similar behaviour to photonic crystals. This has applications in tuning of optical response [3], lasing [5], and waveguides [6–9]. Plasmonic arrays are therefore another interesting platform in which to study topological insulators. 2d topological insulators which make use of plasmons have been realised in theory and the real world [9, 86, 87, 94], alongside several 1d plasmonic TIs [95–97]. Some examples of experimental and theoretical descriptions of plasmonic TIs are shown in figure 1.7(c) and (d).

Loss and gain can be represented by imaginary parts in the dielectric tensor of the medium and in the frequency ω or wavevector $\mathbf{k}$ of the fields. In general, a photonic topological insulator is described by an effective Hamiltonian, which inherits some of these complex values. This can lead to the situation where the Hamiltonian is non-Hermitian. PTIs therefore provide a natural platform to explore non-Hermiticity in topological insulators, an extremely hot topic as of the late 2010s, which we discuss in the next section.

1.4 NON-HERMITICITY

Quantum mechanical Hamiltonians such as those of the original TIs were historically required to be Hermitian, where the Hamiltonian is equal to its Hermitian conjugate, $\mathcal{H} = \mathcal{H}^\dagger$. This is because Hermiticity forces the eigenvalues, which represent measurable quantities of the system, to be real valued. For a time it was believed that Hamiltonians which are non-Hermitian, $\mathcal{H} \neq \mathcal{H}^\dagger$, had no place in quantum mechanics.

However, non-Hermiticity has found its way into both quantum mechanical and classical Hamiltonians through a few different avenues [98]. One of the earliest examples comes from $\mathcal{PT}$-symmetry, where it was shown that certain non-Hermitian symmetries could still result in real eigenvalues. This led to the suggestion that the requirement of Hermiticity could be relaxed in closed quantum systems [99].

In general, non-Hermiticity arises when some kind of imaginary part is included in the Hamiltonian that does not respect the internal Hermitian symmetries of the matrix. This can happen in descriptions of open quantum systems, where the Hamiltonian is effective and describes only a part of the full system. To do this the Hamiltonian includes imaginary parts which describe losses to some external bath which are not otherwise captured in the description [100]. Even though such a system is presumably inside a larger closed Hermitian quantum system, it can sometimes be prohibitively difficult to describe this larger system. Imaginary parts can also appear in Hamiltonians when used to describe the lifetime of quasiparticles.

As shown in the previous section, classical physics also takes an approach where imaginary parts can be used to describe losses in an effective Hamiltonian, introducing non-Hermiticity. In fact, by constructing PCs with a careful balance of loss and gain, $\mathcal{PT}$-symmetry in TIs can be studied in theory and experiment using photonics [101–103].

Non-Hermiticity is an important phenomenon in the field of topological insulators, where it breaks several rules that Hermitian TIs follow. Without the symmetry constraint of Hermiticity, the tenfold way is no longer enough to classify Hamiltonians. What will replace it? Non-Hermiticity introduces the phenomenon of exceptional points, where Hamiltonians become defective and only have one eigenvector. What does this do to topology? Bulk-edge correspondence, one of the cornerstones of Hermitian topological physics, is also thrown into question, with topological invariants apparently no longer tied perfectly to edge states. How can this be understood or rectified? Some of these questions have yet to be fully answered at the time of writing, making it challenging to provide a comprehensive study. Once again we provide a short overview of the current state of the research, and recommend the review by Alvarez *et al.* [104], and papers by Kawabata *et al.* [105] and Zhou and Lee [106] for more complete summaries.

First we consider $\mathcal{PT}$-symmetry, which features some of the basic characteristics shared by non-Hermitian TI symmetries. The $\mathcal{PT}$-symmetry operator is the combination of the parity ($\mathcal{P}$) and time-reversal ($\mathcal{T}$) symmetry operators. The parity operator inverts spatial components, for example $\mathcal{P} : \mathbf{x} \mapsto -\mathbf{x}$, whereas time-reversal symmetry is equal to complex conjugation multiplied by a unitary matrix. The consequence is that the eigenvalues of a $\mathcal{PT}$-symmetric Hamiltonian, a Hamiltonian which commutes with the $\mathcal{PT}$ symmetry operator, are forced to be either real valued or complex conjugate pairs. In the real valued phase, eigenmodes of the Hamiltonian are also

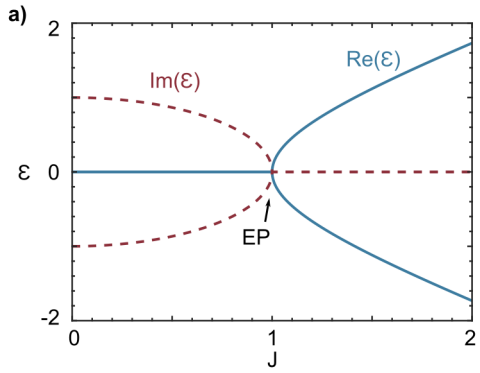

Figure 1.8: a) The exceptional point at $J = 1$ of the matrix featured in equation 1.4. The imaginary part of the eigenvalues are given by red dashed lines, and the real part by blue solid lines.

modes of the $\mathcal{PT}$-symmetry operator and the phase is called $\mathcal{PT}$-unbroken. In the complex conjugate pair phase, the Hamiltonian eigenmodes are not modes of the $\mathcal{PT}$ operator and the phase is called $\mathcal{PT}$-broken. Typically one can vary some parameter of the Hamiltonian to find an unbroken phase in one parameter region, and the broken phase in another. At the phase transition point we see an exceptional point.

For a very simple example of an exceptional point, consider the following matrix,

$$A = \begin{pmatrix} i & J \\ J & -i \end{pmatrix}, \tag{1.17}$$

where for simplicity we take J to be real valued, $J \in \mathbb{R}$. The eigenvalues of A are $\mathcal{E} = \pm\sqrt{J^2 - 1}$, with eigenvectors,

$$\mathbf{v} = \begin{pmatrix} J \\ \pm\sqrt{J^2 - 1} + i \end{pmatrix}. \tag{1.18}$$

For $J \neq 1$ the two eigenvectors are linearly independent and span two dimensions. When $|J| > 1$ the eigenvalues are real and for $|J| < 1$ the eigenvalues are complex conjugate pairs. However, when $|J| = 1$ there is only a single linearly independent eigenvector and there is said to be only one eigenvalue, $\mathcal{E} = 0$. At this exceptional point the matrix is called defective. Figure 1.8 shows a very simple demonstration of this matrix passing from a broken to unbroken phase through the exceptional point at $J = 1$. The exceptional point demonstrated here features the coalescence of 2 levels, but it is possible for more to be involved.

Exceptional points feature interesting properties that have made them something of a selling point of non-Hermitian systems. For example, in a loop around an exceptional point in phase space, choosing the clockwise or counterclockwise direction leads to different phases of the eigenvectors [107]. This chirality of the exceptional points is intrinsic and experimentally measurable [108]. Other exciting results of exceptional points include single-mode lasers [109], unidirectional invisibility [110], and enhanced optical sensitivity [111].

$\mathcal{PT}$-symmetry falls under a generalisation of Hermiticity known as pseudo-Hermiticity, where the bulk Bloch Hamiltonian has the property that

$$\mathcal{U}_\eta^\dagger \mathcal{H}^\dagger(\mathbf{q}) \mathcal{U}_\eta = \mathcal{H}(\mathbf{q}), \tag{1.19}$$

where $\mathcal{U}_\eta$ is unitary and Hermitian and squares to 1. The matrix in equation 1.4 falls under this symmetry. Hermiticity is a special case of this symmetry where $\mathcal{U}_\eta$ is the identity matrix. This is just one of the new non-Hermitian symmetries which do not fall under the classification of the ten-fold way discussed earlier. After much debate about non-Hermitian TI classification [112–114], Kawabata *et al.* [105] and Zhou and Lee [106] separately published periodic tables of non-Hermitian TIs which cover all possible symmetry classes. Here we explain the different symmetries, but the interested reader should look to their work for the actual periodic tables and how they were populated.

In addition to pseudo-Hermiticity, other symmetries emerge from the fact that under non-Hermiticity, $\mathcal{H} \neq \mathcal{H}^\dagger$, complex conjugation and the transpose are no longer the same thing, $\mathcal{H}^* \neq \mathcal{H}^\mathsf{T}$. Therefore we can take the original set of AZ symmetries,

$$\mathcal{T}: \qquad \mathcal{H} = \mathcal{U}_\mathsf{T}^\dagger \mathcal{H}^* \mathcal{U}_\mathsf{T}, \tag{1.20}$$

$$\mathcal{C}: \qquad \mathcal{H} = -\mathcal{U}_\mathsf{C}^\dagger \mathcal{H}^\mathsf{T} \mathcal{U}_\mathsf{C}, \tag{1.21}$$

$$\mathcal{S}: \qquad \mathcal{H} = -\mathcal{U}_\mathsf{S}^\dagger \mathcal{H} \mathcal{U}_\mathsf{S}, \tag{1.22}$$

and construct a new set by taking the Hermitian conjugate, $\mathrm{AZ}^\dagger$,

$$\mathcal{T}': \qquad \mathcal{H} = \mathcal{U}_\mathsf{T}^\dagger \mathcal{H}^\mathsf{T} \mathcal{U}_\mathsf{T}, \tag{1.23}$$

$$\mathcal{C}': \qquad \mathcal{H} = -\mathcal{U}_\mathsf{C}^\dagger \mathcal{H}^* \mathcal{U}_\mathsf{C}, \tag{1.24}$$

$$\mathcal{S}': \qquad \mathcal{H} = -\mathcal{U}_\mathsf{S}^\dagger \mathcal{H}^\dagger \mathcal{U}_\mathsf{S}. \tag{1.25}$$

The choice of complex conjugation and transposition in $\mathcal{T}$ and $\mathcal{C}$ follow the lead of Kawabata *et al.*, so that these correspond to the physical time-reversal and particle-hole symmetries [105]. In addition, $\mathcal{S}$ can be thought of as sublattice symmetry and $\mathcal{S}'$ as chiral symmetry, which are no longer the same in the context of non-Hermiticity. Another interesting thing to note is that under non-Hermiticity the $\mathcal{T}$ and $\mathcal{C}'$ classes are equivalent - one can see this by considering that for any Hamiltonian $\mathcal{H}$ satisying equation 1.20 there is a Hamiltonian $i\mathcal{H}$ which satisfies equation 1.24.

Overall the inclusion of all possible symmetries and behaviours of the $\mathcal{T}$, $\mathcal{C}$ and $\mathcal{S}$ and their Hermitian conjugate variants leads to a total of 38 symmetry classes. Kawabata *et al.* populated the table through use of K-theory [105], while Zhou and Lee used doubling of the non-Hermitian Hamiltonians to create one-to-one maps with Hermitian versions [106].

The obvious question might be, do the two 38 symmetry periodic tables agree with each other? The answer is complicated by the question of what it means for a non-Hermitian Hamiltonian to be 'gapped'. This is non-trivial because in general these systems have complex eigenvalues, which cannot be ordered.

Shen, Zhen and Fu proposed to extend the definition of band gaps in complex space to three different descriptions of bands. They described two bands, labelled by their subscript, as 'separable' if $\mathcal{E}_n(\mathbf{q}) \neq \mathcal{E}_m(\mathbf{q})$ for all $m \neq n$ and all $\mathbf{q}$, 'isolated' if $\mathcal{E}_n(\mathbf{q}) \neq \mathcal{E}_m(\mathbf{q}')$ for all $m \neq n$ and all $\mathbf{q}, \mathbf{q}'$ and 'inseparable' if $\mathcal{E}_n(\mathbf{q}) = \mathcal{E}_m(\mathbf{q})$ for

any **q** [115]. Zhou and Lee describe a gap as the non-crossing of some specified base point energy, as have others [114]. This is referred to as a point gap. Kawabata *et al.* use this type of gap, where the bands do not touch a base energy point, and another type where the bands do not touch a base energy line in complex space. This is called a line gap.

Kawabata *et al.* and Zhou and Lee do in fact agree on topological classifications for bands with point gaps. However, Kawabata *et al.* also provide topological classifications in the case of line gaps, which are different to the point gap classifications.

Non-Hermiticity also adds a complication to the calculation of topological invariants. For example, the Berry phase is now calculated using left and right eigenvectors of the bulk Bloch Hamiltonian. This will be relevant in chapter 3 of the thesis, where we consider a non-Hermitian system and its topological invariant.

One of the greatest challenges that has emerged in non-Hermitian TIs is that of bulk-edge correspondence. It has been shown in several simple non-Hermitian systems that the topological invariant does not always correspond to the existence or non-existence of edge states [116, 117]. This is made more complicated by the fact that the bulk spectrum can be highly sensitive to boundary conditions, with different bulk eigenvalues for infinite or open systems [118]. In addition, even bulk eigenmodes can be localised to the edge of the chain in a phenomenon called the 'non-Hermitian skin effect' [119]. Several examples of these are in one-dimensional tight binding models, which provide one of the simplest platforms to test ideas on.

Efforts to fix some of these problems include utilising different topological invariants [120], treating localised bulk modes as pseudo-Bloch states with complex k values [121] and using singular-value decomposition as opposed to calculating the eigensystem [122]. The question of BEC in non-Hermitian systems is a heavily debated one as of the late 2010s. We will discuss some of these options in chapter 4 of the thesis, where the question of bulk-edge correspondence becomes highly relevant to the system we study.

2 BACKGROUND THEORY

The previous chapter provided a general overview for anyone interested in the field of TIs, giving some important context for the rest of the thesis. In this chapter, we focus instead on the elements of theory needed for the work performed during the PhD.

The system we are ultimately interested in is a chain of metallic nanoparticles with alternating spacing. This has several parallels to the Su-Schrieffer-Heeger (SSH) model, which we therefore describe in some detail. We also cover some theory for metallic nanoparticles and their interaction with electric fields. We then address a simple plasmonic analogue for the SSH model introduced by Ling *et al* [96], which describes a chain of alternately spaced nanoparticles in the quasistatic (QS) limit. This indicates that the chain has topological properties, but the approximation has some significant limitations, which we examine. This puts us in good stead to develop further theory, beyond the QS approximation, in later chapters.

2.1 THE SSH MODEL

The SSH model was originally designed to describe the electronic properties of polyacetylene, an organic molecule with a backbone of carbon atoms joined by alternating single and double bonds [48]. Its diagrammatic chemical structure is shown in figure 2.1(a). In fact, this model is sometimes referred to as the simplest 1d topological insulator (TI), as we will now endeavor to explain. Much of this section is inspired by elements from J. K. Asbóth *et al.*'s 'A Short Course on Topological Insulators', which has been an invaluable resource for me during the PhD and would be an ideal place to find out more about electronic TIs for the interested reader [46].

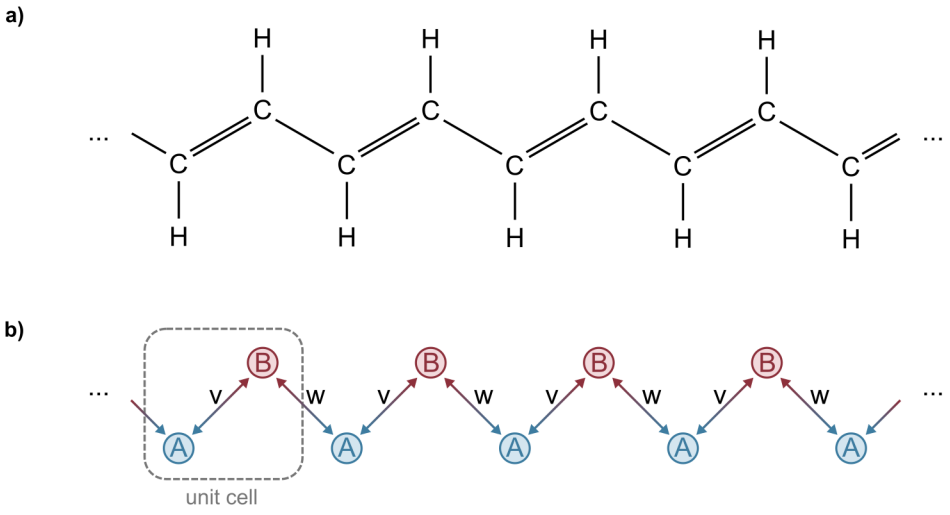

Figure 2.1: (a) Diagram of polyacetylene (b) Diagram of SSH model

Su, Schrieffer and Heeger described the electronic properties of polyacetylene with a tight binding model depicted in figure 2.1(b), where the electrons are non-interacting and move between lattice sites with staggered nearest neighbour hopping integrals. There are two sites per unit cell, with intracell hopping v and intercell hopping w representing the different bond types, leading to two sublattices labelled A and B. The Hamiltonian for a finite chain with N unit cells is

$$H_{SSH} = \sum_{n=1}^{N} (v|n, B\rangle\langle n, A| + \text{H.c.}) + \sum_{n=1}^{N-1} (w|n+1, A\rangle\langle n, B| + \text{H.c.}), \tag{2.1}$$

where $|n, A\rangle = |n\rangle|A\rangle$ and $|n, B\rangle$ represent states with an electron on unit cell n and sublattice A and B respectively. Here H.c. stands for 'Hermitian conjugate', meaning that the Hermitian conjugate of the other term is also included. The Hermitian conjugate takes a state $v|n', A\rangle\langle n, B|$ and sends it to $v^*|n, B\rangle\langle n', A|$, although in this case the hopping integrals are real so that $v = v^*$ and $w = w^*$. Spin is absent from the Hamiltonian as there are no spin specific interactions, so we have two copies of the Hamiltonian with opposite spins. However, as we are not particularly interested in this for our purposes, this is the last we will hear about this.

A finite length section of the SSH model (and any other condensed matter system) can be thought of as made up of two components; the edges and the stuff in between, which we call the bulk. It is common to consider the thermodynamic limit $N \to \infty$ and treat only the bulk, but in the case of TIs the behaviour at the edges is vital. The SSH model acts as a simple example to show how the two are intimately linked by bulk-edge correspondence (BEC).

2.1.1 Topological invariants in the bulk

First we study the bulk by considering the case of an infinite chain. The chain is translationally invariant, so the eigenstates are Bloch waves of the form,

$$|\Psi(q)\rangle = |q\rangle|u(q)\rangle, \tag{2.2}$$

where $|u(q)\rangle$ is the internal part of the wavefunction, which describes it in any one unit cell, and the external part $|q\rangle$ is given by Fourier transform,

$$|q\rangle = \sum_n e^{inqd_0}|n\rangle, \tag{2.3}$$

where d_0 is the lattice spacing. We define the bulk momentum-space Hamiltonian

$$\mathcal{H}_{SSH}(q) = \langle q|H_{SSH}|q\rangle, \tag{2.4}$$

which therefore has eigenstates $|u(q)\rangle$,

$$\mathcal{H}_{SSH}(q)|u(q)\rangle = \mathcal{E}(q)|u(q)\rangle. \tag{2.5}$$

Using equations 2.4 and 2.1 when $N \to \infty$ gives the bulk Hamiltonian,

$$\mathcal{H}_{SSH}(q) = v\left(|B\rangle\langle A| + |A\rangle\langle B|\right) + w\left(|A\rangle\langle B|e^{-iqd_0} + |B\rangle\langle A|e^{iqd_0}\right). \tag{2.6}$$

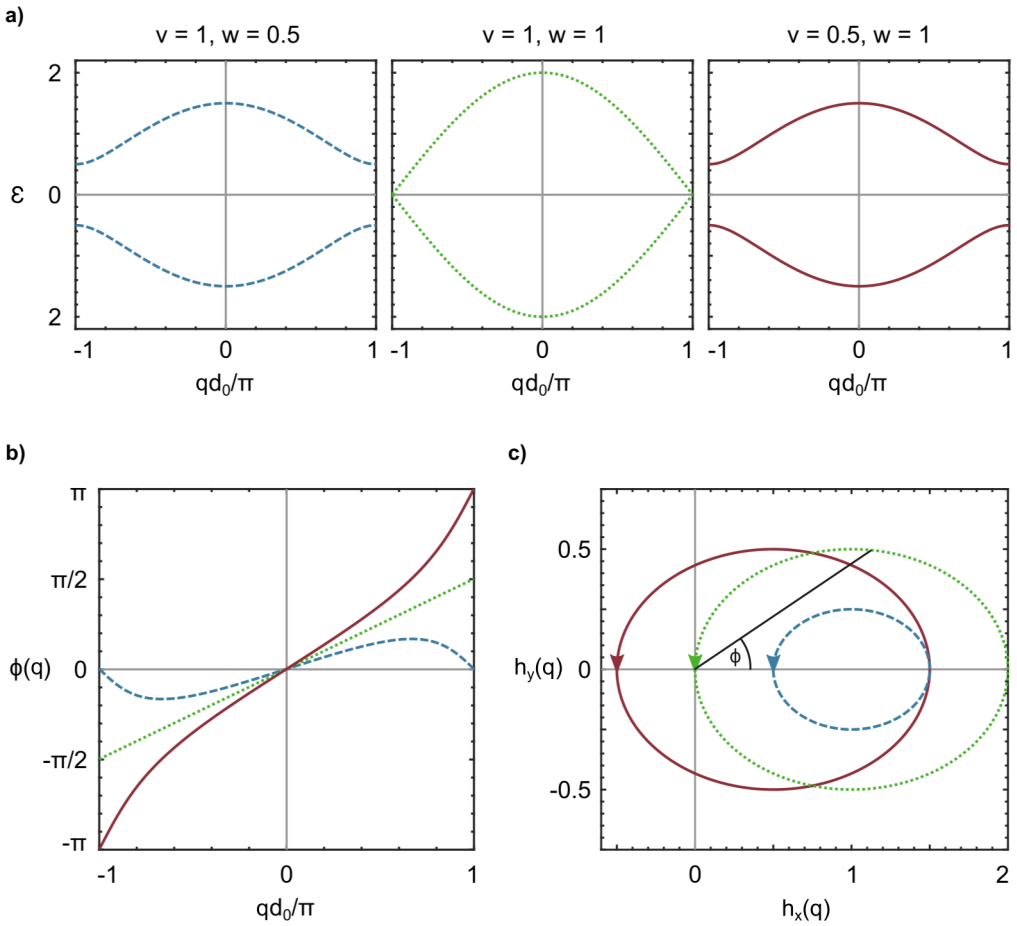

Figure 2.2: Bulk properties of the SSH model. (a) Eigenvalues for different choices of v and w. (b) $\phi(q)$, the phase difference between $a(q)$ and $b(q)$, across the BZ representing the Zak phase calculation for the lower band of the correspondingly coloured choices of v and w in (a).(c) $\mathbf{h}(q)$ for q sweeping across the BZ, representing the winding number of the lower band of the correspondingly coloured choices of v and w in (a).

The eigenstates can be written as combinations of A and B sublattice states, $|u(q)\rangle = a(q)|A\rangle + b(q)|B\rangle$. In matrix form we have

$$\mathcal{H}_{SSH}(q)|u(q)\rangle = \begin{pmatrix} 0 & v + we^{-iqd_0} \\ v + we^{iqd_0} & 0 \end{pmatrix} \begin{pmatrix} a(q) \\ b(q) \end{pmatrix} = \mathcal{E}(q) \begin{pmatrix} a(q) \\ b(q) \end{pmatrix}. \tag{2.7}$$

It's simple enough to solve this for the band structure or dispersion relation,

$$\mathcal{E}(q) = \pm\sqrt{v^2 + w^2 + 2vw\cos qd_0}, \tag{2.8}$$

which is shown for different choices of v and w in figure 2.2(a). The eigenvalues are symmetric when v and w swap values, and the band gap, given by $\Delta = |v - w|$, closes when $v = w$. As discussed in the previous chapter, topological phase transitions occur at band crossings, and this particular crossing is an example of such a phase transition.

The matrix has sublattice symmetry, $\sigma_z \mathcal{H}_{SSH}(q)\sigma_z = -\mathcal{H}_{SSH}(q)$, where σ_z is one of the Pauli spin matrices. The Pauli spin matrices, which are given by

$$\sigma_x = \begin{pmatrix} 0 & 1 \\ 1 & 0 \end{pmatrix}, \quad \sigma_y = \begin{pmatrix} 0 & -i \\ i & 0 \end{pmatrix}, \quad \sigma_z = \begin{pmatrix} 1 & 0 \\ 0 & -1 \end{pmatrix}, \tag{2.9}$$

are typically used to describe the spin of particles. In this thesis we will mostly use them to identify symmetry and in combination with the 2×2 identity matrix as a basis for the space of 2×2 matrices.

The sublattice symmetry causes the eigenvalue spectrum to be symmetric about $\mathcal{E} = 0$, because

$$\mathcal{H}_{SSH}(q)\sigma_z|u(q)\rangle = -\sigma_z \mathcal{H}_{SSH}(q)|u(q)\rangle = -\mathcal{E}(q)\sigma_z|u(q)\rangle. \tag{2.10}$$

The system also has inversion symmetry, which causes the spectrum to be symmetric in q, $\mathcal{E}(q) = \mathcal{E}(-q)$.

Recalling the Hermitian TI periodic table given in table 1.1, we can see that the SSH model falls under the Cartan symmetry classification BDI, indicating that we expect it to be a $\mathbb{Z}$ type topological insulator. There are two commonly used topological numbers of a 1d system like this in the literature: the Zak phase γ and the winding number $\mathcal{W}$. The Zak phase is the 1d version of the Berry phase, discussed in subsection 1.2.2, a geometric phase picked up by traversing the Brillouin Zone (BZ) [123]. It is given by

$$\gamma = i \int_{BZ} \langle u(q)|\frac{\partial}{\partial q}|u(q)\rangle dq. \tag{2.11}$$

If we consider the fact that, for a Hermitian Hamiltonian like $\mathcal{H}_{SSH}$, the normalised eigenvalues are of the form

$$|u(q)\rangle = \frac{1}{\sqrt{2}} \begin{pmatrix} e^{-i\phi(q)} \\ 1 \end{pmatrix}, \tag{2.12}$$

we can simplify this further to find that

$$\gamma = \frac{\phi(q = \pi/d_0) - \phi(q = -\pi/d_0)}{2} \mod 2\pi. \tag{2.13}$$

This phase can be calculated for each band by examining how it changes across the BZ, examples of which are presented in figure 2.2(b) for different v and w. The blue dashed line corresponding to $v > w$ leads to Zak phase $\gamma = 0$ while the red line corresponding to $v < w$ has $\gamma = \pi$. The vertical axis is periodic at π and $-\pi$ because ϕ is a phase, but this point could be shifted, so the important information is in whether ϕ completes a loop across the BZ or does not. We will see shortly that this information is captured in the winding number.

For this system, as long as $v \neq w$, the Zak phase is always quantised as either 0 or π. This is because the state $|u(q)\rangle$ must be equal at either side of the BZ, $|u(q = -\pi/d_0)\rangle = |u(q = \pi/d_0)\rangle$. From equation 2.12 we see that this requires the numerator in equation 2.13 to be some integer multiple of 2π. For the Zak phase to move between 0 and π the band gap has to close, as we see in the case of the green dotted line in

figure 2.2, corresponding to $v = w$. At the transition, $v = w$, there is only one particle per unit cell and the width of the BZ is doubled, so that the restriction on the state at $(q = -\pi/d_0)$ and $(q = \pi/d_0)$ is no longer there.

Throughout this work the choice of gauge means that $\gamma = 0$ is the Zak phase of free space, which has no topological properties and is therefore described as the 'trivial phase'. When $\gamma = \pi$, the system is in the 'topological phase'.

This formulation works in the case of the SSH model because there are is a maximum of one edge mode per edge, so higher topological numbers corresponding to more edges are not necessary. There are extensions of the SSH model which include longer range hopping terms for which the Zak phase is perhaps not the most useful number, as it will return $\gamma = 0$ for any even number of edge modes and $\gamma = \pi$ for any odd number.

How does this compare to the winding number $\mathcal{W}$? In the SSH model the winding number is typically defined using the fact that any 2×2 matrix can be written as a combination of the Pauli matrices,

$$\mathcal{H}(\mathbf{q}) = h_0(\mathbf{q})I + \mathbf{h}(\mathbf{q}) \cdot \boldsymbol{\sigma}, \tag{2.14}$$

where $\boldsymbol{\sigma} = (\sigma_x, \sigma_y, \sigma_z)$ is the vector of Pauli matrices and I is the identity matrix. The coefficients $h_0(\mathbf{q})$ and $\mathbf{h}(\mathbf{q}) = (h_x(\mathbf{q}), h_y(\mathbf{q}), h_z(\mathbf{q}))$ depend on the matrix, and in the case of the SSH model, the bulk Bloch Hamiltonian has

$$h_0(q) = 0, \tag{2.15}$$
$$h_x(q) = v + w\cos qd_0, \tag{2.16}$$
$$h_y(q) = w\sin qd_0, \tag{2.17}$$
$$h_z(q) = 0. \tag{2.18}$$

Consider the path of the vector $\mathbf{h}(q)$ as q traverses the BZ. Examples of this are provided in figure 2.2. The winding number $\mathcal{W}$ is given by the number of times this path winds around the origin, and we see that when $v > w$, given by the blue dashed line, the winding number is zero. When $v = w$ the dotted green line touches the origin and no winding number is defined. When $v < w$, the red solid line encircles the origin once, giving $\mathcal{W} = 1$. In this model it is impossible for the winding number to change without the path crossing the origin, corresponding to the closing of the gap. In this way the winding number is equal to the number of edge modes at each edge.

The winding number can be used to demonstrate that breaking the sublattice symmetry by addition of an $h_z(q)$ term causes the breakdown of the topological properties of the system. An $h_z(q)$ term would allow the path to move in an axis perpendicular to the $h_x(q)$-$h_y(q)$ plane depicted in figure 2.2(c). It would now be possible to move from a case where the path encircles the origin to one where the origin is outside of the path without crossing the origin. In other words, it would become possible to adiabatically transform the Hamiltonian from $\mathcal{W} = 1$ to $\mathcal{W} = 0$ without closing the gap, making the two phases equivalent, and the system topologically trivial.

Although we do not see it in this simple model, the winding number can pass around the origin multiple times or in the opposite direction, allowing for higher or

negative values. This makes it a more useful measurement than the Zak phase in the case of systems which allow for more edge modes.

We have seen that the two topological invariants are related by

$$\gamma = \pi\mathcal{W} \mod 2\pi. \tag{2.19}$$

This is due to their connection to $\phi(q)$, used in the calculation of the Zak phase, which also represents the angle that the point $(h_x(q), h_y(q)$ makes with the x axis at the origin, as depicted in figure 2.2(c).

In the case of a non-Hermitian extension of the system, it is a little clearer how to redefine the Zak phase than the winding number because complex valued $h_x(q)$ and $h_y(q)$ makes the concept of winding around an origin point less clear. One solution is to measure the winding of one of the off diagonal elements of the matrix around the origin in the complex plane, which is again equivalent to calculating the Zak phase [124].

2.1.2 Edge modes in the finite system

Now that we have examined the bulk properties of the SSH model, the next step is to consider a finite chain and study the edge modes. We refer to equation 2.1, which can be written in matrix form and produces a $2N \times 2N$ matrix. Eigenvectors of the matrix are of the form $|\Psi\rangle = (a_1, b_1, a_2, b_2, \cdots, a_N, b_N)^T$, where the subscript represents the unit cell. For example, for 3 unit cells we can write the eigenvalue equation in matrix form as

$$H_{SSH}|\Psi\rangle = \begin{pmatrix} 0 & v & 0 & 0 & 0 & 0 \\ v & 0 & w & 0 & 0 & 0 \\ 0 & w & 0 & v & 0 & 0 \\ 0 & 0 & v & 0 & w & 0 \\ 0 & 0 & 0 & w & 0 & v \\ 0 & 0 & 0 & 0 & v & 0 \end{pmatrix} \begin{pmatrix} a_1 \\ b_1 \\ a_2 \\ b_2 \\ a_3 \\ b_3 \end{pmatrix} = \mathcal{E} \begin{pmatrix} a_1 \\ b_1 \\ a_2 \\ b_2 \\ a_3 \\ b_3 \end{pmatrix}. \tag{2.20}$$

We can solve the finite chain eigenvalue equations for all 2N eigenvalues $\mathcal{E}$ and eigenvectors $|\Psi\rangle$.

Figure 2.3 summarises some of the results of interest. In figure 2.3(a), we fix $w = 1$ and vary v to visualise the transition between a topological phase $v < w$ and trivial phase $v > w$. The upper panel shows this for $N = 10$ chain, while the lower does so for an $N = 50$ chain.

Consider the fully dimerised limit at the left of the figures, where $v = 0$ and $w = 1$. In this case the sites at the left and right ends of the chain are fully disconnected, so they host zero energy edge states which exist at only these sites. As v increases the edge sites couple to the rest of the chain and the edge mode begins to spread slightly into the chain. Figure 2.3(b) shows the mode profile $|\Psi|$ of an edge mode in the gap at $v = 0.2$, where we see the modes exponentially confined to the edge of the chain. This corresponds to the red circle labelled b in the $N = 10$ chain in figure 2.3(a). There are two such modes in the centre of the gap with energy $\mathcal{E} = 0$, in the form of symmetric

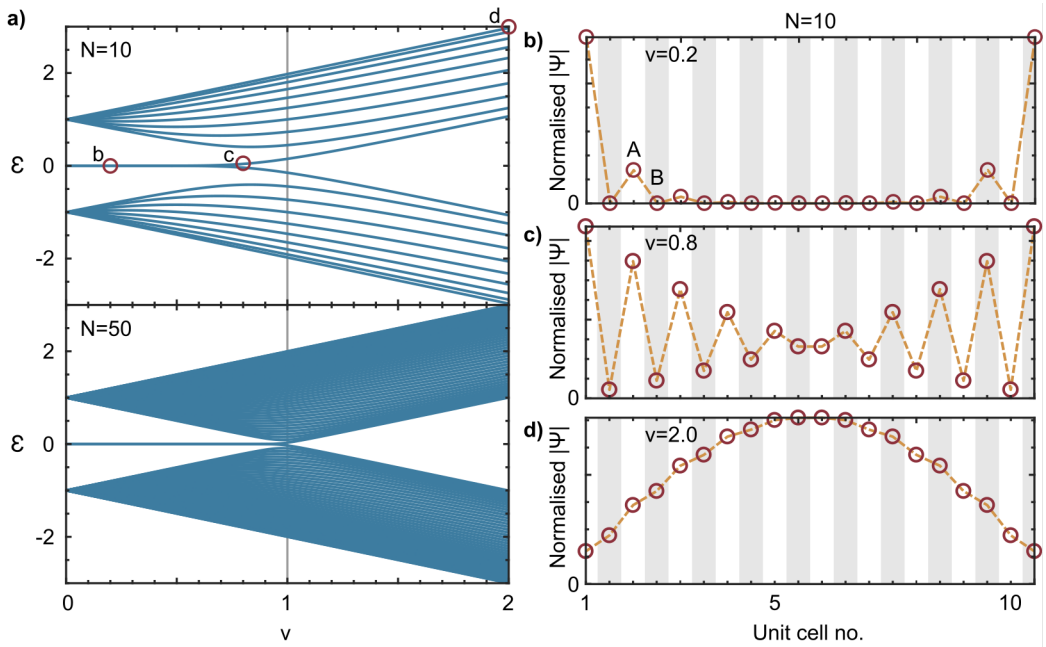

Figure 2.3: a) Eigenvalues of the finite SSH chain for fixed $w = 1$ and varying v, with $N = 10$ upper panel and $N = 50$ in the lower panel. b)-d) Normalised absolute values mode profiles for $N = 10$ chain, with white regions representing particles on the A sublattice and grey regions representing particles on the B sublattice. b) Edge modes for $v = 0.2$ indicated by red circle 'b' in (a) upper. c) Edge modes for $v = 0.8$ indicated by red circle 'c' in (a) upper. c) Bulk mode for $v = 2.0$ indicated by red circle 'd' in (a) upper.

and antisymmetric pairs. The left mode is confined completely to the A sublattice and the right mode is confined completely to the B sublattice.

As v increases the edge modes delocalise further into the chain and the bulk band gap begins to close. Figure 2.3(c) shows the same mode at $v = 0.8$, where the two edge modes have started to interact, allowing the energies to split and begin to leave the gap. This corresponds to the red circle labelled c in the $N = 10$ chain in figure 2.3(a). Comparing the $N = 10$ case to the $N = 50$ case we see that the edge modes begin to leave the gap a little earlier for a smaller chain due to finite size effects. If the chain is longer the edge modes must become more delocalised in order to couple and leave zero energy.

A phase transition happens at $v = 1$, and as v continues to increase there are no longer any modes in the gap. Figure 2.3(d) shows a typical bulk mode at $v = 2.0$, corresponding to the red circle labelled d in the $N = 10$ chain in figure 2.3(a). The bulk mode profiles look like standing waves on the chain.

To understand some of these observations we examine the finite Hamiltonian a little more. First we see that, like the bulk Hamiltonian, it features sublattice symmetry (SLS). In the finite case, the operator $\hat{\Sigma} = \sum_{n=1}^{N}(|n, A\rangle\langle n, A| - |n, B\rangle\langle n, B|)$ acts as the unitary operator $\mathcal{U}_S$ in equation 1.16. For example, if $N = 3$ the SLS operator, in matrix form, is given by

$$\Sigma = \begin{pmatrix} 1 & 0 & 0 & 0 & 0 & 0 \\ 0 & -1 & 0 & 0 & 0 & 0 \\ 0 & 0 & 1 & 0 & 0 & 0 \\ 0 & 0 & 0 & -1 & 0 & 0 \\ 0 & 0 & 0 & 0 & 1 & 0 \\ 0 & 0 & 0 & 0 & 0 & -1 \end{pmatrix}. \tag{2.21}$$

It is also useful to consider the projection operators for each sublattice A and B, given by $P_A = \sum_{n=1}^{N} |n, A\rangle\langle n, A|$ and $P_B = \sum_{n=1}^{N} |n, B\rangle\langle n, B|$. The SLS operator and the projection operators are related by $\Sigma = P_A - P_B$.

First we observe that eigenstates come in plus-minus pairs related by the SLS operator,

$$H_{SSH}\Sigma|\Psi\rangle = -\Sigma H_{SSH}|\Psi\rangle = -\mathcal{E}\Sigma|\Psi\rangle. \tag{2.22}$$

For eigenvalues which are non-zero, $\mathcal{E} \neq 0$, the SLS pair $|\Psi\rangle$ and $\Sigma|\Psi\rangle$ have different eigenvalues and are therefore orthogonal. This implies that the associated modes have equal support on the A and B sublattices,

$$0 = \langle\Psi|\Sigma|\Psi\rangle = \langle\Psi|P_A|\Psi\rangle - \langle\Psi|P_B|\Psi\rangle. \tag{2.23}$$

We see an example of this in figure 2.3(d), where the bulk mode has equal support in both sublattices.

For eigenvalues which are zero, $\mathcal{E} = 0$, eigenstates can be chosen to have support on only one sublattice, because

$$H_{SSH}P_\nu|\Psi\rangle = \frac{1}{2}H_{SSH}(1 \pm \Sigma)|\Psi\rangle = 0, \tag{2.24}$$

where ν is A or B. Zero energy eigenstates are SLS partners of themselves. Figure 2.3(b) shows a possible form of an edge mode of the chain, which has a corresponding antisymmetric partner. Since the eigenvalues of both of these modes are zero, linear combinations of the modes are also modes of the chain. Choosing an appropriate linear combination of these two modes allows us to isolate the edge modes so that the leftmost edge mode is supported only on the A sublattice, and the rightmost edge mode supported only on the B sublattice.

It is possible to find an approximate equation for the zero energy eigenstates of the SSH model by attempting to solve $H_{SSH}|\Psi\rangle = 0$, where we once again take $|\Psi\rangle = (a_1, b_1, a_2, b_2, \cdots, a_N, b_N)^T$. Doing so leads to the approximate solutions

$$|L\rangle = \sum_{m=1}^{N} a_m|m, A\rangle, \qquad |R\rangle = \sum_{m=1}^{N} b_m|m, B\rangle, \tag{2.25}$$

where a_m and b_m are given by

$$a_m = a_1 \left(\frac{-v}{w}\right)^{m-1} \tag{2.26}$$

$$b_m = b_N \left(\frac{-v}{w}\right)^{N-m} \qquad \forall m \in \{1, \ldots, N\}, \tag{2.27}$$

valid in the thermodynamic limit $N \to \infty$ [46]. This will come in handy later in the thesis.

2.1.3 Extensions and analogues

In this section, we have examined the SSH model, a simple 1d topological insulator with SLS. Its simplicity has made it very appealing for further study in the literature, with several extensions adding longer range hopping with higher winding numbers while preserving the SLS [125] or breaking it [126, 127]. The SSH model has been used as a basis to understand edge states in ribbons of graphene [128], and a 2d version with no Berry curvature but a vectorial Zak phase has been studied [129].

Non-Hermitian versions of the SSH model have also been proposed [130, 131], some preserving chiral symmetry [132] or introducing $\mathcal{PT}$-symmetry by applying opposite imaginary on-site potentials to the different sublattices [133–135]. This type of system has proved an invaluable tool for understanding and addressing some of the quirks of non-Hermiticity, and has led to proposed solutions to the breakdown of bulk-edge correspondence [119, 121, 122] and even a fractional topological number [124]. Some of these works will be relevant in chapter 4.

The SSH model and its extensions have also laid the groundwork for several photonic and plasmonic analogues in both theory and experiment [136], introducing staggered hopping using angles in zigzag chains [4, 95, 137] or staggered spacing between waveguides [138–141], interfaces of dielectrics, and nanoparticles [1, 5, 96, 142, 143].

One of these works, a study of edge states in a chain of metallic nanoparticles with alternating spacing by Ling *et al.* [96], led to the main work in this thesis. In order to understand how one would theoretically treat such a system, we first describe some theory of electromagnetically coupled nanoparticles.

2.2 SCATTERING OF LIGHT BY NANOPARTICLES

2.2.1 Mie theory and polarisability

In the 4^{th} century, ancient Roman glass workers produced the Lycurgus cup, a beautifully decorated piece with an interesting optical effect. As shown in figure 2.4, the colour of the glass of the cup is different for reflected or transmitted light due to the presence of gold and silver nanoparticles in a colloidal suspension in the glass [144]. Examples of the Roman ability to manufacture this material are rare, and the craft was short lived. Nonetheless, it is an impressive display of the possibilities afforded by the manipulation of light by nanoparticle scattering.

It was not until the late 19^{th} century, when Lord Rayleigh mathematically described the field scattered by a very small particle, compared to the wavelength, that a theoretical understanding of such behaviour began to develop [145]. Further work by Thomson, Love, Lorenz, Debye and Mie [146] culminated in Mie's 1908 paper on the field scattered by a sphere of any radius a subject to an incident monochromatic plane wave with wavelength λ [147]. In this treatment, Maxwell's equations are satisfied both inside and outside the particle, and the scattered field is expanded in terms of spherical harmonics. The coefficients of the expansion can then be determined by ensuring continuity of the tangential field at the interface between the particle and the embedding medium, known as a boundary value problem. The expressions for the Mie coefficients contain several special functions which are quite cumbersome, and overall they are not very enlightening. For this reason we will omit them and point the interested reader to one of the several texts in which they are featured [147–149].

Mie's original figures, sketches representing the vector spherical harmonics which make up each term of the expansion of the electric field, are given in figure 2.5. They correspond to the transverse components of the electric field lines of each mode at a fixed radial distance outside the particle. Each term in the Mie expansion is a linear combination of two vector spherical harmonics, one of which has no radial magnetic field component (upper) and one which has no radial electric field component (lower). They are therefore sometimes referred to as transverse magnetic and transverse electric modes, respectively [148].

In a metallic sphere, the incoming electric field affects the electrons near the surface of the particle, setting up localised surface plasmon modes, as discussed in section 1.3. The resultant effect is primarily electric, unlike the potential magnetic properties of a dielectric particle [149]. Therefore the focus of this work is on electric fields, although it is easy to apply many of the results to magnetically active systems. In this work we set the relative background magnetic permeability to $\mu = 1$.

To further simplify matters, we work in the limit of a small particle relative to the wavelength, $a \ll \lambda$. Scattering of light by small particles is often called Rayleigh scattering due to Rayleigh's simple treatment of this phenomenon [145]. From the perspective of Mie theory, in the small particle limit the first order transverse magnetic term, shown in the upper panel in figure 2.5(a), dominates in the expansion for

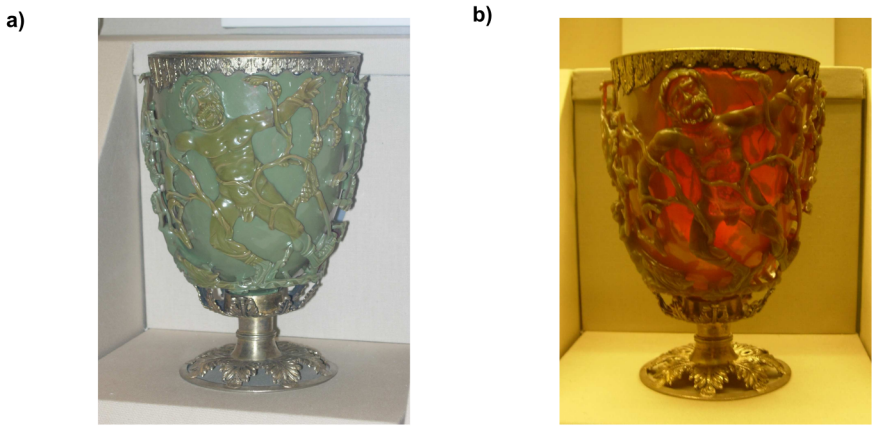

Figure 2.4: The famous Lycurgus cup, lit from a) the outside and b) the inside. Photos taken by José Sánchez-Gil.

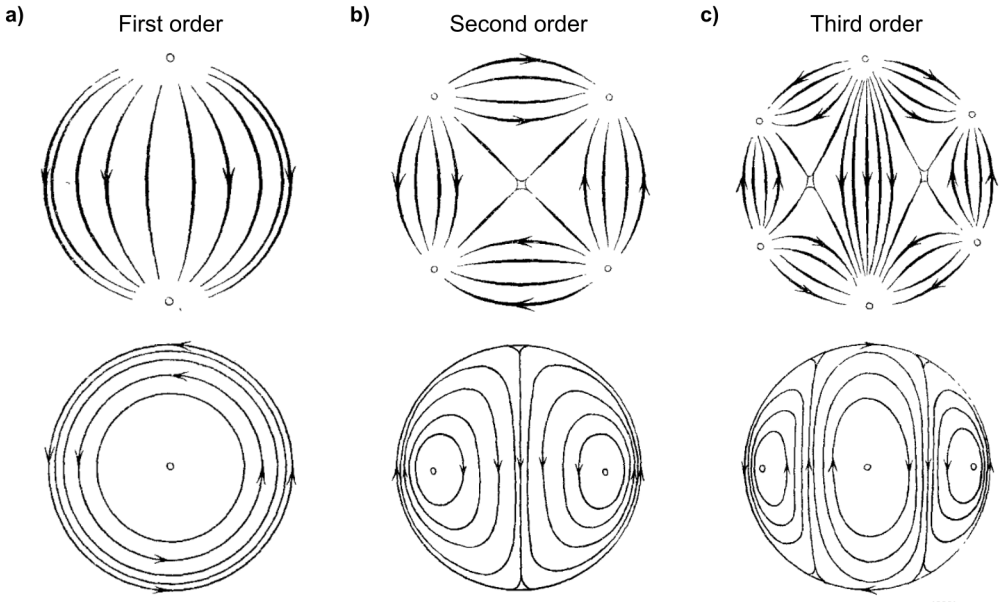

Figure 2.5: Field lines of the a) first, b) second and c) third order terms in the vector spherical harmonic expansion of a field scattered by a particle, adapted from Mie, Beiträge zur Optik trüber Medien, speziell kolloidaler Metallösungen, John Wiley and Sons. Copyright 1908 WILEY-VCH Verlag GmbH & Co. KGaA, Weinheim [147].

a single sphere. The scattered field by such a particle is therefore approximately the same as that of a dipole.

When we consider multiple spheres, their proximity is important because they are affected by each other's scattered fields, causing the dipolar approximation to worsen as the particles get closer. As long as the centres of particles are separated by a minimum distance of around $3a$, higher order terms in the Mie expansion are fairly insignificant [150]. In order to work in this dipolar limit we use small particles compared to the wavelength and keep particles at a minimum separation of $3a$.

Before introducing any equations it is worth noting that different authors use different conventions for the inclusion of certain constants like the electric permittivity of free space, ϵ_0. This is because these constants often cancel out, and can therefore be included or not included as long as the work is self-consistent.

The relationship between the electric field $\mathbf{E}$ at the nanoparticle's position and the dipole moment $\mathbf{p}$ is given simply by

$$\mathbf{p} = \epsilon_B \alpha(\omega)\mathbf{E}, \tag{2.28}$$

where $\alpha(\omega)$ is the polarisability of the nanoparticle as a function of the frequency of the light ω [148]. The background material is captured by ϵ_B, its relative permittivity. The polarisability $\alpha(\omega)$ must therefore encode all the information about the particle such as its size, shape and material properties. It can be a 3×3 matrix when the particle is not a uniform shape, but for our purposes of spherical particles it is scalar, or sometimes thought of as a scalar multiplied by the identity matrix.

An electrostatic, or quasistatic (QS), expression for the polarisability of a sphere can be derived by considering the first Mie coefficient in the limit of a very small particle $a \ll \lambda$. It is given by

$$\alpha_{QS}(\omega) = 4\pi\epsilon_0 a^3 \frac{\epsilon(\omega) - \epsilon_B}{\epsilon(\omega) + 2\epsilon_B}. \tag{2.29}$$

Here $\epsilon(\omega)$ is the dielectric function of the sphere, which can be experimentally measured or approximated simply using the Drude model,

$$\epsilon(\omega) = \epsilon_\infty - \frac{\omega_P^2}{\omega^2 + i\omega/\tau}, \tag{2.30}$$

where ϵ_∞ is the high frequency permittivity limit, ω_P is the bulk plasmon frequency, and τ is the decay time of plasmon excitations. From equation 2.29 it is clear that there is a surface plasmon resonance when the denominator $\epsilon(\omega) + 2\epsilon_B$ is zero. This QS surface plasmon resonance frequency is given by $\omega_{sp} = \omega_P/\sqrt{\epsilon_\infty + 2\epsilon_B}$.

The QS polarisability is a reasonable approximation for particles below $a = 10\,\text{nm}$, but it violates the optical theorem, which relates the extinct power, where $\mathtt{extinction} = \mathtt{absorption} + \mathtt{scattering}$, to the forward scattered field. This is because in the QS limit the extinct and absorbed power are equal, which means the scattered power is completely neglected.

One reason for this is that the QS polarisability fails to take into account the self interaction between the electromagnetic radiation caused by the movement of the electrons and the electrons themselves. This interaction causes a phase lag between the oscillations of the driving field and the oscillation of the electrons in the sphere. The resultant damping on electron motion is called radiative damping. It is possible to find the radiative damping force on the electrons by introducing it in the harmonic oscillator equation [151], and from this an effective polarisability called the radiative correction can be derived,

$$\alpha_R(\omega) = \frac{\alpha_{QS}(\omega)}{1 - i\frac{k^3}{6\pi\epsilon_0}\alpha_{QS}(\omega)}, \tag{2.31}$$

where $k = \sqrt{\epsilon_B}\omega/c = \sqrt{k_x^2 + k_y^2 + k_z^2}$ is the magnitude of the wavevector in the embedding medium. This improved polarisability description satisfies the optical theorem and is useful for slightly larger particles, up to around $a = 30\,\text{nm}$.

This correction misses a final ingredient, where the electric field depolarises as it moves over the surface of the particle. This effect, called dynamic depolarisation, causes a red shift of the particle resonance, which increases as the particle becomes larger [152, 153]. It can be shown that to first order the dynamic depolarisation adds another term to the effective polarisability [154], now called the modified long wavelength approximation (MLWA),

$$\alpha_{MLWA}(\omega) = \frac{\alpha_{QS}(\omega)}{1 - i\frac{k^3}{6\pi\epsilon_0}\alpha_{QS}(\omega) - \frac{k^2}{4\pi\epsilon_0 a}\alpha_{QS}(\omega)}. \tag{2.32}$$

Different polarisabilities can be chosen depending on the particle dimensions we are interested in.

One way to analyse the effect of a particle on an electromagnetic field is to calculate its extinction cross section. For a single particle using the dipole approximation this is given by the optical theorem [148] as

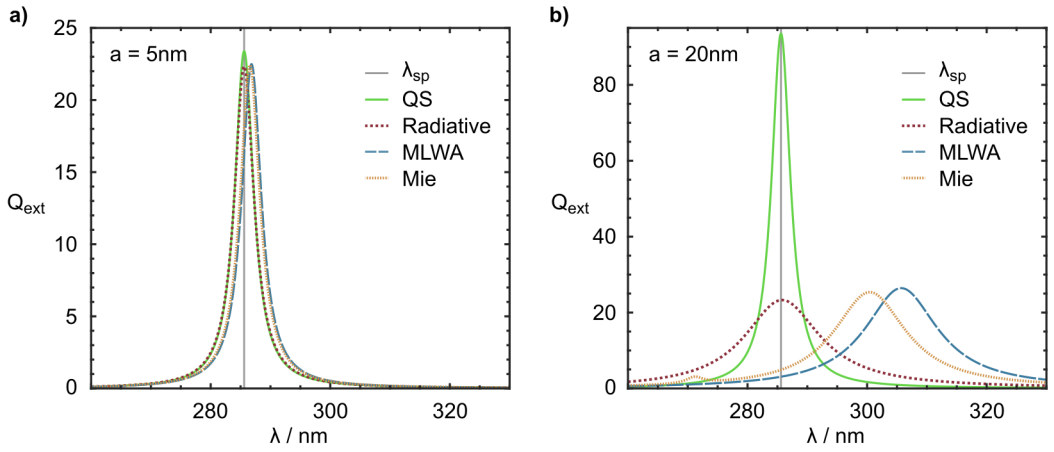

Figure 2.6: Extinction cross section of a silver particle in glass for different calculations of the polarisability, compared to Mie theory, for particles of size a) $a = 5\,\text{nm}$ and b) $a = 20\,\text{nm}$. Mie extinction calculated using code translated from appendix A of Bohren and Huffman [148] by Markowicz [155].

$$C_{ext} = \frac{k}{\epsilon_0}\text{Im}[\alpha(\omega)]. \tag{2.33}$$

The extinction efficiency is then given by the cross section divided by the particle's spacial cross section, in this case $Q_{ext} = C_{ext}/\pi a^2$.

Figure 2.6 shows the theoretical extinction efficiencies for the three different polarisabilities, for particles of size (a) $a = 5\,\text{nm}$ and (b) $a = 20\,\text{nm}$. It also features the extinction efficiency calculated by Mie theory for these same particles. The particles use Drude parameters for silver, $\epsilon_\infty = 5$, $\omega_P = 1.36 \times 10^{16}\,\text{rad/s}$, $1/\tau = 5.88 \times 10^{13}\,\text{rad/s}$ [156] and are embedded in glass, giving background dielectric constant $\epsilon_B = 2.25$. The figure clearly shows that for smaller particles $a = 5\,\text{nm}$ the three polarisabilities are not significantly different, but as the particles grow they begin to diverge. For $a = 20\,\text{nm}$, the radiative correction (red dots) shows a significant decrease in the strength of the resonance compared to the QS polarisability (green solid lines). It is also smeared out in frequency or wavelength. However, its peak is in a similar location to the QS resonance wavelength $\lambda_{sp} = 2\pi c/\sqrt{\epsilon_B}\omega_{sp}$ (grey line), at approximately $\lambda = 286\,\text{nm}$ for this choice of parameters. The inclusion of the depolarisation correction red shifts the peak in the MLWA case (blue dashed), with greater shifts for larger particles. This compares favourably with the full Mie extinction efficiency (yellow dots). However, in the Mie expansion, for $a = 20\,\text{nm}$, a higher order peak is visible at $\lambda = 271\,\text{nm}$, which is not predicted by the polarisabilities. This peak increases in size as the particle becomes larger.

In order to understand how to treat multiple scattering particles, we need a description of the scattered electric field outside of the particle. We will use the Green's dyadic for this purpose.

2.2.2 Electromagnetic Green's dyadic and coupled dipoles

Mathematically, Green's functions are solutions of linear ordinary differential equations (ODEs), which can be used to solve the same system with a different driving

function. Consider an arbitrary linear differential operator $\mathcal{L}$ and driving function $f(x)$,

$$\mathcal{L}u(x) = f(x), \tag{2.34}$$

which is a linear ODE with solution $u(x)$. Then the corresponding differential equation for the Green's function is

$$\mathcal{L}g(x,s) = \delta(x-s), \tag{2.35}$$

where $g(x,s)$ is the Green's function and $\delta(x-s)$ is the well known delta function.

Imagine that we have solved equation 2.35 for the Green's function. If we multiply both sides by any driving function $f(s)$ and integrate we have

$$\int \mathcal{L}g(x,s)f(s)\,ds = \int \delta(x-s)f(s)ds. \tag{2.36}$$

On the left hand side, $\mathcal{L}$ is linear, so it can be brought out of the integral. The right hand side evaluates to $f(x)$, so that

$$\mathcal{L}\int g(x,s)f(s)\,ds = f(x). \tag{2.37}$$

Comparing this to equation 2.34 it is clear that

$$u(x) = \int g(x,s)f(s)\,ds. \tag{2.38}$$

This can be a powerful tool for solving ODEs in general.

In this specific case we are interested in solving the homogeneous, or free, space vector wave equation, given by

$$\nabla\times\nabla\times\mathbf{E}(\mathbf{r}) - k^2\mathbf{E}(\mathbf{r}) = \frac{i\omega}{\epsilon_0 c^2}\mathbf{j}(\mathbf{r}), \tag{2.39}$$

where $\mathbf{j}(\mathbf{r})$ is the charge current density [151].

The electric field $\mathbf{E}(\mathbf{r})$ is a vector, so the corresponding Green's function must relate a vectorial input to a vectorial output, and is therefore a second order tensor, called a dyadic. In this thesis the notation for a dyadic will be a capital letter, although in double bars or arrows are often used in other works. The homogeneous space Green's function version of the vector wave equation is

$$\nabla\times\nabla\times G(\mathbf{r},\mathbf{r}') - k^2 G(\mathbf{r},\mathbf{r}') = I\delta(\mathbf{r}-\mathbf{r}'). \tag{2.40}$$

where G is the Green's dyadic and I is the identity dyadic.

It can be shown that the solution is given by

$$G(\mathbf{r},\mathbf{r}') = \left[1 + \frac{1}{k^2}\nabla\otimes\nabla\right] g(\mathbf{r},\mathbf{r}'), \tag{2.41}$$

where $\otimes$ represents the outer product, and $g(\mathbf{r},\mathbf{r}')$, called the scalar free space Green's function, solves the scalar Helmholtz equation,

$$-\left[k^2 + \nabla^2\right] g(\mathbf{r},\mathbf{r}') = \delta(\mathbf{r}-\mathbf{r}'), \tag{2.42}$$

which leads to

$$g(\mathbf{r},\mathbf{r}') = \frac{e^{\pm ik|\mathbf{r}-\mathbf{r}'|}}{4\pi|\mathbf{r}-\mathbf{r}'|}. \tag{2.43}$$

For convenience we will define $\mathbf{R} = \mathbf{r}-\mathbf{r}'$ and $R = |\mathbf{R}|$. Evaluating equation 2.41 finally gives

$$G(\mathbf{r},\mathbf{r}') = \frac{e^{ikR}}{4\pi k^2 R^3}\left[-\left(1-ikR-k^2R^2\right)I + \left(3-3ikR-k^2R^2\right)\frac{\mathbf{R}\otimes\mathbf{R}}{R^2}\right]. \tag{2.44}$$

This gives us a solution to the homogeneous space vector wave equation for the electric field outside of any volume V containing arbitrary charge current density $\mathbf{j}(\mathbf{r})$, given by

$$\mathbf{E}(\mathbf{r}) = \mathbf{E}_I(\mathbf{r}) + \frac{i\omega}{\epsilon_0 c^2}\iiint_V G(\mathbf{r},\mathbf{s})\mathbf{j}(\mathbf{s})\,d\mathbf{s}, \qquad \mathbf{r}\notin V, \tag{2.45}$$

where $\mathbf{E}_I$ is the incident electric field. This equation fails for $\mathbf{r}$ inside the volume because of the pole at $\mathbf{r}=\mathbf{s}$, but it is possible to treat the field inside as well. Solving this equation can be prohibitively difficult for an arbitrary scatterer, but for a dipole it is remarkably simple. A dipole at position $\mathbf{r}_0$ has charge current density $\mathbf{j}(\mathbf{r}) = -i\omega\mathbf{p}_0\delta(\mathbf{r}-\mathbf{r}_0)$, which therefore radiates an electric field given by

$$\mathbf{E}(\mathbf{r}) = \frac{k^2}{\epsilon_0\epsilon_B}G(\mathbf{r},\mathbf{r}_0)\mathbf{p}_0. \tag{2.46}$$

We have arrived at a physical interpretation of the electric Green's function. Its x, y and z columns are proportional to the electric field radiated by a dipole aligned in the x, y and z directions. The reciprocity of Maxwell's equations also gives it the property that $G(\mathbf{r},\mathbf{r}') = G(\mathbf{r}',\mathbf{r})$.

The Green's function can be broken up into near, intermediate and far field components, $G = G_n + G_i + G_f$, which decay at a $\sim 1/R^3$, $\sim 1/R^2$ and $\sim 1/R$ rate respectively, given by

$$G_n(\mathbf{r},\mathbf{r}') = \frac{e^{ikR}}{4\pi}\frac{1}{k^2R^3}\left[-I+3\frac{\mathbf{R}\otimes\mathbf{R}}{R^2}\right], \tag{2.47}$$

$$G_i(\mathbf{r},\mathbf{r}') = \frac{e^{ikR}}{4\pi}\frac{i}{kR^2}\left[I-3\frac{\mathbf{R}\otimes\mathbf{R}}{R^2}\right], \tag{2.48}$$

$$G_f(\mathbf{r},\mathbf{r}') = \frac{e^{ikR}}{4\pi}\frac{1}{R}\left[I-\frac{\mathbf{R}\otimes\mathbf{R}}{R^2}\right]. \tag{2.49}$$

For N dipoles at positions $\mathbf{r}_j$ in space and an incident field, the total electric field is

$$\mathbf{E}(\mathbf{r}) = \mathbf{E}_I(\mathbf{r}) + \frac{k^2}{\epsilon_0\epsilon_B}\sum_{j=1}^{N}G(\mathbf{r},\mathbf{r}_j)\mathbf{p}_j. \tag{2.50}$$

This equation can be applied to systems with an arbitrarily shaped piece of homogeneous material embedded in another by breaking the embedded material into tiny volume elements, and treating each as a dipole. This semi-analytical method is called

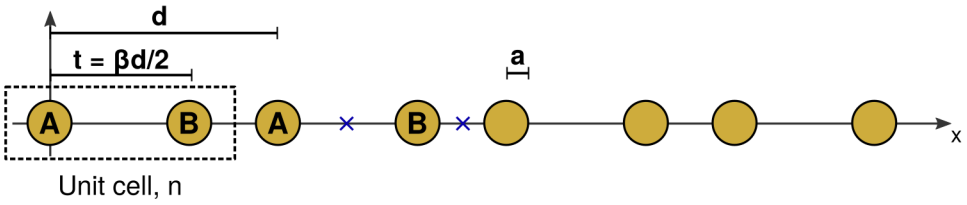

Figure 2.7: Diagram of the topological plasmonic chain, adapted from [1]

the coupled dipole approximation [151]. We derive a set of equations relating the dipole moments at each particle by considering the electric field at the positions of each particle, setting the incident electric field to zero, and applying the relationship between an electric field and the dipole moment in equation 2.28. The resultant N equations are

$$\frac{1}{\alpha(\omega)}\mathbf{p}_n = \frac{k^2}{\epsilon_0}\sum_{j=1}^{N}{}' G(\mathbf{r}_n, \mathbf{r}_j)\mathbf{p}_j, \tag{2.51}$$

where the prime notation on the sum means that the $j = n$ term is skipped. Fittingly these are called the coupled dipole equations (CDEs).

The final useful tool to establish in this section is the extinction cross section for any set of N dipoles, which is given by

$$C_{ext} = \frac{k}{\epsilon_0 \epsilon_B |\mathbf{E}_0|^2}\sum_{j=1}^{N} \mathrm{Im}[\mathbf{E}_I^*(\mathbf{r}_j)\cdot\mathbf{p}_j], \tag{2.52}$$

With that, we are finally in a position to understand the QS plasmonic SSH model.

2.3 A QUASISTATIC PLASMONIC SSH MODEL ANALOGUE

Although there are more than one QS plasmonic SSH model analogue in the literature, we focus on Ling *et al.*'s model [96], which uses the CDEs and then the QS limit $kd \ll 1$ to simplify the Green's functions [157]. As we will see, this QS approximation has serious limitations in its ability to accurately describe such a system. This motivates the remaining chapters of the thesis, in which the system is treated in detail beyond the QS limit.

2.3.1 The model

The system of interest is a chain of metallic nanoparticles with alternating spacing, depicted in figure 2.7. The particles are centered on the x axis. Each unit cell contains two nanoparticles, labelled A and B, with unit cell spacing d and an internal spacing $t = \beta d/2$ between the A and B particles of the same unit cell. This causes the spacing to be staggered when $\beta \neq 1$. Importantly, we require that the spacing is such that $t \geqslant 3a$ and $d - t \geqslant 3a$, so that the nanoparticles act as coupled dipoles. This will allow us to apply the CDEs in equation 2.51.

Ling *et al.* considered only nearest neighbours, so that any coupled dipoles have $R < d$ spacing. In this context we apply the QS limit, $kd \ll 1$, and the free space Green's dyadic becomes

$$G_{QS}(\mathbf{r}, \mathbf{r}') = \frac{1}{4\pi k^2 R^3}\left[-I + 3\frac{\mathbf{R}\otimes\mathbf{R}}{R^2}\right]. \tag{2.53}$$

This is similar to the near field part of the Green's dyadic, except the phase information caused by the finite speed of light is lost, $\exp(ikR) \mapsto 1$. Note that this is real valued for any $\mathbf{R}$ and real valued k. The chain is confined to the x axis, so the Green's dyadic becomes diagonal, decoupling the x, y and z components of the dipolar moments. We call the x components longitudinal as they lie in the axis of the chain, and the y and z components transverse. The non-zero scalar components of the QS Green's dyadic are then given by

$$G^{xx}_{QS}(\mathbf{r}, \mathbf{r}') = \frac{2}{4\pi k^2 R^3}, \tag{2.54}$$

$$G^{yy}_{QS}(\mathbf{r}, \mathbf{r}') = G^{zz}_{QS}(\mathbf{r}, \mathbf{r}') = \frac{-1}{4\pi k^2 R^3}. \tag{2.55}$$

Finally we relabel the particles so that $\mathbf{p}^A_n$ and $\mathbf{p}^B_n$ are the dipole moments of particle A and B in unit cell n respectively. We use $\nu = x, y$ or z to label the three components of the dipole. Taking only nearest neighbours for a chain with N unit cells we arrive at the following system of equations,

$$\frac{1}{\alpha(\omega)}p^A_{\nu,n} = \frac{2m_\nu}{\pi\epsilon_0 d^3}\left[\frac{p^B_{\nu,n}}{\beta^3} + \frac{p^B_{\nu,n-1}}{(2-\beta)^3}\right], \tag{2.56}$$

$$\frac{1}{\alpha(\omega)}p^B_{\nu,n} = \frac{2m_\nu}{\pi\epsilon_0 d^3}\left[\frac{p^A_{\nu,n}}{\beta^3} + \frac{p^A_{\nu,n+1}}{(2-\beta)^3}\right], \tag{2.57}$$

where $m_\nu = 2$ when $\nu = x$ and $mu_\nu = -1$ when $\nu = y, z$, and $p^{A,B}_{\nu,n} = 0$ for $n \leqslant 0$ or $n > N$ to enforce open boundary conditions. Notably Ling *et al.* used only the longitudinal polarisation for their study, because the transverse polarisation is not as well described by a quasistatic approach for equally spaced chains, as we will discuss later. For now we cover the theory for both since the only difference between the two polarisations in the QS case is the prefactor $m_\nu = 2$.

Although it is obscured a little by notation, there is already a direct mapping between this system and the finite SSH Hamiltonian eigenvalue equation $H_{SSH}|\Psi\rangle = \mathcal{E}|\Psi\rangle$. In this plasmonic system the eigenvector is instead given by $(p^A_{\nu,1}, p^B_{\nu,1}, \ldots, p^A_{\nu,N}, p^B_{\nu,N})^T$, the eigenvalues by $\mathcal{E} = 1/\alpha(\omega)$, and the intra and intercell hopping parameters by

$$v \mapsto \frac{2m_\nu}{\pi\epsilon_0 d^3}\frac{1}{\beta^3}, \qquad w \mapsto \frac{2m_\nu}{\pi\epsilon_0 d^3}\frac{1}{(2-\beta)^3}. \tag{2.58}$$

In the case of a bulk chain, the correspondence is similar. Using an infinite chain and applying Bloch's theorem to the plasmonic system yields

$$\begin{pmatrix} 0 & f(q_x) \\ f^*(q_x) & 0 \end{pmatrix} \begin{pmatrix} p_\nu^A \\ p_\nu^B \end{pmatrix} = \frac{1}{\alpha(\omega)} \begin{pmatrix} p_\nu^A \\ p_\nu^B \end{pmatrix}, \tag{2.59}$$

where the Bloch momentum, q_x, is the x component of the Bloch wavevector $\mathbf{q}$, and

$$f(q_x) = \frac{2m_\nu}{\pi\epsilon_0 d^3}\left[\frac{1}{\beta^3} + \frac{1}{(2-\beta)^3}e^{-iq_x d}\right]. \tag{2.60}$$

It is simple to see that this is extremely similar to the Bloch Hamiltonian eigenvalue equation for the the SSH model, equation 2.7, by way of the map in equations 2.58. The matrix in the above equation acts as effective Hermitian Bloch Hamiltonian with SLS, identical to the SSH model. Its eigenvectors can be mapped directly onto those of the SSH model, bestowing exactly the same topological properties. Now instead of the ratio v/w, the dimensionless chain parameter β controls the topological properties of this system. If $\beta < 1$ the system is trivial, and if $\beta > 1$ it is topological, so that a phase transition between the two occurs when the bands cross at $\beta = 1$.

One significant difference between the SSH model and its plasmonic analogue is that in the electronic system the energy is given by the eigenvalues $\mathcal{E}$, but in the plasmonic analogue the physical component of interest is the frequency ω. This can be calculated from the eigenvalue $\mathcal{E} = 1/\alpha(\omega)$. Ling *et al.* used the QS polarisability from equation 2.29 and the Drude model, equation 2.30, to reach the following equation for the frequency dispersion,

$$\omega = \frac{-i}{2\tau} + \sqrt{\frac{-1}{4\tau^2} + \frac{\omega_P^2(1 \pm 4\pi a^3\epsilon_0\sqrt{f(q_x)f^*(q_x)})}{(\epsilon_\infty + 2\epsilon_B) \pm 4\pi a^3\epsilon_0(\epsilon_\infty - \epsilon_B)\sqrt{f(q_x)f^*(q_x)}}}, \tag{2.61}$$

although Ling *et al.* used $\epsilon_\infty = 1$ and set the background medium to be air, $\epsilon_B = 1$, which simplifies the expression significantly to

$$\omega = \frac{-i}{2\tau} + \sqrt{\frac{-1}{4\tau^2} + \frac{\omega_P^2}{3}(1 \pm 4\pi a^3\epsilon_0\sqrt{f(q_x)f^*(q_x)})}. \tag{2.62}$$

The eigenvalues $1/\alpha_{QS}(\omega)$ have the same properties as the SSH model in that they exist in plus-minus pairs around $1/\alpha_{QS}(\omega) = 0$, and edge modes sit at $1/\alpha_{QS}(\omega) = 0$. When the damping is zero, $\tau \to \infty$, the frequency dispersion is real and exists in plus-minus pairs either side of the surface plasmon resonance frequency $\omega_{sp} = \omega_P/\sqrt{3}$. Introducing Drude damping distorts the real part of the frequency bands slightly and adds an imaginary part, but the effective Hamiltonian remains Hermitian and $1/\alpha(\omega)$ is still real valued.

2.3.2 Limitations

The QS approximation used above ignores the phase properties caused by the speed of light, called retardation, and the inherently long range nature of the electric field. This is emphasised even further by the use of nearest neighbour dipole coupling only. It also neglects the effects of radiative damping through use of the QS polarisability. Here we outline the limitations of making these simplifying assumptions.

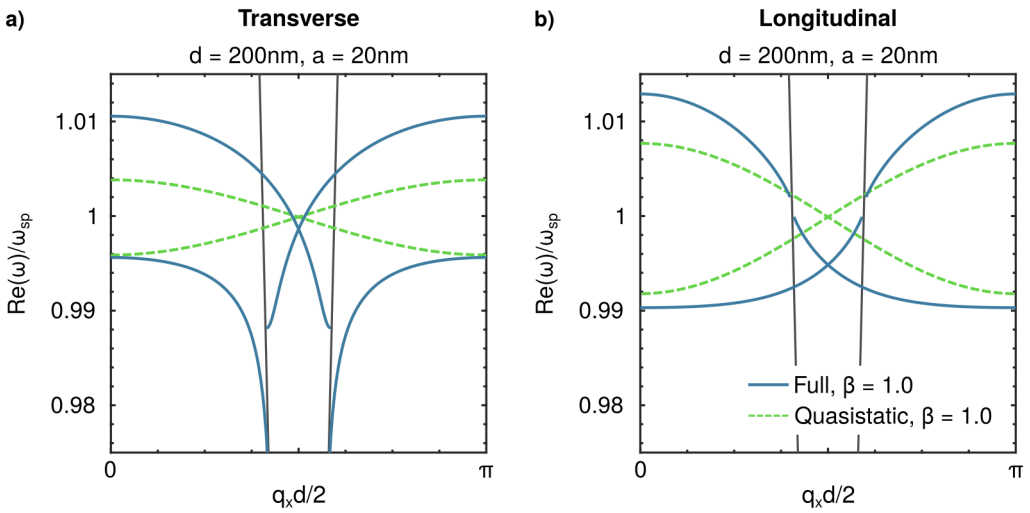

Figure 2.8: The full dipolar (blue solid line) and quasistatic (green dotted line) dispersions for the equispaced chain, $\beta = 1$, for the a) transverse and b) longitudinal polarisations, over the light lines (grey lines), adapted from [1].

In subsection 2.2.1 we saw that radiative damping has a significant effect on the size of the resonance of a particle, and is necessary to satisfy the optical theorem. Depolarisation also redshifts this peak. Consequently this limits the possible size of particles accurately described by the polarisability to below 10 nm radius.

The above study was not the first to examine a chain of metallic nanoparticles. Equispaced chains, corresponding to $\beta = 1$ in our description, have been examined for some time for their ability to act as surface plasmon waveguides [158], for uses in shaping the extinction linewidth of the surface plasmonic resonance [3, 159], and for applications in lasing [5].

Calculations of these equispaced chains have shown that the dispersion relation of chains with gold or silver particles separated by around 75 nm or more ($d \geqslant 150$ nm) are not well represented by the QS approximation, especially for the transverse polarisation. The earliest calculations used the finite chain to approximate an infinite band structure [160], and then various similar methods were utilised to approximate or evaluate the infinite sums of Green's functions [161–164]. Similar results have also been found using an open quantum system approach [143].

The most relevant method of evaluating the infinite Green's function sums for this work is the use of polylogarithmic special functions presented by Citrin [163] and also utilised by Koenderink and Polman [164]. This will be elaborated upon in the next section, where the basic idea of this method is expanded upon to treat the staggered chain where $\beta \neq 1$.

Figure 2.8 demonstrates the difference between the QS and full dipolar treatments for an equispaced chain of gold nanoparticles with Drude parameters $\epsilon_\infty = 9.1$, $\omega_P = 1.38 \times 10^{16}$ rad/s and $1/\tau = 1.08 \times 10^{14}$ rad/s [165], embedded in glass, $\epsilon_B = 2.25$. The centre-to-centre particle spacing is 100 nm, corresponding to $d = 200$ nm, and the particle radius is $a = 20$ nm.

The figure shows the real parts of the QS (green dashed) and full dipolar (blue solid) band structures for the (a) transverse and (b) longitudinal polarisations, normalised to the QS surface plasmon resonance frequency $\omega_{sp} = 3.74 \times 10^{15}$ rad/s.

Light lines, where $kd \pm q_x d = 0 \mod 2\pi$ are grey. As described by Koenderink and Polman, retardation leads to polariton-like splitting at the light lines for the transverse polarisation which are absent from the QS green dashed dispersion. In the longitudinal case there is a discontinuity in the full dispersion at the light lines. Another change in the full dipolar case is that the dispersion is not symmetric around ω_{sp}, which will be investigated in more detail in the later chapters. The particle spacing is on the same order as $\lambda_{sp} = 504\,\text{nm}$ so it is unsurprising that the QS approximation is not valid in this case, as demonstrated by the bands in the figure.

As we have seen, plasmonic systems like gold or silver tend to have surface plasmon resonances with wavelengths on the order of 100s of nanometers. Experimental techniques for fabricating arrays of metallic nanoparticles, like lithography and etching, are typically only capable of particle sizes and interparticle spacing that is too large to obey the QS condition for wavelengths of interest [166–168]. This leads us to the conclusion that, in order to make predictions about the topological properties of experimentally accessible systems, we require a full dipolar description of the topological plasmonic chain.

Of course, one might ask if we should expect any topological properties at all. Though Ling *et al.*'s model was primarily quasistatic, they also performed a full-wave simulation using Lumerical FDTD to calculate an emission rate of the topological and trivial phases of the chain [96]. This indicated the presence of a possible edge mode in the topological phase of the chain, although no band structures for the full system were calculated. This suggests that, despite the above issues with the plasmonic chain as a direct SSH model analogue, there is potential in exploring topological properties by way of a more complete band structure calculation.

3 TOPOLOGICAL PROPERTIES OF THE PLASMONIC CHAIN

In this chapter we provide a treatment for the staggered chain of metallic nanoparticles which takes the properties of light into account. Doing so allows for the length scales of the chain to be raised to experimentally accessible levels, and unveils some surprising results about the transverse polarisation of the chain.

In order to model the chain we build upon the coupled dipole equations (CDEs) to construct an effective Hamiltonian. As with the study of the SSH model in section 2.1, we first consider properties of the bulk and then move on to the finite system. We examine the effect of long range retarded dipole-dipole interactions on symmetry properties compared to the QS model, and present band structures and studies of the Zak phase. We find topologically protected edge modes in the case of longitudinal polarisation in the retarded finite chain, and study the effect of disorder on these modes. Finally we include calculations of the extinction cross section of the chain for incident plane waves.

Most of the material in this chapter, excluding section 3.5, is published in a 2017 ACS Photonics paper and its supporting material [1], for which the author of this thesis was first author. Some changes have been made to remedy the fact that the paper was written before some understanding of non-Hermitian TIs and bulk-edge correspondence emerged. Some aspects that are missing will be elaborated in later chapters. Further permissions related to the material excerpted should be directed to the American Chemical Society.

3.1 MODELLING THE PLASMONIC CHAIN

First, we establish the model we use throughout the chapter. Our plasmonic analogue of the Su-Schrieffer-Heeger (SSH) model is a chain of metallic nanoparticles with alternating spacing, depicted in figure 3.1. Particles have radius a and unit cells length d, with the spacing between the A and B sublattices given by $t = \beta d/2$, where β acts as a tuning parameter. Throughout this thesis, we choose the spacing of the particles to be large enough compared to the radius of the spheres ($t,\ d - t \geqslant 3a$) that the nanospheres can be treated as dipoles [150] with dipole moments $\mathbf{p}_n$. Therefore, the system is described by the coupled dipole equations,

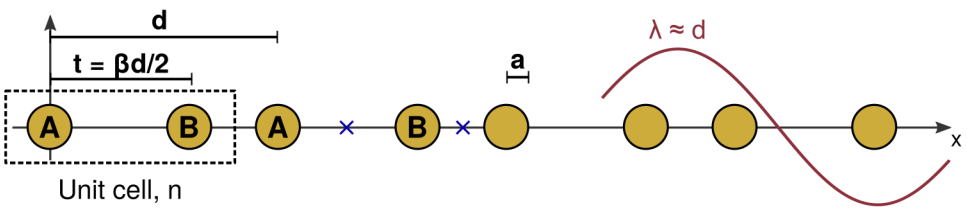

Figure 3.1: Diagram of the plasmonic chain featuring radiative effects, adapted from [1]

$$\frac{1}{\alpha(\omega)}\mathbf{p}_n = \frac{k^2}{\epsilon_0}\sum_{j\neq n} G(\mathbf{r}_{nj},\omega)\mathbf{p}_j, \tag{3.1}$$

where $k = \sqrt{\epsilon_B}\omega/c = \sqrt{k_x^2+k_y^2+k_z^2}$ is the magnitude of the wavevector, and $G(\mathbf{r}_{nj},\omega)$ is the free space 3×3 Green's dyadic. Here the notation of the Green's dyadic's parameters have been modified slightly to capture the dependence on the spatial separation between two positions, $\mathbf{r}_{nj} = \mathbf{r}_n - \mathbf{r}_j$, and the frequency ω.

As discussed in subsection 2.2.1, the properties of each nanoparticle are captured by the polarisability $\alpha(\omega)$. In this chapter we make use of the radiative correction,

$$\alpha_R(\omega) = \frac{\alpha_{QS}(\omega)}{1 - i\frac{k^3}{6\pi\epsilon_0}\alpha_{QS}(\omega)}, \tag{3.2}$$

with quasistatic polarisability given by

$$\alpha_{QS}(\omega) = 4\pi a^3\epsilon_0\frac{\epsilon(\omega)-\epsilon_B}{\epsilon(\omega)+2\epsilon_B}. \tag{3.3}$$

Here $\epsilon(\omega)$ is the dielectric function of the metal, ϵ_0 the permittivity of free space and ϵ_B the relative background permittivity. In this chapter we utilise the radiative correction rather than the MLWA in order to simplify some numerical calculations. The radiative correction is the simplest polarisability available which obeys the optical theorem, and we have seen that, for larger particles, the main difference between the radiative correction and MLWA is a redshift of the resonance peak which should not change any qualitative conclusions in this chapter.

Here we consider gold nanospheres using the Drude model,

$$\epsilon(\omega) = \epsilon_\infty - \frac{\omega_P^2}{\omega^2 + i\omega/\tau}, \tag{3.4}$$

with $\epsilon_\infty = 9.1$, $\omega_P = 1.38\times 10^{16}$ rad/s and $1/\tau = 1.08\times 10^{14}$ rad/s [165], embedded in a material like glass, with dielectric constant $\epsilon_B = 2.25$. This is the same set of parameters used for figure 2.8. We deliberately exclude interband transitions to make the effects of retardation more clear in this study, although we would not expect this to affect the existence of modes [9, 96]. We also do not include a substrate, which could modify the dispersion relation of the plasmons [169, 170], but is avoidable by making use of a transparent substrate and index matching with the surrounding material [171].

The chain is confined to the x-axis, which causes the Green's dyadic to become diagonal. Therefore, the longitudinal (x) and transverse (y, z) parts of equation 3.1 decouple,

$$\frac{1}{\alpha(\omega)}p_{\nu,n} = \frac{k^2}{\epsilon_0}\sum_{j\neq n} G^{\nu\nu}(r_{nj},\omega)p_{\nu,j}, \tag{3.5}$$

where $\nu = x, y, z$ labels the orientation of the dipoles. The elements of the Green's dyadic which couple dipoles of the same orientation are

$$G^{xx}(r_{nj},\omega) = \frac{2e^{ikr_{nj}}}{4\pi k^2 r_{nj}^3}\left[1 - ikr_{nj}\right], \tag{3.6}$$

$$G^{yy,zz}(r_{nj},\omega) = \frac{-e^{ikr_{nj}}}{4\pi k^2 r_{nj}^3}\left[1 - ikr_{nj} - k^2 r_{nj}^2\right], \tag{3.7}$$

with ω dependence contained within k.

Next, we relabel the particles so that $\mathbf{p}_n^A$ and $\mathbf{p}_n^B$ are the dipole moments of particle A and B in unit cell n respectively, as in figure 3.1(a). This leads to the following equations,

$$\frac{p_{\nu,n}^A}{\alpha(\omega)} = \frac{k^2}{\epsilon_0}\sum_{j\neq n} G^{\nu\nu}((n-j)d,\omega)p_{\nu,j}^A + \frac{k^2}{\epsilon_0}\sum_j G^{\nu\nu}((n-j)d+t,\omega)p_{\nu,j}^B, \tag{3.8}$$

$$\frac{p_{\nu,n}^B}{\alpha(\omega)} = \frac{k^2}{\epsilon_0}\sum_j G^{\nu\nu}((n-j)d-t,\omega)p_{\nu,j}^A + \frac{k^2}{\epsilon_0}\sum_{j\neq n} G^{\nu\nu}((n-j)d,\omega)p_{\nu,j}^B. \tag{3.9}$$

This set of equations will be the basic structure upon which the results of this chapter will be built.

3.2 PROPERTIES OF THE BULK

In order to examine the bulk of the system, we consider an infinite chain and use Bloch's theorem. The dipole moment for each particle in a given unit cell n is the product of the unit cell dipole moment when $n = 0$, p_ν^A or p_ν^B, and a phase factor $e^{iq_x nd}$,

$$p_{\nu,n}^A = p_\nu^A e^{iq_x nd}, \qquad p_{\nu,n}^B = p_\nu^B e^{iq_x nd}. \tag{3.10}$$

Applying this to equations 3.8 and 3.9 leads to an eigenvalue problem,

$$\mathcal{G}_\nu(q_x,\omega)\begin{pmatrix} p_\nu^A \\ p_\nu^B \end{pmatrix} = \frac{1}{\alpha(\omega)}\begin{pmatrix} p_\nu^A \\ p_\nu^B \end{pmatrix}, \tag{3.11}$$

where $\mathcal{G}_\nu(q_x,\omega)$ acts as an ω-dependent non-Hermitian Bloch Hamiltonian which is, in matrix form,

$$\mathcal{G}_\nu(q_x,\omega) = \begin{pmatrix} \sum'_{n\in\mathbb{Z}} G^{\nu\nu}(nd,\omega)e^{iq_x nd} & \sum_{n\in\mathbb{Z}} G^{\nu\nu}(nd+t,\omega)e^{iq_x nd} \\ \sum_{n\in\mathbb{Z}} G^{\nu\nu}(nd-t,\omega)e^{iq_x nd} & \sum'_{n\in\mathbb{Z}} G^{\nu\nu}(nd,\omega)e^{iq_x nd} \end{pmatrix}, \tag{3.12}$$

where the primed sum notation indicates that the sum does not include the $n = 0$ term. The eigenvalues of $\mathcal{G}_\nu$ are $\mathcal{E} = 1/\alpha(\omega)$, but the band structure is given by ω. Topological properties of the system are associated with the eigenvectors $\mathbf{p}_\nu = (p_\nu^A, p_\nu^B)^T$.

It was shown in the previous chapter that the QS nearest neighbour approximation has strict sublattice symmetry (SLS), because there is no hopping from sites A to A or from B to B. This can be expressed by $\sigma_z H \sigma_z = -H$, as discussed in some detail in subsection 1.2.3 and section 1.4. In this treatment SLS is broken by the presence of long range hopping. The exact manner in which the symmetry is broken is elaborated upon later in this chapter. We might therefore expect the system to be topologically trivial, however the results of this chapter will show that the retarded plasmonic chain has a wealth of topological properties. A clearer understanding of why and to what extent will be developed in chapter 4.

Another symmetry worth noting for this system is inversion symmetry in the x-direction, mathematically expressed by $\sigma_x \mathcal{G}_\nu(q_x)\sigma_x = \mathcal{G}_\nu(-q_x)$. Inversion centres are marked by blue crosses in figure 3.1(a). This symmetry guarantees that the band structure will be symmetric in q_x.

Calculating the band structure is a matter of fixing real q_x and finding corresponding complex ω numerically, to solve

$$\det\left(\mathcal{G}_\nu - \frac{1}{\alpha(\omega)}\mathrm{I}\right) = 0. \tag{3.13}$$

Physically, the real part of the frequency is the measured frequency and the imaginary part dictates the rate of decay of the given mode. We discuss this further in subsection 3.4.1.

Solving for the band structure is complicated by the fact that the elements of the Hamiltonian $\mathcal{G}_\nu$ are infinite, slowly converging sums. We address this using a special function known as the Lerch transcendent.

3.2.1 The Lerch Transcendent

As discussed in subsection 2.3.2, Citrin [163] and then Koenderink and Polman [164] used polylogarithms to calculate the infinite sums in the case of equally spaced chains. The on diagonal terms of equation 3.12 represent hopping between the same sublattice, where particles are equally spaced by a distance nd. We therefore use polylogarithms to evaluate these sums. Polylogarithms can be defined by the infinite sum

$$\mathrm{Li}_s(z) := \sum_{n=1}^{\infty} \frac{z^n}{n^s}. \tag{3.14}$$

These have the advantage of being implemented as standard in several scientific packages. The polylog forms for the on-diagonal terms are

$$\begin{aligned}\sum_{n\in\mathbb{Z}}{}' G^{xx}(nd)e^{iq_x nd} = \frac{2}{4\pi\epsilon_0 d^3}\Big\{&\mathrm{Li}_3(e^{i(k-q_x)d}) + \mathrm{Li}_3(e^{i(k+q_x)d}) \\ &- ikd\left[\mathrm{Li}_2(e^{i(k-q_x)d}) + \mathrm{Li}_2(e^{i(k+q_x)d})\right]\Big\}\end{aligned} \tag{3.15}$$

and

$$\sum_{n\in\mathbb{Z}}{}' G^{yy,zz}(nd)e^{iq_x nd} = -\frac{1}{4\pi\epsilon_0 d^3}\Big\{\mathrm{Li}_3(e^{i(k-q_x)d}) + \mathrm{Li}_3(e^{i(k+q_x)d}) - ikd\left[\mathrm{Li}_2(e^{i(k-q_x)d}) + \mathrm{Li}_2(e^{i(k+q_x)d})\right] - k^2d^2\left[\mathrm{Li}_1(e^{i(k-q_x)d}) + \mathrm{Li}_1(e^{i(k+q_x)d})\right]\Big\}. \tag{3.16}$$

The off diagonal terms relate to A to B and B to A hopping, which corresponds to spacing $nd \pm t$. These no longer fit the form of a polylogarithm. This author's insight was to apply a more general special function, the Lerch transcendent, which can be defined as

$$\Phi(z, s, \nu) := \sum_{n=0}^{\infty} \frac{z^n}{(n+\nu)^s}. \tag{3.17}$$

For our numerical calculations, we make use of the fact that the Lerch transcendent can be expressed as an integral,

$$\Phi(z, s, \nu) = \frac{1}{\Gamma(s)} \int_0^{\infty} \frac{t^{s-1}e^{-\nu t}}{1 - ze^{-t}} dt, \tag{3.18}$$

where $\mathrm{Re}(\nu) > 0$, and either $|z| \leqslant 1, z \neq 1, \mathrm{Re}(s) > 0$ or $z = 1, \mathrm{Re}(s) > 1$ [172]. This imposes the restriction that it is not possible to calculate the Lerch transcendent on the light lines, where $kd \pm q_x d = 0$ modulo 2π, for the transverse case, as can be seen from the following equations.

The off-diagonal elements, in terms of the Lerch transcendent, are

$$\sum_{n\in\mathbb{Z}} G^{xx}(nd \pm t)e^{iq_x nd} = \frac{2}{4\pi\epsilon_0 d^3}\Big\{e^{ikt}\Phi\left(e^{i(k\pm q_x)d}, 3, \frac{t}{d}\right) + e^{-ikt}e^{i(k\mp q_x)d}\Phi\left(e^{i(k\mp q_x)d}, 3, 1-\frac{t}{d}\right) - ikd\Big[e^{ikt}\Phi\left(e^{i(k\pm q_x)d}, 2, \frac{t}{d}\right) + e^{-ikt}e^{i(k\mp q_x)d}\Phi\left(e^{i(k\mp q_x)d}, 2, 1-\frac{t}{d}\right)\Big]\Big\}, \tag{3.19}$$

and

$$\begin{aligned}\sum_{n\in\mathbb{Z}} G^{yy,zz}(nd\pm t)e^{iq_x nd} = -\frac{1}{4\pi\epsilon_0 d^3}\Bigg\{ & e^{ikt}\Phi\left(e^{i(k\pm q_x)d}, 3, \frac{t}{d}\right) \\ & + e^{-ikt}e^{i(k\mp q_x)d}\Phi\left(e^{i(k\mp q_x)d}, 3, 1-\frac{t}{d}\right) \\ & - ikd\Bigg[e^{ikt}\Phi\left(e^{i(k\pm q_x)d}, 2, \frac{t}{d}\right) \\ & + e^{-ikt}e^{i(k\mp q_x)d}\Phi\left(e^{i(k\mp q_x)d}, 2, 1-\frac{t}{d}\right)\Bigg] \\ & - k^2d^2\Bigg[e^{ikt}\Phi\left(e^{i(k\pm q_x)d}, 1, \frac{t}{d}\right) \\ & + e^{-ikt}e^{i(k\mp q_x)d}\Phi\left(e^{i(k\mp q_x)d}, 1, 1-\frac{t}{d}\right)\Bigg]\Bigg\}. \end{aligned} \tag{3.20}$$

Before performing any numerics we make a simple analytical observation. If we substitute $q_x = \pm\pi/d$ and $t = d/2$ we see that

$$\sum_{n\in\mathbb{Z}} G^{vv}(nd \pm d/2)e^{in\pi/2} = 0. \tag{3.21}$$

For these values, the off diagonal terms in the Hamiltonian $\mathcal{G}$ are zero. The Hamiltonian is therefore proportional to the identity matrix, so that the eigenvalues are degenerate and the gap closes. This shows that when $\beta = 1$, the bands cross at the edge of the Brillouin zone (BZ), at $q_x d/2 = \pi/2$. This is also true in the QS limit, where it signified a topological phase transition. We will show that a phase transition also occurs at this point in the full dipolar treatment.

3.2.2 Bulk band structures

We now present numerically calculated band structures for various choices of chain parameters d and a in figure 3.2, displaying only the real part of ω. Complex bands are shown later, in subsection 3.4.1. Blue dashed lines show the $\beta = 1$ case, and red solid lines show the $\beta = 0.9$ (identical to $\beta = 1.1$) case. For $\beta \neq 1$, a *complex valued* gap opens at the edge of the BZ, which increases in magnitude with increasing $|\beta - 1|$. We will soon see that this gap corresponds to a point gap, as discussed in section 1.4, according to the definition of Kawabata *et al.* [105].

For small chain geometry, $d = 50$ nm, $a = 5$ nm, in figure 3.2(a), the band structure is well approximated by the QS model (yellow dotted line), which makes a reasonable prediction of the band gap, but fails to predict the small deviations of the band structure at the light line in the transverse case. In addition, some asymmetry in $\mathrm{Re}(\omega)$ exists due to the breaking of SLS.

Figures 3.2(b,c) demonstrate band structures with larger particles and spacing, with $d \sim \lambda_{sp}$, well away from the QS limit. The usual polariton-like splitting and $\mathrm{Re}(\omega)$ asymmetry are present, as well as discontinuities at the light line, as in the upper band for (b) longitudinal. The QS approximation, not shown for clarity, is poor here and completely fails to predict that a gap in $\mathrm{Re}(\omega)$ does not always open, such as in (b) transverse and (c) longitudinal. It is important to note that, in these cases,

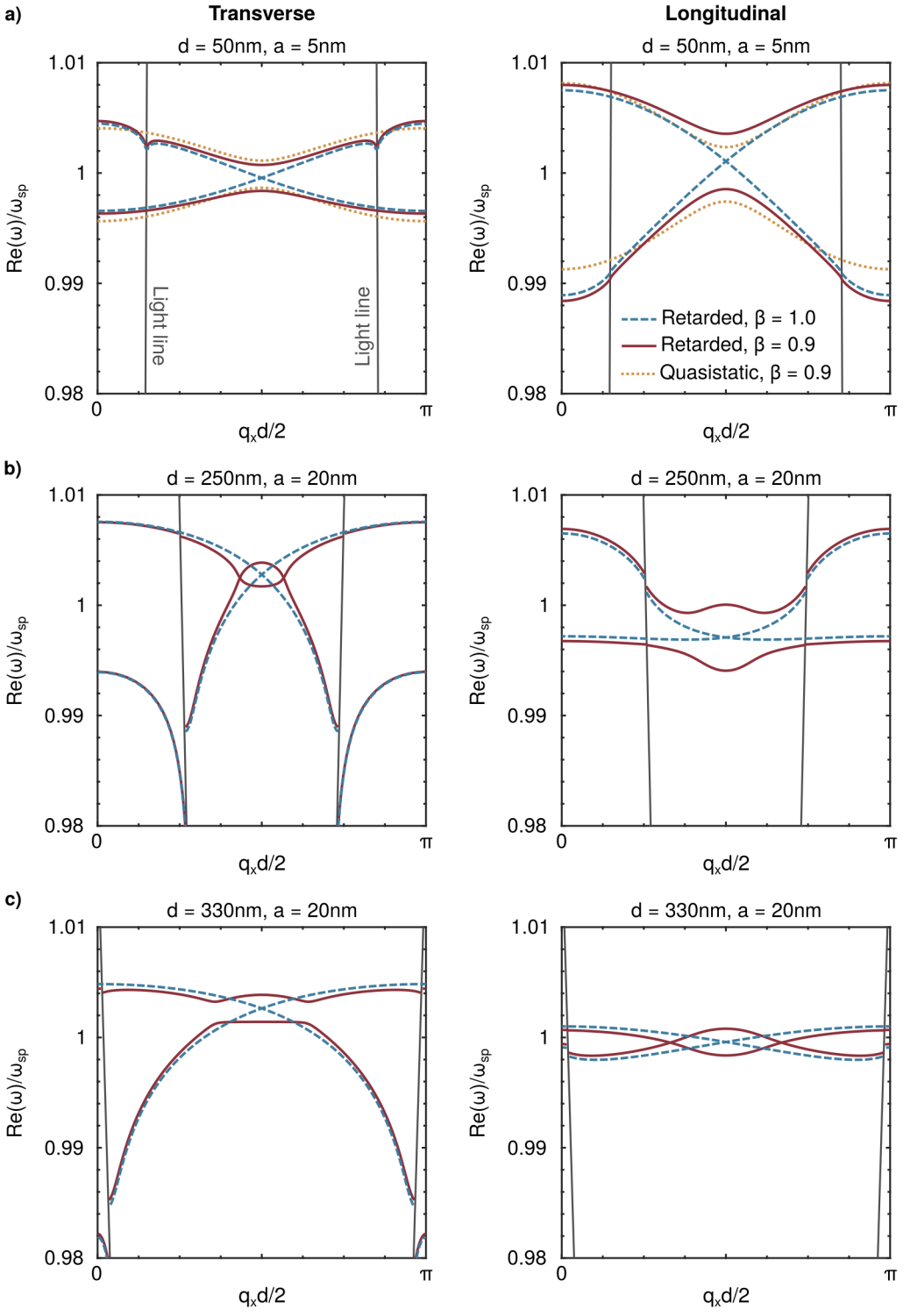

Figure 3.2: Band structures for the topological plasmonic chain, for various choices of geometric parameters d and a, with $\beta = 0.9$ or 1.1. (a) Comparison of QS and retarded band structures near the QS regime. (b),(c) show band structures further away from the QS regime and *do not feature the yellow QS bands*, which are similar to those shown in (a).

there still exists a gap in $\mathrm{Im}(\omega)$, such that there is no band crossing and associated topological phase transition. This is discussed in more detail in subsection 3.4.1. This gap allows us to ask if these cases are topological or trivial, but before doing so we examine the bulk symmetry properties in more detail.

3.2.3 Sublattice symmetry breaking

As we have seen for the SSH model, in section 2.1, it is possible to write $\mathcal{G}$ in terms of the Pauli matrices $\{\sigma_i\}$,

$$\mathcal{G}(q_x) = g_0(q_x)I + \mathbf{g}(q_x)\cdot\boldsymbol{\sigma}, \tag{3.22}$$

where $\boldsymbol{\sigma}$ is the vector of Pauli spin matrices. This is true for any two band Hamiltonian. For this system in particular,

$$\begin{aligned}
g_0(q_x) &= \sum_{n\neq 0} G(nd)e^{iq_x nd},\\
g_x(q_x) &= \left[\sum_n G(nd+t)e^{iq_x nd} + \sum_n G(nd-t)e^{iq_x nd}\right],\\
g_y(q_x) &= i\left[\sum_n G(nd+t)e^{iq_x nd} - \sum_n G(nd-t)e^{iq_x nd}\right],\\
g_z(q_x) &= 0.
\end{aligned} \tag{3.23}$$

SLS exists when there are no interactions between sites A to A or B to B, and we have seen it can be expressed in the form $\sigma_z H\sigma_z = -H$. This is the case when $g_0 = 0 = g_z$ in equation 3.22. Although this model breaks SLS due to long range dipole-dipole interactions, there is no σ_z contribution to the matrix due to $g_z(q_x) = 0$. This means that the difference between the retarded plasmonic system and an SLS system is only the identity term $g_0 \neq 0$. Therefore, the system has the same eigenvectors as an SLS system with Bloch Hamiltonian $\mathcal{H} = \mathcal{G} - g_0 I$,

$$\begin{aligned}
\mathcal{G}\mathbf{p} &= \frac{1}{\alpha}\mathbf{p},\\
(\mathcal{G} - g_0 I)\,\mathbf{p} &= \left(\frac{1}{\alpha} - g_0\right)\mathbf{p}.
\end{aligned} \tag{3.24}$$

This equivalence between eigenvectors allows us to apply Zak phase results for SLS systems directly to ours.

We also have a pseudo-SLS equation for $\mathcal{G}$ from the original SLS equation, given by $\sigma_z(\mathcal{G} - g_0 I)\sigma_z = -(\mathcal{G} - g_0 I)$. This leads us to conclude that eigenvalues will be not plus-minus pairs around $1/\alpha = 0$. Instead,

$$\begin{aligned}
(\mathcal{G} - g_0 I)\,\sigma_z\mathbf{p} &= -\sigma_z\,(\mathcal{G} - g_0 I)\,\mathbf{p}\\
&= -\left(\frac{1}{\alpha} - g_0\right)\sigma_z\mathbf{p},
\end{aligned} \tag{3.25}$$

so that, much like the SLS case, every eigenmode $\mathbf{p}$ has a counterpart $\sigma_z\mathbf{p}$, with eigenvalues related by

$$\begin{aligned} \mathcal{G}\mathbf{p} &= \frac{1}{\alpha}\mathbf{p}, \\ \mathcal{G}\sigma_z\mathbf{p} &= \left(2g_0 - \frac{1}{\alpha}\right)\sigma_z\mathbf{p}. \end{aligned} \tag{3.26}$$

These equations relate the upper and lower bands of $\mathcal{G}$, although an additional non-trivial mapping is required from the eigenvalues to ω. Notably, $\mathcal{G}$ also has ω dependence, and so the eigenvalues aren't perfectly symmetric around g_0.

In conclusion, the bulk topological properties of the system are identical to a corresponding SLS system because the eigenvectors of the Hamiltonian are the same. Therefore, the Zak phase is the same. In the original paper in which these results were published [1] we referred to this type of symmetry breaking as 'trivial', and used 'chiral' rather than 'sublattice' throughout the work. The word 'trivial' was used because, as it has no effect on the Zak phase, we expected it to have no effect on the topological properties of the system at all. However, we will see later in the chapter that this is not true in some cases due to the issue of bulk-edge correspondence (BEC). The use of 'sublattice' here rather than 'chiral' is in order to align with the convention used by Kawabata *et al.* [105].

It is possible to break sublattice symmetry without maintaining the Zak phase by adding a term in σ_z to the Bloch Hamiltonian, which can be achieved by changing the polarisability for the two different sublattices. For example, one could change the relative sizes of A and B particles, or make the A and B particles different materials.

3.2.4 The Zak phase

The next step is to apply these results to calculate the Zak phase for this system. In section 2.1 we saw an expression for the Zak phase of the SSH model. For a Hermitian system like the SSH model, this time in dipolar notation, the Zak phase is given by

$$\gamma_H = i\int_{-\pi/d}^{\pi/d} \mathbf{p}^\dagger \frac{\partial \mathbf{p}}{\partial q_x} dq_x. \tag{3.27}$$

However, the Hamiltonian $\mathcal{G}_v$ is non-Hermitian, so we must be more careful. The generalisation of the Berry phase for non-Hermitian systems [173], written in 1d, is

$$\gamma = i\int_{-\pi/d}^{\pi/d} \mathbf{p}_L^\dagger \frac{\partial \mathbf{p}_R}{\partial q_x} dq_x, \tag{3.28}$$

where $\mathbf{p}_R$ and $\mathbf{p}_L$ are normalized biorthogonal right and left eigenvectors, solving equation 3.11 and its Hermitian conjugate respectively. It has been shown that SLS quantises this non-Hermitian Zak phase [132], and we showed in the previous section that this applies for the current system too. In fact, the aforementioned inversion sym-

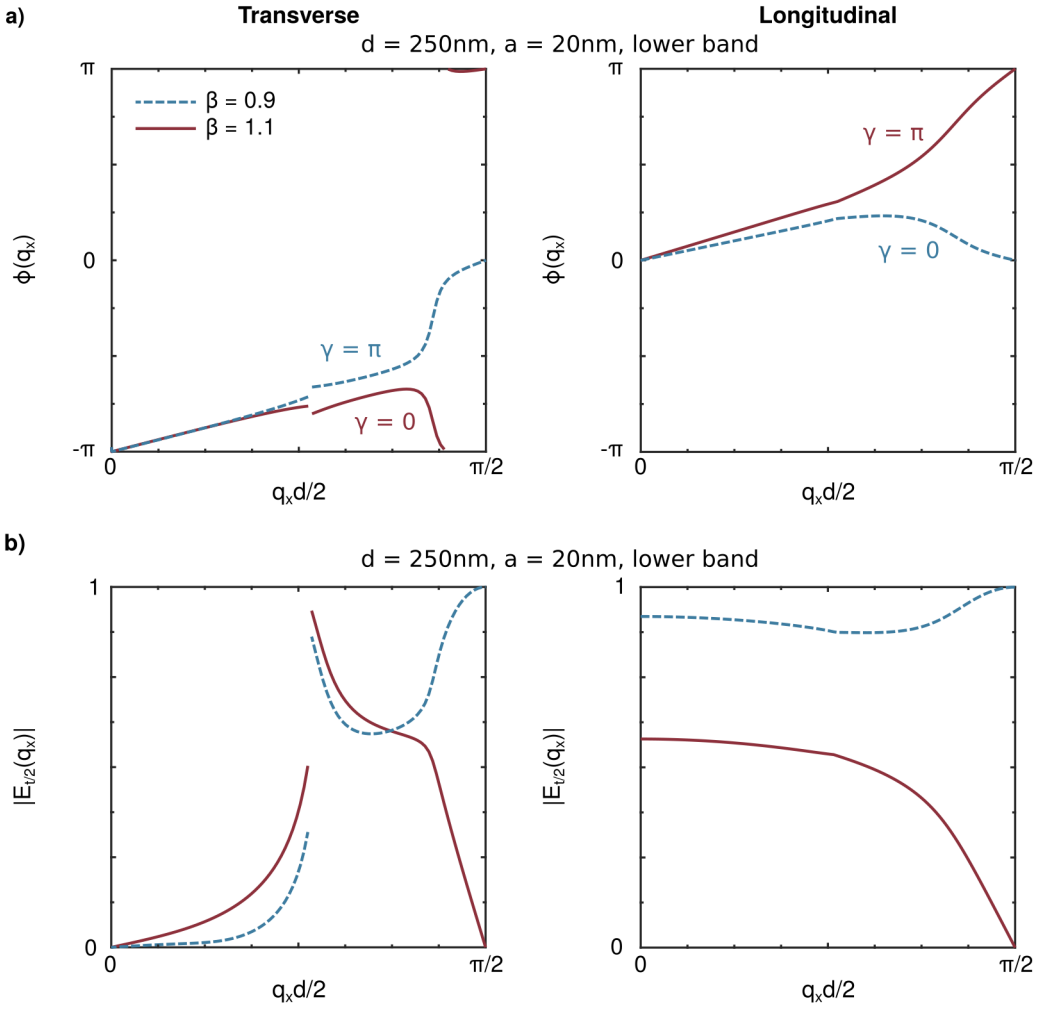

Figure 3.3: Representations of the calculation of the Zak phase γ for the lower band from figure 3.2(b). (a) The change of ϕ across the half the BZ, modulo 2π. Since $\phi(-q_x) = -\phi(q_x)$, this is enough to see the calculation of the Zak phase. (b) The normalized electric field at the $x = t/2$ inversion centre. The upper band has the same topological number as the lower band in all examined cases.

metry of the system leads to quantisation of the Hermitian Zak phase as well [174], so that both calculations have the same familiar result,

$$\gamma = \frac{\phi(\pi/d) - \phi(-\pi/d)}{2} \mod 2\pi, \tag{3.29}$$

where ϕ is the relative phase difference between p^A and p^B. It follows that for $\beta \neq 1$, γ is either 0 or π modulo 2π. As in section 2.1, the Zak phase $\gamma = \pi$ leads us to expect topologically protected edge modes when the system features BEC.

As a brief aside, topological systems with SLS but no inversion symmetry can exist [132], so the identical Hermitian and non-Hermitian Zak phase is not seen in all sublattice symmetric systems. In addition, inversion symmetry quantises the Zak phase but does not lead to topological protection without SLS, as will be discussed in chapter 4.

Figure 3.3(a) shows $\phi(q_x)$ changing across half the BZ for the lower bands of figure 3.2(b). We only need half the BZ because inversion symmetry gives us the other

half, with $\phi(-q_x) = -\phi(q_x)$. The vertical axis is periodic at π and $-\pi$ because ϕ is a phase, but this periodic value could be shifted, so the important information is in whether ϕ completes a loop across the BZ or does not. This is represented in the connection between the Zak phase and the winding number, explored in section 2.1.

We examine β either side of the topological phase transition at $\beta = 1$, with blue dashed lines representing ϕ for $\beta = 0.9$ and solid red lines representing ϕ for $\beta = 1.1$. The longitudinal case has the same property as the SSH model and QS approximation, that $\gamma = \pi$ when $\beta > 1$ and $\gamma = 0$ when $\beta < 1$. Surprisingly, the transverse case is in the opposite topological phase to the longitudinal case for the same choice of unit cell when it has the same β. The $\beta = 0.9$ case winds around zero and gives a Zak phase of $\gamma = \pi$, while the $\beta = 1.1$ case does not and has a Zak phase of $\gamma = 0$.

Of the example band structures given in figure 3.2, all bands have the same topological properties as the SSH model and (b) longitudinal, except (b) transverse. This implies that topological phase transitions occur for the transverse polarized modes between (a) and (b), and again between (b) and (c).

We explore these surprising phase transitions shortly, but first confirm these results by considering an alternative Zak phase calculation. M. Xiao *et al.* showed that, in photonic systems, the Zak phase is also given by the behaviour of the electric field at the inversion centres $x = t/2, (d + t)/2$ of the chain, at the centre ($q_x = 0$) and edge ($q_x = \pi/d$) of the BZ [81]. Considering the inversion centre at $x = t/2$, if $|E_{t/2}(q_x = 0)|$ and $|E_{t/2}(q_x = \pi/d)|$ are both either zero or non-zero, we have $\gamma = 0$. If $|E_{t/2}(q_x = 0)|$ and $|E_{t/2}(q_x = \pi/d)|$ are opposite, so that one is zero while the other is non-zero, the Zak phase is given by $\gamma = \pi$. The normalized magnitude of the electric field at $x = t/2$ is shown across the BZ in figure 3.3(b), which agrees with the calculations of figure 3.3(a). If we take the opposite inversion centre the Zak phases are switched, as we have effectively picked a different gauge. This method of determining the topological nature of the system relies on Zak's results [123] originally for Hermitian systems, but inversion symmetry assures that any results for the Hermitian Zak phase is identical here to the non-Hermitian Zak phase.

Through the treatment of retardation, we have found an interesting phase transition for transverse-polarised modes that was overlooked in previous studies of the topological plasmonic chain. We examine one of these phase transitions in figure 3.4, where the Zak phases for chains with fixed radius $a = 5$ nm and $\beta = 0.9, 1.1$ are plotted with changing unit cell spacing d. The Zak phase predicted by the QS model is shown by the horizontal dark grey line. Results obtained for transverse modes are given by red circles, which agree with the QS prediction for chain periods near the QS limit, then undergo a phase transition somewhere between $d = 90$ and 100 nm in the grey region. Consequently, it enters the phase opposite to the QS prediction in the yellow region.

Topological phase changes occur when the product of the off diagonal elements of the matrix $\mathcal{G}_v(q_x, \omega)$ in equation 3.12 is zero, causing the gap to close. Changing the radius of the particles a only impacts the eigenvalue $1/\alpha(\omega)$, which could change where the gap closes in d but not the existence of the gap closure. In fact, the zeros can only happen for the transverse case due to the third, long range, term in the Green's function in equation 3.7. We show this by considering the Zak phase for a system which does not include this long range term, given by the blue crosses in figure 3.4. This case is equivalent to the longitudinal case, which has the same Green's function apart from a factor of -2 which makes no difference to the closing

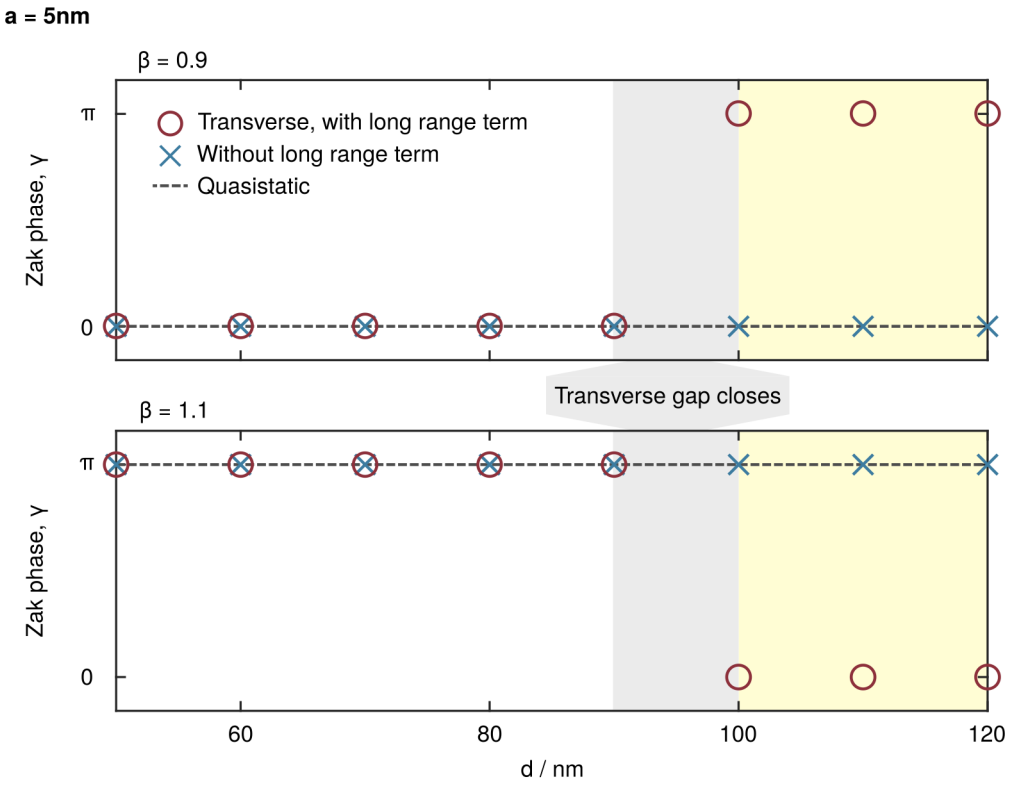

Figure 3.4: Retardation-induced Zak phase changes with particle spacing d, where the ratio β is fixed. The transverse gap closes somewhere in the grey region and a phase transition occurs that is not predicted by the QS nearest neighbour approach. Red circles are the calculation with the full transverse Green's function in equation 3.7. Blue crosses show the case where the third long range term is not included, equivalent to the longitudinal-polarised modes.

of the gap. Here no phase change occurs with changing d, as predicted by the QS model, because the missing long range term is responsible for the phase transition in the other case. Finally, we observe that the off diagonals of $\mathcal{G}_\nu(q_x, \omega)$ are transformed into each other by mapping $\beta \mapsto 2 - \beta$. Therefore, if the gap closes for β it will also close for $2 - \beta$, so phase transitions occur for β symmetric around $\beta = 1$, and are opposite due to the phase transition at $\beta = 1$.

Why does the long range term allows for phase transitions to occur? A possible explanation is linked closely to its extremely slowly decaying nature. Consider the contributions to the dipole moment for a particle at some position in the chain. The decay of the long range term is so slow that it even diverges when $z = 1$ in the Lerch transcendent, which makes it is possible for the nearest neighbour hopping term to be smaller than the sum of the remaining particles' contributions. This cannot happen for the medium or short range hopping terms. It has been shown in that, when the nearest neighbour hopping is not the largest, the system can have access to higher winding numbers with more predicted edge modes [125, 127]. In our case, it appears that the non nearest neighbour contributions are large enough to cause topological phase transitions, but not large enough to push the system to even higher winding numbers.

These transverse phase transitions are non-Hermitian effects which deserve further study. In chapter 4 we find that BEC is not preserved in this region of the transverse

polarisation, preventing the observation of edge modes corresponding to these phase transitions. We argue that the topological phase is of some interest even when not corresponding to edge modes. In chapter 5 we study these retardation-induced phase transitions in much greater detail.

3.3 FINITE CHAINS AND DISORDER

Now that we have studied the bulk properties of the chain, the next step is to consider the implications for edge modes in finite chains. Mathematically, the approach is to start with equations 3.8 and 3.9, make the sums finite from $j = 1$ to $j = N$, and construct a matrix out of the terms of the sums. Solving the eigenvalue problem for ω gives the finite modes of the system. This is the same approach as for the SSH model in subsection 2.1.2, except we look for ω instead of the actual eigenvalues $\mathcal{E}$.

In this section the main focus is on the longitudinal polarisation of the dipole moments. For this model, we struggled to find transverse edge modes, which we attributed to finite size effects because these numerical methods limit us to chains of $N \leqslant 60$ or so, and the transverse polarisation has the very slowly decaying long range term in its Green's function. However, it is now clear that this is because BEC had broken down in the parameters we searched. This phenomenon is studied in chapter 4.

Figure 3.5(a) shows the eigenvalues of a finite chain, with an example choice of parameters so that there is a gap in $\mathrm{Re}(\omega)$, for the longitudinal polarisation. The real valued gap, as defined by the bulk modes (blue), increases symmetrically away from $\beta = 1$, where there is a topological phase transition. Edge modes (yellow) appear in the gap when the Zak phase $\gamma = \pi$.

Bulk modes can be identified by their mode profiles, which are typically similar to normal modes of a chain, as in figure 3.6(b). They can therefore be ordered by assigning a mode number n, the number of times the sign of $\mathrm{Re}(p_\nu)$ changes plus 1, and a q_x given by

$$q_x \frac{d}{2} = \frac{(N-2)n+1}{N(N-1)}\pi, \tag{3.30}$$

where N is the number of particles in the chain [160], and $N = 60$ in our calculations. These (q_x, ω) pairs are plotted for an example set of parameters in 3.5(b), where the finite QS approximation (red circles) and retarded system (blue dots) are compared. Bulk modes of the finite chain approximate the Bloch band structure in both cases, and the two edge modes exist in the gap.

Figure 3.5(c) shows the dipole moments of a set of particles at the edge of a chain, with a comparison between the QS edge mode (yellow dashed) and the retarded edge mode (green solid). The QS edge mode is fully supported on only the A sublattice due to SLS, as discussed in subsection 2.1.2, while the retarded edge mode exists on both sublattices. The edge modes decay exponentially into the chain, although the retarded edge mode does so with a longer decay length. The real part of p_x has a minimum at particle 5, before increasing and then decreasing again because of the longer range, out of phase, dipole-dipole interactions, but the absolute value $|p_x|$ still decays monotonically on each sublattice into the chain as illustrated by the inset $\log|\mathbf{E}|$ field. When the gap has no real part, edge mode frequencies have an

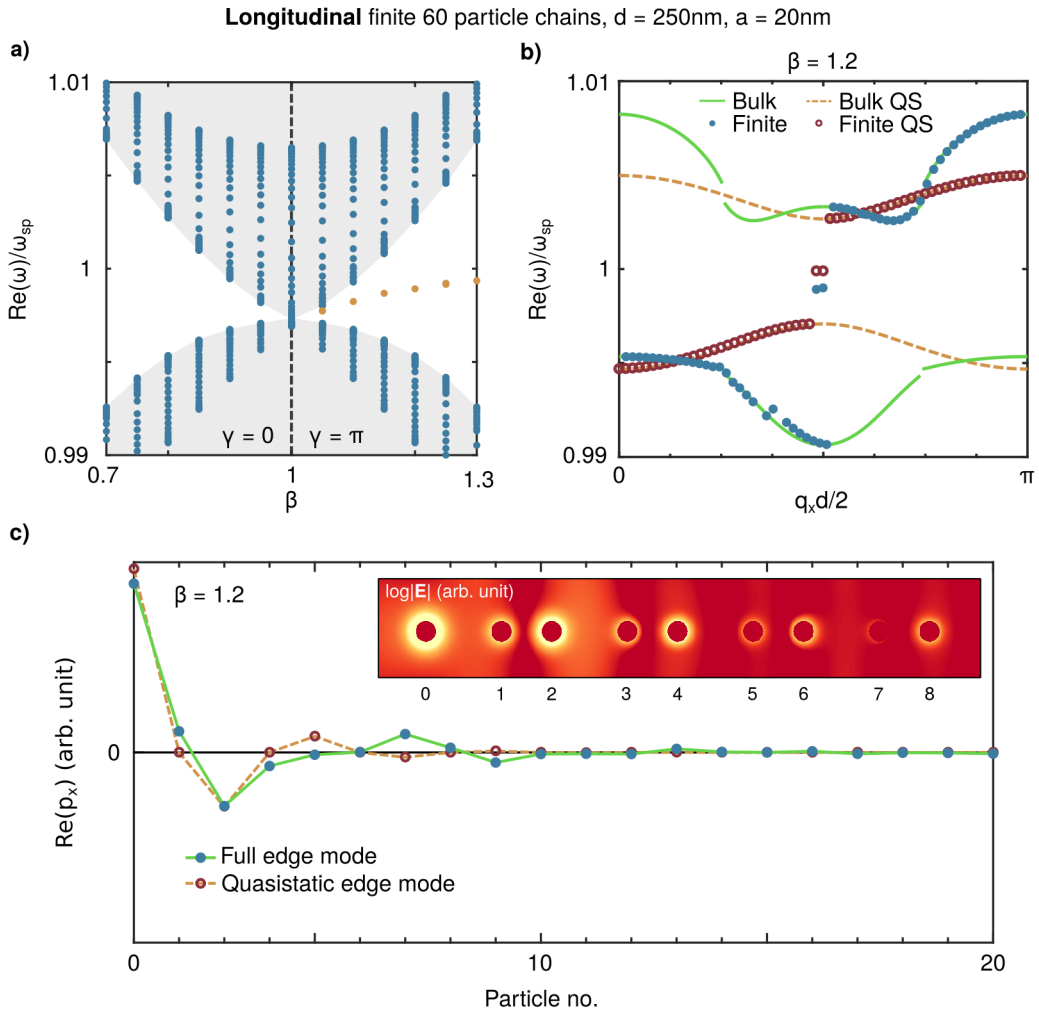

Figure 3.5: (a) Longitudinal eigenmodes of a finite 60 particle chain with varying β. As predicted by the Zak phase, edge states (yellow) exist when $\beta > 1$. (b) Comparison of the quasistatic and retarded finite chain band structure for a choice of $\beta = 1.2$, showing edge modes in the gap. (c) The real parts of the QS and retarded edge mode profiles of the leftmost end of the chain. Modes in the gap are symmetric and antisymmetric combinations of these modes profiles. Inset: $\log|\mathbf{E}|$ field outside of the particles for retarded left edge mode, excited by an evanescent plane wave perpendicular to the chain. Dark red corresponds to the weakest field, and bright yellow represents a stronger field.

imaginary part so that they still sit in the imaginary valued gap for $\gamma = \pi$, which we discuss in subsection 3.4.1, and have similar profiles to figure 3.5(c).

One of the most relevant properties that arises due to topology is the protection of the edge modes from disorder in the axis of the chain. In figure 3.6, we apply disorder in the form of a random positive or negative shift to each particle's position in the chain axis, and measure the root mean square of the disorder as a percentage of $\Lambda = |\beta - 1|$. When the disorder is 50%, the system is within one standard deviation of the topological phase transition, where the particles are equally spaced.

In figure 3.6(a), a random choice of disorder is scaled smoothly for different choices of β, causing the bulk modes (blue) to enter and eventually close the gap at around 50%. These bulk modes also become localised [175], with example mode profiles in figure 3.6(b). The edge modes (yellow) separate in energy until they are lost in the

bulk, but survive for high levels (sometimes greater than 20%) of disorder, especially for larger $|\beta - 1|$. Figure 3.6(c) shows the mode profiles of the two edge modes for two joined chains with 20% disorder and opposite Zak phases, which illustrates the continued existence of the edge modes in disordered systems. These longitudinally-polarised disorder-protected edge modes act as plasmonic hotspots, which can be positioned anywhere at the interface of two chains with opposite Zak phases.

3.4 FURTHER BAND DISCUSSION

3.4.1 Complex bands

In any system featuring losses or retardation, one of the wavevector or frequency must be complex [176]. This is typically chosen depending on the physics of the studied system. Here we discuss the importance of this with regards to a plasmonic TI.

For non-Hermitian solid state topological insulators, the eigenvalues are complex and the Bloch wavevector has real components, making the choice of real q_x and complex frequency natural for comparison. Figure 3.7(a) shows the real and imaginary parts of the Bloch band structure (red and green lines) in the case where there is a crossing in the real frequency axis, and the gap still has an imaginary part. We can visualise these bands as curves embedded in three dimensions, as in figure 3.7(b). As we have seen in section 1.4, it is necessary to take into account both the real and imaginary parts of the frequency when considering the topological nature of a non-Hermitian system [105, 115]. Here, and for this system in general, the complex gap is a point gap.

The complex gap allows for the unambiguous identification of each band, which are labeled with different colours in figure 3.7 for clarity. This then permits the calculation of Zak phases. For a finite chain, we still find bulk modes (blue dots) which follow the bands and edge modes (yellow dots) which sit in the complex valued gap.

All of the retarded and radiative band structures presented in this chapter have imaginary components to the frequency, whose inverse is equal to the lifetime of the mode. Lifetimes of edge modes are comparable to those of the bulk modes and plasmons localized to a single particle. For example, the edge modes in figure 3.7 have a lifetime on the order of 10 fs. The presence of these imaginary parts suggest that it may be necessary to use an evanescent wave to excite the modes.

3.4.2 Full Maxwell's equations bandstructures

In this section we present full Maxwell's equations simulations of the band structures of equally spaced chains, $\beta = 1$, for the d and a parameters featured in figure 3.2. The main purpose of this is to confirm the validity of the CDE method used in this thesis for studying band structures of chains with particles of this size and spacing. The calculations were performed using commercial software. Lumerical calculations are by Xiaofei Xiao and Comsol calculations by Paloma A Huidobro, both contributing authors to the paper [1].

In figure 3.8, we compare the CDE (blue line) to Lumerical finite difference time domain (FDTD) Solutions simulations with the same Drude model [165] (red circles),

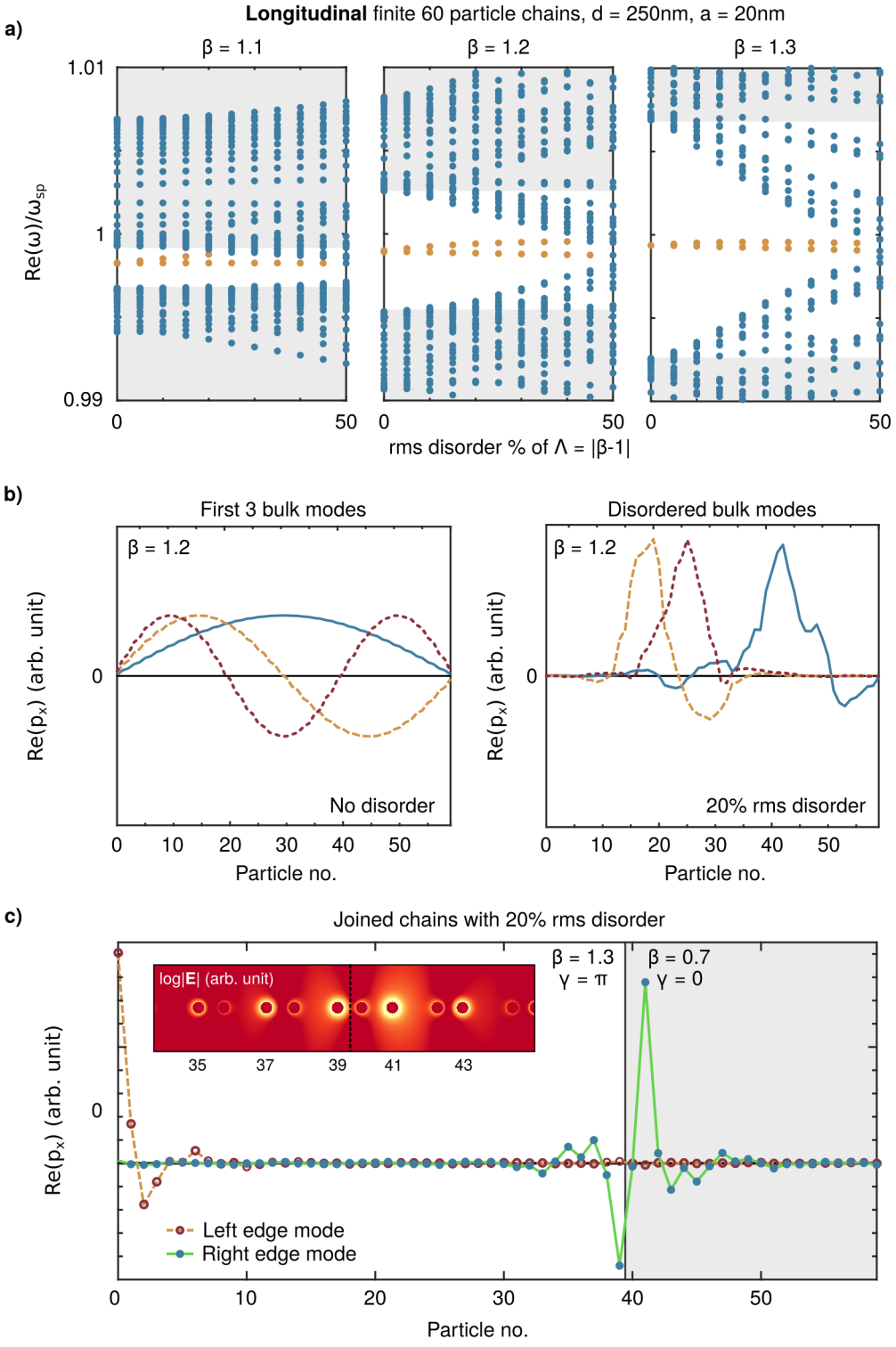

Figure 3.6: (a) Random disorder with the same seed is applied with increasing strength along the x axis for three different choices of β. The original bulk is marked in grey, bulk modes are blue and edge modes are yellow. (b) Bulk modes of the of the system without disorder and with disorder, using the same seed as (a). (c) Joined chains with opposite $|\beta - 1|$ values interfaced between particles 39 and 40. Disorder uses a different seed to (a) and (b). Inset: $\log|\mathbf{E}|$ field outside of the particles. Dark red corresponds to the weakest field, and bright yellow represents a stronger field.

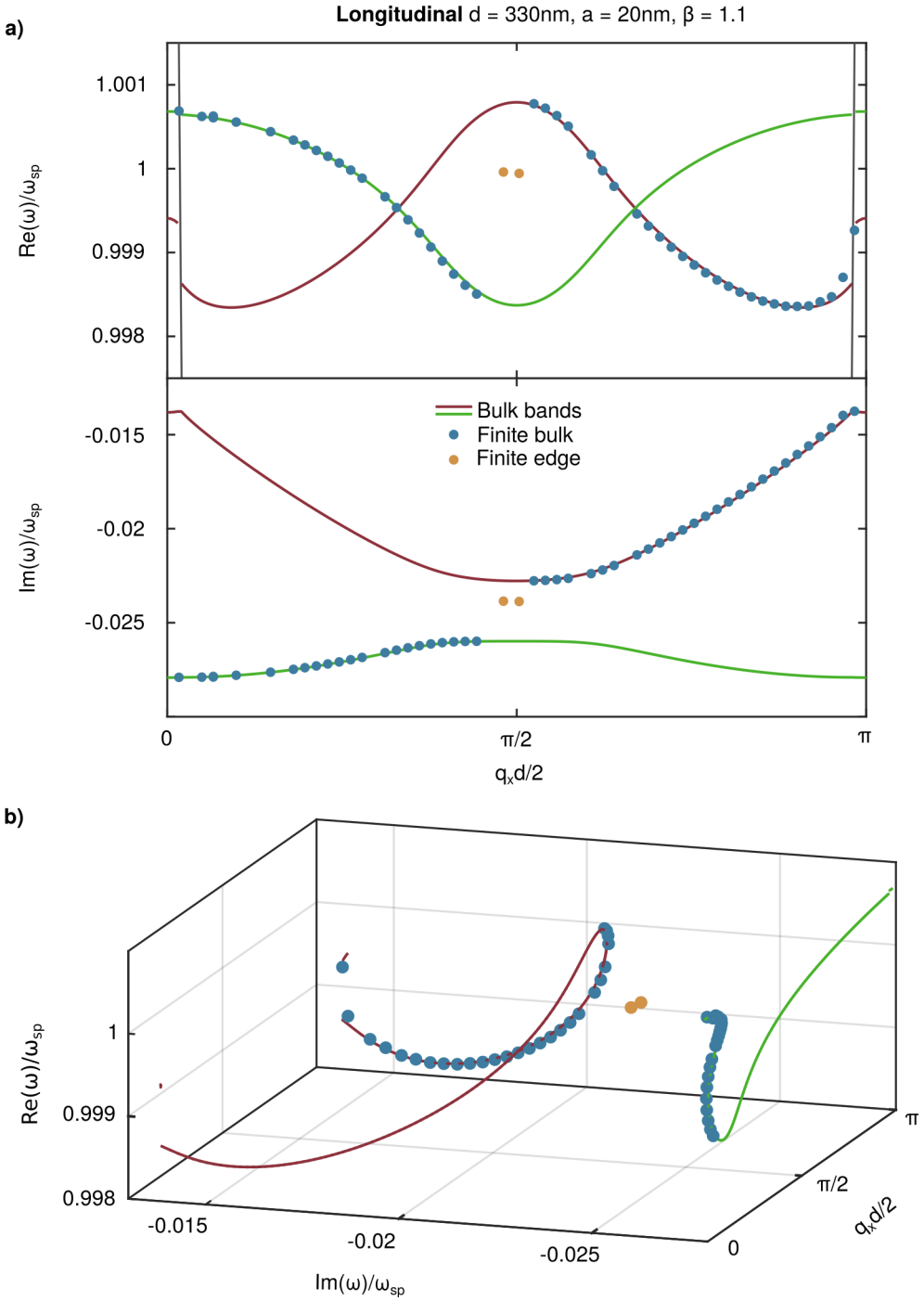

Figure 3.7: (a) Real and imaginary parts of the band structure (red and green lines) for $d = 300$ nm, $a = 20$ nm, $\beta = 1.1$, overlaid with modes for a finite 60 particle chain of the same geometry (blue and yellow dots). The two bulk bands are coloured differently for clarity. (b) 3d representation of the above two projections, demonstrating that the curve is embedded in a 3d space.

and also with experimental data for the dielectric function $\epsilon(\omega)$ of gold from Johnson and Christy [177] (green crosses). This captures the interband transitions, which are ignored in the Drude model. We consider the equally spaced chain with only a single particle per unit cell, so we only see one band in the BZ.

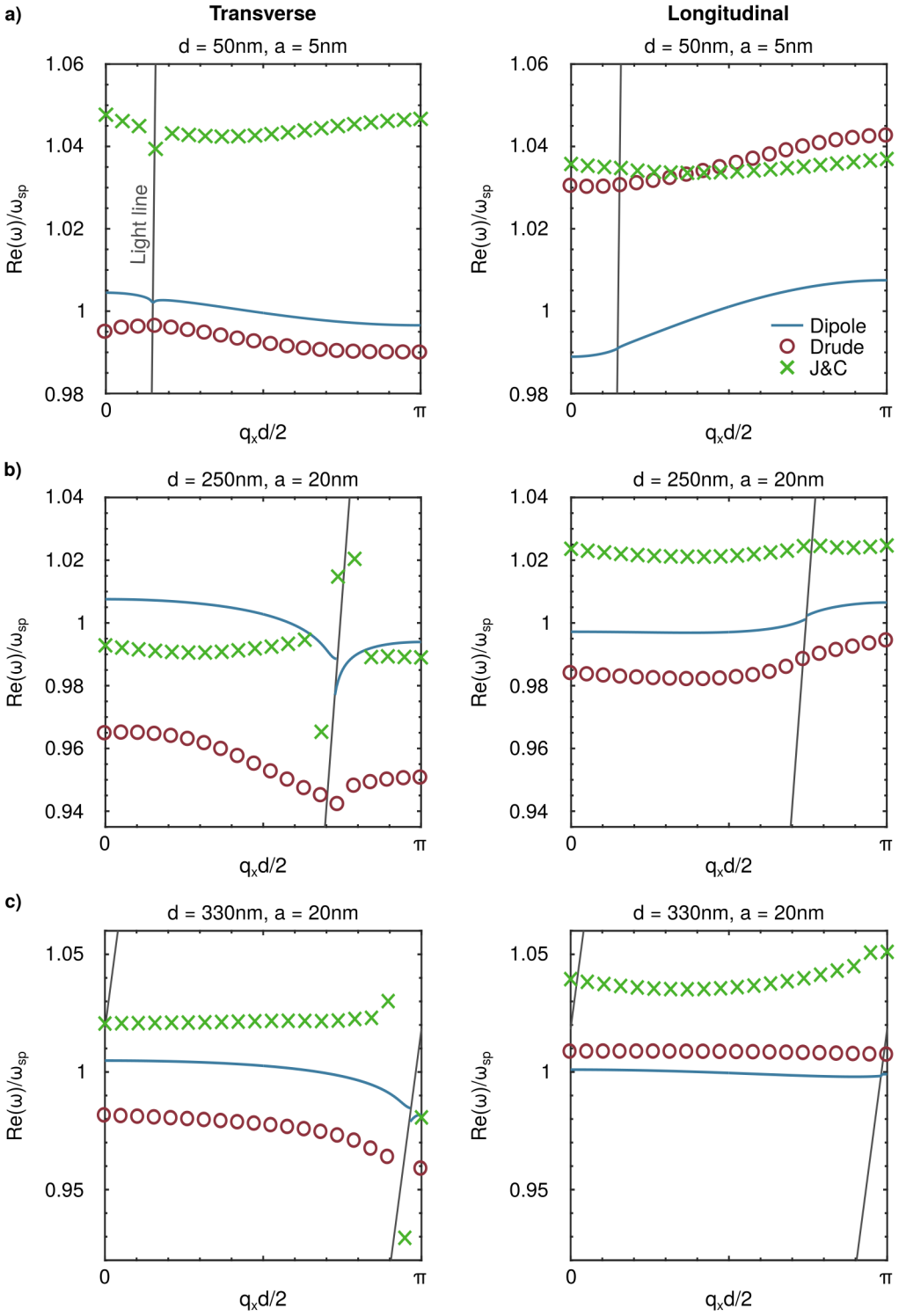

Figure 3.8: Comparison of coupled dipole equation bands (blue line) with FDTD simulations using the same Drude model as in the manuscript (red circles) and experimental results from Johnson and Christy (green crosses). The error when comparing either of the CDE results to either of the FDTD results is less than 6%. Simulations by Xiaofei Xiao.

Although the differences between the methods in figure 3.8 might appear large, the figures are zoomed in to make the best use of space and in fact show that the

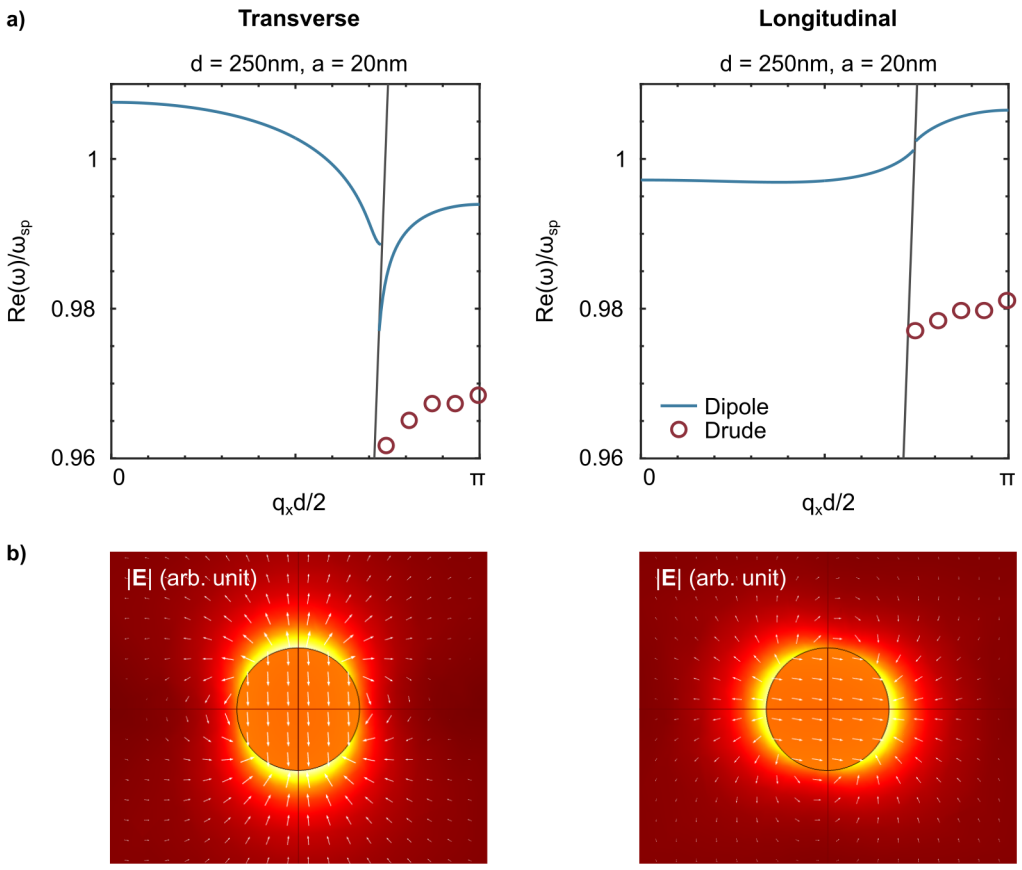

Figure 3.9: (a) Comparison of coupled dipole approximation bands (blue line) with FEM simulations below the light line, using the same Drude model with losses reduced by a factor of 10 (red circles). The error between the results is less than 5% (b) Representative electric fields $|\mathbf{E}|$ of one of the modes in (a), excited by an evanescent wave. Dark red corresponds to the weakest field, and bright yellow represents a stronger field. Simulations by Paloma A Huidobro.

CDE (blue line) is a good approximation to the multipolar simulations, with an error smaller than 6%. When the Drude model is used (red circles), there is a small shift but a similar band shape is recovered, featuring evidence of polariton-like behaviour at the light line. The inclusion of the full experimental dielectric function (green crosses) changes the shape of the bands more dramatically due to the presence of interband transitions, although this should not have an effect on the qualitative topological properties of the system. The inclusion of a different dielectric function changes the polarisability of the particles $\alpha(\omega)$, but does not change whether gaps close, which is dictated by the zeros of the off diagonals of the Hamiltonian matrix in equation 3.12. This is also explained in subsection 3.2.4

For figure 3.8, an FDTD solver (Lumerical) was used to search the eigenfrequencies by placing a number of randomly oriented and randomly distributed dipole sources to excite all modes of interest for the system. A cloud of randomly distributed time monitors was applied to obtain a spectrum with peaks at the resonant frequencies using the Fourier transform of the time signal. By running a parameter sweep over a range of the Bloch vectors and finding the local maxima of the spectrum for each Bloch vector, the band structure can be found [178]. However, according to the Lumerical webpage regarding simulations with loss, 'the fields decay more quickly when

more loss is introduced, and the useful part of the time signal that is collected by the time monitors is shortened. The Fourier transform of the time signal becomes noisy, making it difficult to extract the resonance peaks' [179]. Therefore, special settings need to be chosen to excite the interesting modes and make the bands more visible. In our simulation, we also used symmetry or antisymmetry on the y and z axes to isolate the longitudinal and transverse modes.

In figure 3.9(a), we compare the CDE (blue line) to Comsol finite element method (FEM) simulations with the same Drude model, with losses reduced by a factor of 10 [165] (red circles). In the simulation, an evanescent wave is incident on the chain and peaks in absorption are used to construct the bands below the light line. Reduced losses help to resolve these peaks. Again, the differences between the bands are small, with an error below 5%. Unlike the messy incident fields created by dipole clouds in the FDTD method, evanescent waves allow us to clearly see the near fields of the particles at the modes. Example near fields in the xy plane are shown in figure 3.9(b), where colour shows the magnitude of the field $|\mathbf{E}|$ and white arrows the direction and size of the field. These modes are represented well by transverse and longitudinal dipoles.

There are some limitations to these approaches to calculating the band structures, as Lumerical struggles with simulations featuring lossy systems like this one, and it is difficult for Comsol to solve for eigenmodes with the combination of open and periodic boundary conditions required to find band structures of a chain of 3d particles.

3.5 EXTINCTION CROSS SECTIONS

Although band structures and eigenmodes are the clearest theoretical way to probe topological properties of the system, it is not trivial for experimentalists to measure band structures directly. One method is to probe the chain with an incident electric field, and measure the extinction of the chain at a range of frequencies. The incident field excites some modes of the chain, depending on symmetries of the bands and the electric field. Modes which are excited have greater extinction, in much the same way as a single particle resonance, as depicted in subsection 2.2.1. In this section, we discuss and present preliminary results on the extinction cross sections of the plasmonic topological chain.

As we saw in subsection 2.2.2, the extinction cross section of a system of nanoparticles coupled by dipolar fields can be calculated from

$$C_{ext} = \frac{k}{\epsilon_0 \epsilon_B |\mathbf{E}_0|^2} \sum_{j=1}^{N} \mathrm{Im}(\mathbf{E}_I^*(\mathbf{r}_j) \cdot \mathbf{p}_j), \tag{3.31}$$

where $\mathbf{E}_I$ is the incident field, which here is given by a linearly polarized plane wave of the form

$$\mathbf{E}_I(\mathbf{r}) = \mathbf{E}_0 e^{i\mathbf{k}\cdot\mathbf{r}}, \tag{3.32}$$

where the harmonic time dependence of the field is not written explicitly. $\mathbf{E}_0$ contains the polarisation and amplitude of the field.

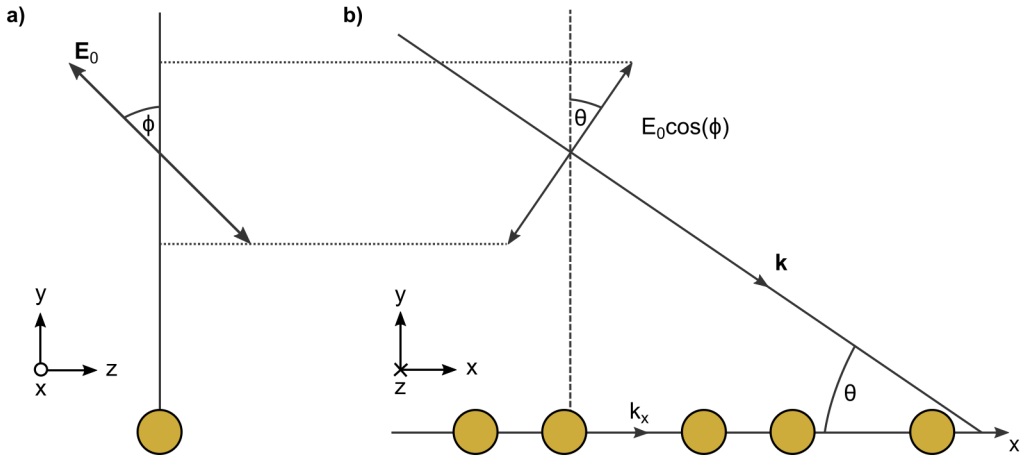

Figure 3.10: Diagram of an incident plane wave on a chain of nanoparticles

The wave vector **k** fixes the possible polarisations of the incident wave. Without loss of generality, we consider an incident plane wave with **k** in the xy plane, with arbitrary polarisation given by $\mathbf{E}_0$, as in figure 3.10. Given that the polarisation is at an angle ϕ from the xy plane, we have (for $|k_x| \leqslant \sqrt{\epsilon_B}\omega/c = k$),

$$E_0^x = E_0 \frac{\sqrt{k^2 - k_x^2}}{k} \cos\phi, \tag{3.33}$$

$$E_0^y = E_0 \frac{k_x}{k} \cos\phi, \tag{3.34}$$

$$E_0^z = E_0 \sin\phi. \tag{3.35}$$

As we increase the magnitude of k_x further so that $|k_x| > k$, the other component k_y becomes imaginary, resulting in an evanescent wave in the y direction. This corresponds to crossing the light line at $k_x = \pm k$. The polarisation is then given by

$$E_0^x = 0, \tag{3.36}$$

$$E_0^y = E_0 \cos\phi, \tag{3.37}$$

$$E_0^z = E_0 \sin\phi. \tag{3.38}$$

Fixing ϕ and choosing k_x appropriately allows us to calculate the extinction efficiency $Q_{ext} = C_{ext}/\pi a^2$ for any direction and polarisation of an incident plane wave. However, it is difficult to excite longitudinal modes using this method. For $\theta \neq \pi/2$, which is the same as $k_x \neq 0$, the angle of the polarisation is such that a transverse component of the chain must be excited. When we pass the point where $|k_x| > k$, we see from equation 3.36 that there is no more longitudinal component and we excite only transverse modes. Therefore, if $\phi = 0$ we excite a mixture of longitudinal and transverse modes above the light line, and only transverse modes below the light line. If $\phi = \pi$ we excite only transverse modes.

Figure 3.11 shows normalised extinction cross sections for finite 300 particle chains with $d = 250\,\text{nm}$, $a = 20\,\text{nm}$ and $\beta = 1.3$. The $\phi = \pi/2$ case on the left is overlaid with the real part of the transverse bands, and the $\phi = 0$ case on the right is overlaid with

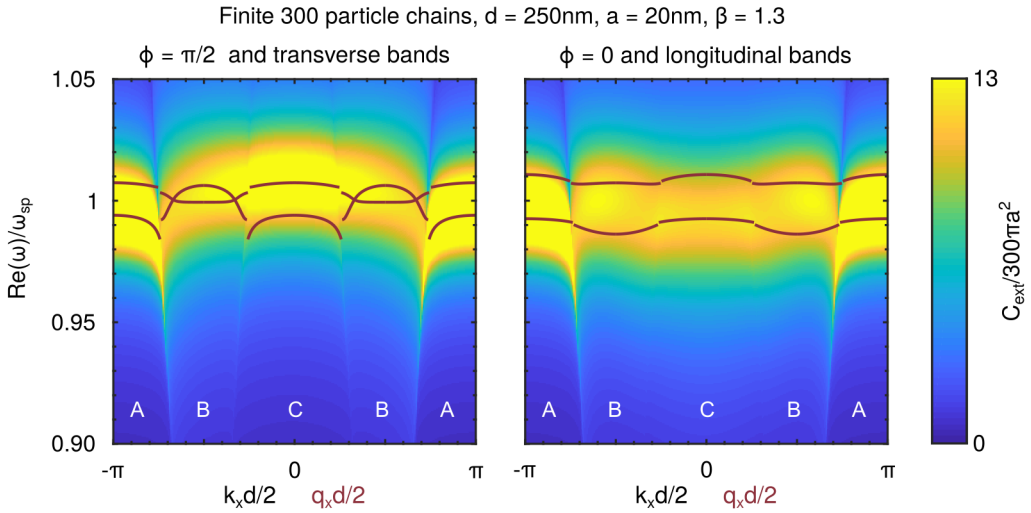

Figure 3.11: Extinction cross sections of 300 particle chains, for $\phi = \pi/2$ and $\phi = 0$, with the real part of the corresponding transverse and longitudinal bulk band structures overlaid in red.

the real part of the longitudinal bands, each with the same Bloch vector component q_x value as the wavevector component k_x. In each of the panels the light lines are visible as sharp changes in the extinction, and separate the panels into 3 regions, labelled A, B and C. Region A is under the first set of light lines, $kd \pm k_x d = 0$. In this case the lower band is excited because the symmetry of the modes in the band matches up with the symmetry of the incoming plane wave, which does not excite the modes in the upper band. In region C, under the second set of light lines, $kd - k_x d = \pm 2\pi$, the upper band is excited instead. The extinction does not appear to align with either of the bands in region B.

In the case of $\phi = 0$, on the right hand side of figure 3.11, the plane wave is longitudinally polarised for $k_x d/2 = 0$ and gradually becomes transversely polarised until the light lines $kd \pm k_x d = 0$. The consequence is that in region A the extinction cross section is identical to the $\phi = \pi/2$ case on the left, and the lower transverse band is excited. In region C, where the plane wave is mostly longitudinally polarised, the lower longitudinal band is excited. Once again region B has the least correspondence between extinction and bands.

3.6 SUMMARY AND DEVELOPMENTS

In this chapter we have presented a way to study a staggered one dimensional chain of coupled dipolar particles and applied it specifically to a staggered chain of metallic nanoparticles. We found that band structures of the staggered plasmonic chain are gapped in complex frequency by a point-like gap, and therefore have trivial and topological phases which we identified using the Zak phase.

For longitudinal polarisation, there are simple topological properties. For $\beta < 1$ the chain is trivial, and for $\beta > 1$ it is topological, which results in edge modes for chains in free space and at the interface of chains with opposite Zak phase. These edge modes are strongly protected from disorder in the axis of the chain, providing

a possible avenue for plasmonic hot spots which are protected by manufacturing defects. This is in spite of the fact that SLS is broken by A to A and B to B hopping, which adds an identity term to the bulk Hamiltonian. This identity term does not affect the Zak phase because it has no impact on the eigenmodes.

In the case of transverse polarisation we found a surprising retardation-induced phase transition when $\beta \neq 1$, caused by the long range term in the Green's function. We did not present edge modes in the case of transverse polarisation. We will elaborate on this in chapters 4 and 5.

We also presented extinction cross sections of the system for various parameters. The study of the extinction cross sections and their correspondence with the band structures, and whether the cross sections contain any information about the topology of the system, is a promising area for research beyond this thesis. This understanding could aid experimental studies of the system.

At the time of writing, we are in communication with Päivi Törmä's group at Aalto University in Finland regarding the use of edge modes for lasing in experiments. This group already used bulk modes of an equispaced plasmonic chain for the same purpose [180].

Since the publication of the results of this chapter, several other papers have appeared which make use of the Lerch transcendent method to analyse other one dimensional systems which behave like coupled dipoles, such as cold atoms [181], phonon polaritons [182] and dispersive gyromagnetic lattices [183]. It is exciting that this work has inspired or helped others to study these interesting systems, which are mathematically extremely similar to ours apart from nanoparticle specific aspects, like polarisability.

Some of these works raised questions about the existence or breakdown of bulk-edge correspondence in the transverse-polarised case. In the next chapter we outline their ideas and go on to study and explain these topological phenomena in more detail.

4 BULK-EDGE CORRESPONDENCE IN THE PLASMONIC CHAIN

In chapter 1, we introduced the concept of bulk-edge correspondence (BEC), the agreement between properties of the bulk in an infinite, or periodic boundary condition, system with properties of the edge in a finite, or open boundary condition, system. Typically, this is the connection between the topological number, in our case the Zak phase, with the existence or non existence of edge states. At the time of writing, one of the main issues in the theory of non-Hermitian TIs is that BEC is not always present, leading to a few proposed solutions, as discussed briefly in chapter 2.

As we showed in chapter 3, the Zak phase agrees closely with the existence of edge states in the case of longitudinal polarisation. However, the transverse case is much more complicated. In this chapter, we address a couple of the relevant proposed solutions for BEC breakdown in non-Hermitian systems and discuss in detail the breakdown of BEC in the transverse polarisation.

Aside from sections 4.1 and 4.6, this chapter consists mostly of material adapted from an article in Nanophotonics and its supplementary material, for which the author of this thesis was first author [184]. It is reproduced here, in altered form, under creative commons license CC BY 4.0 [88].

4.1 INTRODUCTION

After the publication of the results of the previous chapter, Wang and Zhao published two works which utilised the Lerch transcendent approach for other dipole-dipole interacting systems. These were staggered chains of cold atoms [181] and staggered chains of Silicon Carbide (SiC) [182]. In the second of these, Wang and Zhao presented an instance where, for the transverse polarisation, the Zak phase and existence of edge states disagreed. In an attempt to rectify this, they applied a modified Zak phase for non-Hermitian systems, suggested by Yao and Wang [119].

Yao and Wang's idea stems from a phenomenon where open boundary conditions in non-Hermitian systems can not only introduce edge states but also affect the entire bulk spectrum and eigenmodes. A common result is the partial localisation of bulk modes at the edges of the 1d system, known as the non-Hermitian skin effect [121]. Some systems which exhibit this skin effect also exhibit BEC breakdown.

In an effort to capture the skin effect in calculations of the Zak phase, Yao and Wang presented a non-Bloch modification. Their proposal is equivalent to letting the Bloch wavevector q_x take complex values, as opposed to the usual real values in the BZ, as a sort of generalised BZ. The imaginary part of q_x captures the decay of the bulk modes into the chain when there is localisation.

Wang and Zhao applied this logic to their SiC system, calculating a Zak phase with complex q_x and finding that it now agreed with the presence of the edge mode for their specific choice of parameters. However, this is only for one set of parameters, and the choice of imaginary part for q_x is fairly arbitrary. As discussed in the pre-

vious chapter, and as noted by Wang and Zhao, the Zak phase calculation depends only on the off-diagonals of the bulk Hamiltonian. The complex q redefinition does not alter this. As we will show in this chapter, the breakdown of BEC is driven by the on-diagonal terms of the Hamiltonian; the complex q redefinition cannot take this into account and therefore cannot solve the problem of BEC breakdown in this system.

Another idea regarding the issue of BEC breakdown in non-Hermitian systems is that topological properties should actually be considered in the context of the singular-value decomposition (SVD), rather than the eigensystem of the bulk Hamiltonian [122]. In systems where the bulk modes are affected by open boundary conditions the SVD is unaffected, and SVD edge modes can be found in a gap in the SVD spectrum. In section 4.6, we will show that the SVD approach does not solve the problem of BEC breakdown in our system.

In any staggered chain of coupled dipoles, the breakdown of BEC is caused by the breaking of sublattice symmetry (SLS) by the A to A and B to B hoppings in the system, which contribute an identity term to the Bloch Hamiltonian. We show that, in the longitudinal case, this is small enough that topological protection of edge states remains, but in the transverse case the longest range term causes BEC breakdown for larger spacing of the chain and wavevectors q_x. Although the system is non-Hermitian, this method of BEC breakdown occurs also in Hermitian systems, as demonstrated by Pérez-González *et al.* [127].

Since realistic photonic systems, like ours, often feature some degree of long range hopping, it is necessary to understand how it affects the existence of BEC. In this chapter we study BEC breakdown in this realistic physical model, and also a simpler non-Hermitian SSH model, defining a model-specific measure of SLS breaking to elucidate where BEC breakdown occurs.

4.2 MODELLING THE PLASMONIC CHAIN II

The mathematical model applied in this chapter is similar to that of chapter 3, with a couple of important differences. The most significant change is to linearise the Green's functions, which reduces the numerical difficulty of the model and allows consideration of longer chains. This restricts the radius of the particles but, as discussed in section 3.2.4, that doesn't change the qualitative topological properties of the system.

We start once again with the coupled dipole equations (CDEs), given by

$$\frac{1}{\alpha(\omega)}\mathbf{p}_n = \frac{k^2}{\epsilon_0}\sum_{j\neq n} G(\mathbf{r}_{nj},\omega)\mathbf{p}_j, \tag{4.1}$$

where $\mathbf{p}_n$ is the dipole moment of the n^{th} particle, $G(\mathbf{r}_{nj},\omega)$ is the Green's dyadic between the positions n^{th} and j^{th} particles at frequency ω, and $\alpha(\omega)$ the polarisability of the particles.

We use the MLWA for the polarisability,

$$\alpha(\omega) = \frac{\alpha_{QS}(\omega)}{1 - i\frac{k^3}{6\pi\epsilon_0}\alpha_{QS}(\omega) - \frac{k^2}{4\pi\epsilon_0 a}\alpha_{QS}(\omega)}, \tag{4.2}$$

as discussed in subsection 2.2.1. The wavevector magnitude is given by $k = \sqrt{\epsilon_B}\omega/c$, where ϵ_B is the background dielectric and $\alpha_{QS}(\omega)$ is the QS polarisability, given by

$$\alpha_{QS}(\omega) = 4\pi\epsilon_0 a^3 \frac{\epsilon(\omega) - \epsilon_B}{\epsilon(\omega) + 2\epsilon_B}. \tag{4.3}$$

$\epsilon(\omega)$ is the dielectric function of the particles, in this work given by the Drude model,

$$\epsilon(\omega) = \epsilon_\infty - \frac{\omega_P^2}{\omega^2 + i\omega/\tau}. \tag{4.4}$$

In this chapter, we consider silver nanoparticles in air, with $\epsilon_\infty = 5$, $\omega_P = 1.36 \times 10^{16}\,\mathrm{rad/s}$, $1/\tau = 5.88 \times 10^{13}\,\mathrm{rad/s}$ [156] and $\epsilon_B = 1$. We take small particles with radius $a = 5\,\mathrm{nm}$, leading to a single particle surface plasmon resonance (SPR) frequency of $\omega_{sp} = 5.13 \times 10^{15}\,\mathrm{rad/s}$. This SPR frequency is calculated from the MLWA polarisability instead of the QS method shown in subsection 2.2.1, but 5 nm particles are small enough that the MLWA and QS approximations for the polarisability give very similar results. However, the use of MLWA gives the potential to study larger particles. We can use the MLWA, instead of the radiative correction used in chapter 3, because we linearise the Green's functions by making the approximation that $\omega = \omega_{sp}$ in the Green's dyadic. This simplifies calculations by removing ω dependence from the bulk Bloch Hamiltonian, and is a good approximation for small particles because ω varies faster in the polarisability than the Green's function. For larger particles, the approximation becomes inaccurate at the light lines, where $kd \pm q_x d = 0 \mod 2\pi$.

As we have seen in the previous chapter, for the 1d chain the x, y and z components of equation 4.1 decouple. This leads to two distinct polarisations of the particles, longitudinal (x) and transverse (y and z). We relabel particles by unit cell and sublattice, leading to a set of equations

$$\begin{aligned}
\frac{d^3}{\alpha(\omega)} p^A_{\nu,n} &= \sum_{m\neq n} \tilde{g}^\nu(m-n) p^A_{\nu,m} + \sum_m \tilde{g}^\nu(m-n+\beta/2) p^B_{\nu,m}, \\
\frac{d^3}{\alpha(\omega)} p^B_{\nu,n} &= \sum_{m\neq n} \tilde{g}^\nu(m-n) p^B_{\nu,m} + \sum_m \tilde{g}^\nu(m-n-\beta/2) p^A_{\nu,m},
\end{aligned} \tag{4.5}$$

where $\nu = x, y, z$ represents the direction of polarisation and the linearised reduced Green's functions $\tilde{g}^\nu(\bar{r})$ are given by

$$\tilde{g}^x(\bar{r}) = 2\frac{e^{ik_{sp}d|\bar{r}|}}{4\pi\epsilon_0|\bar{r}|^3}\left[1 - ik_{sp}d|\bar{r}|\right], \tag{4.6}$$

$$\tilde{g}^{y,z}(\bar{r}) = -\frac{e^{ik_{sp}d|\bar{r}|}}{4\pi\epsilon_0|\bar{r}|^3}\left[1 - ik_{sp}d|\bar{r}| - (k_{sp}d)^2|\bar{r}|^2\right], \tag{4.7}$$

with $\bar{r}$, the spacing between particles divided by d, and $k_{sp} = \sqrt{\epsilon_B}\omega_{sp}/c$, the mangitude of the wavevector of light with the same frequency as the single particle surface plasmon resonance. This is the same as the set of equations 3.8 and 3.9, except for the linearisation $k \mapsto k_{sp}$, and the definition of a 'reduced' Green's function in which

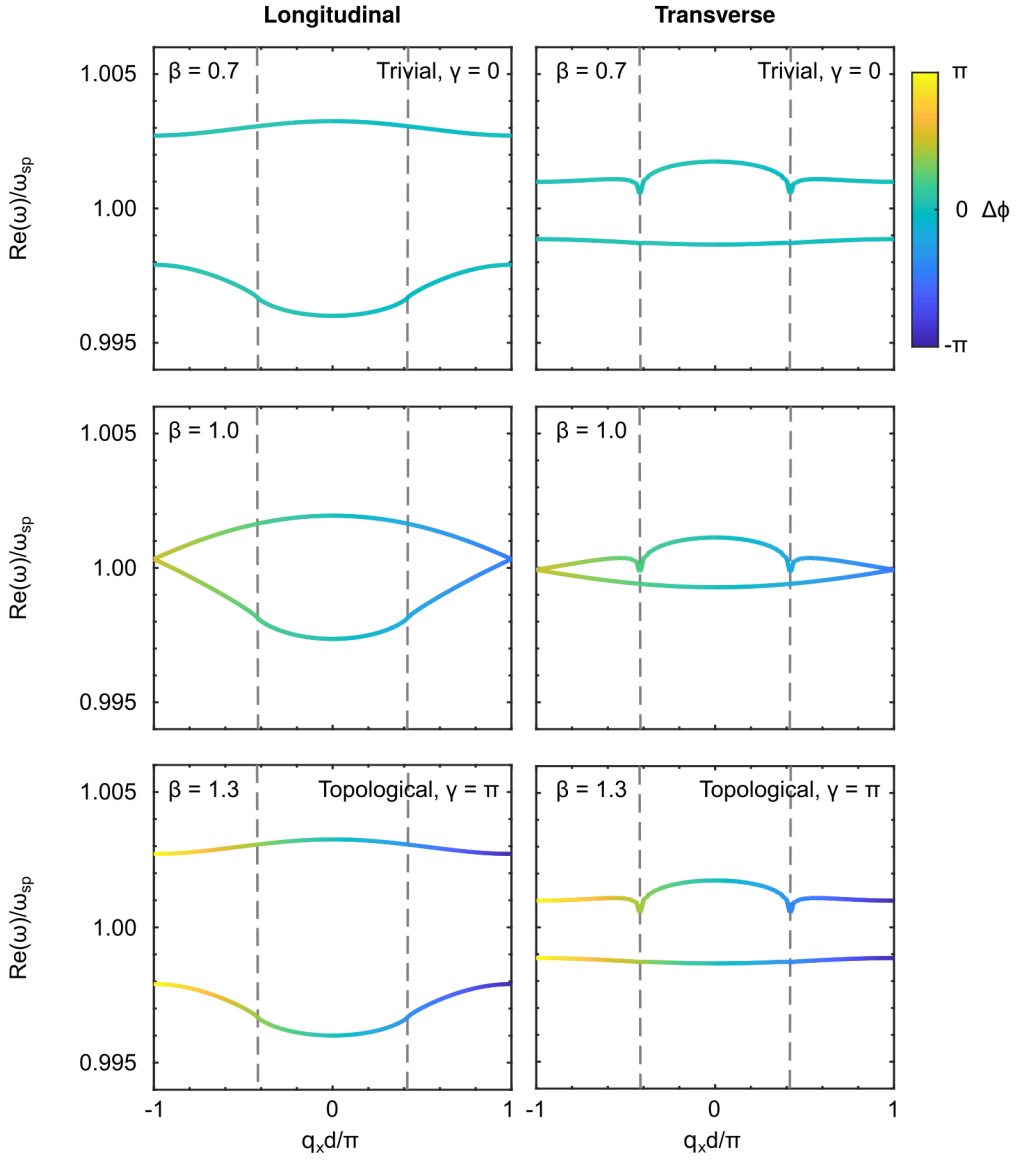

Figure 4.1: Real part of the dispersion relation of the topological plasmonic chain with $a = 5\,\mathrm{nm}$ and $k_{sp}d = 0.42\pi$ for the longitudinal and transverse polarisations, which corresponds to $d = 77\,\mathrm{nm}$. Band colouring shows how ϕ changes for each band away from the centre of the BZ. Not depicted is that the upper and lower bands have a phase difference of π.

some constants have been shuffled around to improve the clarity of some figures later on.

We again refer to the third term in the transverse reduced Green's function, equation 4.7, as 'long range', as it decays proportional to the inverse of the particle separation. In addition, we note the finite lifetime of the plasmons, which causes decoherence between the nanoparticles. Dipoles can only interact coherently if they have separation less than $c\tau/\sqrt{\epsilon_B}$, which we take into account by setting $g(r)$ to zero if $rd > c\tau/\sqrt{\epsilon_B}$. The addition of the plasmon lifetime based cutoff removes physically unrealistic divergences at the light line.

4.2.1 Properties of the bulk II

Although the model is very similar to that of the previous chapter, there are enough subtle differences that it benefits us to go through the basic bulk properties of the system once more. For an infinite chain we relabel particles by unit cell and sublattice A and B and apply Bloch's theorem to arrive, once again, at the eigenvalue problem

$$\mathcal{G}_\nu(\omega, q_x)\begin{pmatrix} p_\nu^A \\ p_\nu^B \end{pmatrix} = \frac{d^3}{\alpha(\omega)}\begin{pmatrix} p_\nu^A \\ p_\nu^B \end{pmatrix} = \mathcal{E}(\omega, q_x)\begin{pmatrix} p_\nu^A \\ p_\nu^B \end{pmatrix}, \tag{4.8}$$

where q_x is the x-component of the Bloch vector. Here the matrix $\mathcal{G}$ and the eigenvalues $\mathcal{E}$ are different to chapter 3 because of the use of the reduced Green's functions. This is summarised by $\mathcal{E}(\omega, q_x) = d^3/\alpha(\omega)$. The elements of the 2×2 Bloch Hamiltonian matrix are given by

$$\begin{aligned} \mathcal{G}_\nu^{11} &= \mathcal{G}_\nu^{22} = \sum_{n\neq 0} \tilde{g}^\nu(n) e^{iq_x d n}, \\ \mathcal{G}_\nu^{12}(\omega, q_x) &= \sum_n \tilde{g}^\nu(n+\beta/2) e^{iq_x d n}, \\ \mathcal{G}_\nu^{21}(\omega, q_x) &= \sum_n \tilde{g}^\nu(n-\beta/2) e^{iq_x d n}, \end{aligned} \tag{4.9}$$

where the superscript indicates the element's row and column position the matrix. The matrix is non-Hermitian, which allows $\mathcal{E}$ to take complex values. Solving the equation for ω gives the bulk dispersion relation of the chain. As an example, we consider the case of $k_{sp}d/\pi = 0.42$, corresponding to $d = 77\,\text{nm}$, in figure 4.1, where we plot the real part of the dispersion relation for the longitudinal (left) and transverse (right) polarisations with $\beta = 0.7$, 1, and 1.3. The band structure is symmetric in q_x due to the inversion symmetry of the system.

As discussed in chapter 3, the relevant topological number of this system is the Zak phase [123] using the periodic gauge [96, 185], given by

$$\gamma = \frac{\phi(\pi) - \phi(-\pi)}{2} \mod 2\pi, \tag{4.10}$$

where $\phi(q_x d)$ is the relative phase between p_A and p_B. Although a variation on the Zak phase has been proposed which takes into account the non-Hermiticity of the system [119, 182], we will show that this Zak phase is sufficient here. In a system with BEC, a Zak phase of $\gamma = \pi$ ($\gamma = 0$) predicts the existence (non-existence) of topologically protected edge modes [128]. The colouring of the bands in figure 4.1 shows how ϕ changes for $q_x d$ moving away from the centre of the BZ. We see that for $\beta < 1$, $\gamma = 0$ and for $\beta > 1$, $\gamma = \pi$. There is a bandgap closure at $\beta = 1$ for complex ω, though the imaginary part is not shown in the figure, indicating a topological phase transition. At this value of β, the colouring of the bands shows that the Zak phase is not an integer.

Unlike in chapter 3, there is no ω dependence inside the Hamiltonian due to the linearisation of the Green's functions, which means the mapping between frequency and the eigenvalue $\mathcal{E}$ is contained entirely in the relation $\mathcal{E}(\omega) = d^3/\alpha(\omega)$.

As we have seen, the topological properties of the system emerge due to SLS, where a given Hamiltonian H satisfies the relation $\sigma_z H \sigma_z = -H$, where σ_z is the Pauli spin matrix. We argued in chapter 3 that, although $\mathcal{G}$ does not satisfy this relation it is equal to an SLS matrix plus an identity term, which is equal to $\mathcal{G}^{11}\mathrm{I}$. It therefore has the same eigenvectors as an SLS matrix, and so the Zak phase, which is calculated from the eigenvectors, is equal to that of the matrix $\mathcal{G} - \mathcal{G}^{11}\mathrm{I}$. In sublattice symmetric systems the eigenvalues come in positive and negative pairs, leading to a spectrum that is symmetric about $|\mathcal{E}| = 0$. The addition of the identity term shifts the bulk bands by $\mathcal{G}^{11}(q_x)$ in the complex plane.

However, a subtlety not noted in the original paper [1] was that, although the bulk topological number is the same, BEC is not necessarily preserved. In subsection 2.1.2 it was shown that, in an SLS system, the finite Hamiltonian also has an SLS operator which guarantees the existence and protection of zero eigenvalue edge modes. However, such an operator does not exist for a finite system which has bulk SLS broken by an identity term. Other studies have already argued that the existence of large enough A to A and B to B hopping causes the disappearance of edge modes in simple Hermitian and dipolar non-Hermitian systems [127, 181]. In summary, SLS is the ingredient which protects the edge states, and although inversion symmetry or an added identity term in the bulk still quantises the Zak phase, this does not guarantee BEC. In the next section, we study how varying the spacing of the chain through the parameter $k_{sp}d$ with fixed β affects the existence of BEC.

4.3 THE EFFECTS OF SUBLATTICE SYMMETRY BREAKING

In order to assess the impact of the A to A and B to B hoppings, we compare a realistic system with long range hoppings to a toy model which is identical except for the A to A and B to B hoppings, which are set to zero. This toy model therefore has SLS, and any differences in topological properties between the two systems must be due only to SLS breaking in the full model.

As discussed in chapter 3, the system has a point-like gap, meaning that a phase transition occurs when the bands cross a certain point in eigenvalue space. In the SLS case, this is the point given by $|\mathcal{E}| = 0$. The closing of the gap in ω is equivalent to the closing of the gap in $\mathcal{E}$, so it is enough to consider the eigenvalues $\mathcal{E}$, rather than ω, when examining the topological properties of the system. We therefore study the change of the absolute value of the eigenvalues, $|\mathcal{E}|$, as $k_{sp}d$ increases with fixed β. Ideally we would have manipulable 3d representation are there is the danger of some modes being obscured, but this seems to be the best way to present the data in print.

4.3.1 Eigenvalue plots

Longitudinal versus transverse polarisations

First we examine the eigenvalues of the longitudinal and transverse polarisations for a system with fixed $\beta > 1$. In the SSH model this has the Zak phase $\gamma = \pi$, and the longitudinal case behaves in the same way. In subsection 3.2.4, we saw that the transverse polarisation has a more complicated behaviour, with topological phase transitions associated with changing $k_{sp}d$. As $k_{sp}d$ increases, the Zak phase for β

above and below 1 swaps at specific values of $k_{sp}d$ in *retardation-induced topological phase transitions*. We showed in subsection 3.2.4 that these transitions are caused by the long range term in the Green's function, for example in equation 4.6. This term is insignificant for small enough $k_{sp}d$, but dominates for larger $k_{sp}d$.

These phase transitions are non-Hermitian features which occur at exceptional points, where one of the off-diagonal terms in the Bloch Hamiltonian is zero. The exceptional points come in pairs symmetrically around $\beta = 1$; if $\mathcal{G}_{12}$ is zero for some value of $k_{sp}d$ for $\beta = 0.7$, then $\mathcal{G}_{21}$ is zero for the same $k_{sp}d$ for $\beta = 1.3$. Therefore, for $\beta = 0.7$ the Zak phase is exactly opposite to $\beta = 1.3$, for all $k_{sp}d$. We will discuss these phase transitions in greater detail in chapter 5.

Figure 4.2(a) and (b) show $|\mathcal{E}|$ for $N = 600$ particle finite chains with $\beta = 1.3$ with changing $k_{sp}d$. The dark grey region represents the values of $k_{sp}d$ where the spacing of the particles is too small for the CDEs to be applicable because higher order modes come into play, as noted in section 2.2.1. SLS bulk modes are shown in red and full dipolar bulk modes in blue, with topologically protected edge modes coloured yellow.

Fig 4.2(a) shows the eigenvalues for the longitudinal polarisation which, for $\beta > 1$, has a Zak phase of $\gamma = \pi$ for all $k_{sp}d$. The top panel features topologically protected edge modes fixed at $|\mathcal{E}| = 0$ in the SLS case. In the full-dipolar case, these modes slightly deviate from zero as the particle spacing increases. Overall, the plots show that edge modes continue to exist in the full-dipolar longitudinal case as $k_{sp}d$ increases, which is consistent with other works that suggest that the longitudinal full-dipolar case always features BEC because A to A and B to B hoppings are 'small enough' for all $k_{sp}d$. We found similar results in chapter 3.

Fig 4.2(b) shows the transverse polarisation, with vertical black lines marking Zak phase transitions according to bulk calculations. The Zak phase in each region is given in the figure. In the SLS case, we see that the Zak phase is equal to that of the longitudinal chain for small $k_{sp}d$, and as $k_{sp}d$ increases the Zak phase swaps values. These are the aforementioned retardation-induced phase transitions.

In the SLS case, we can see that the existence and non-existence of zero edge modes is predicted by the Zak phase; the SLS finite chain has BEC. This suggests that the Zak phase calculation is sufficient for this system in this parameter regime despite the non-Hermitian skin effect, which led to the proposed Zak phase modification discussed at the start of this chapter. In the full dipolar case, however, the bulk and edge modes intersect before the first phase transition, and for higher $k_{sp}d$ there is no longer BEC. In this work we will call this BEC breakdown. We once again emphasise that the breakdown of BEC in this system is due to SLS breaking rather than non-Hermiticity. The fact that this happens before the first Zak phase transition is consistent with the notion that the breakdown occurs because the long range term gets 'too large', and therefore the A to A and B to B terms get too large, because the retardation-induced phase transitions are also related to the size of the long range term.

Another feature to note in the (blue) full dipolar case in figure 3(b) is the presence of modes outside the bulk in the $\beta = 1.3$ case, for $k_{sp}d/\pi > 0.93$ (2s.f.). These modes also exist in other $\beta > 1$ cases, and are localised to the edges of the chain. Importantly their existence or non existence does not line up exactly with the changing Zak phase and they have eigenvalues far from $|\mathcal{E}| = 0$. We therefore do not label these as topologically protected edge states. Even if they have some kind of topological

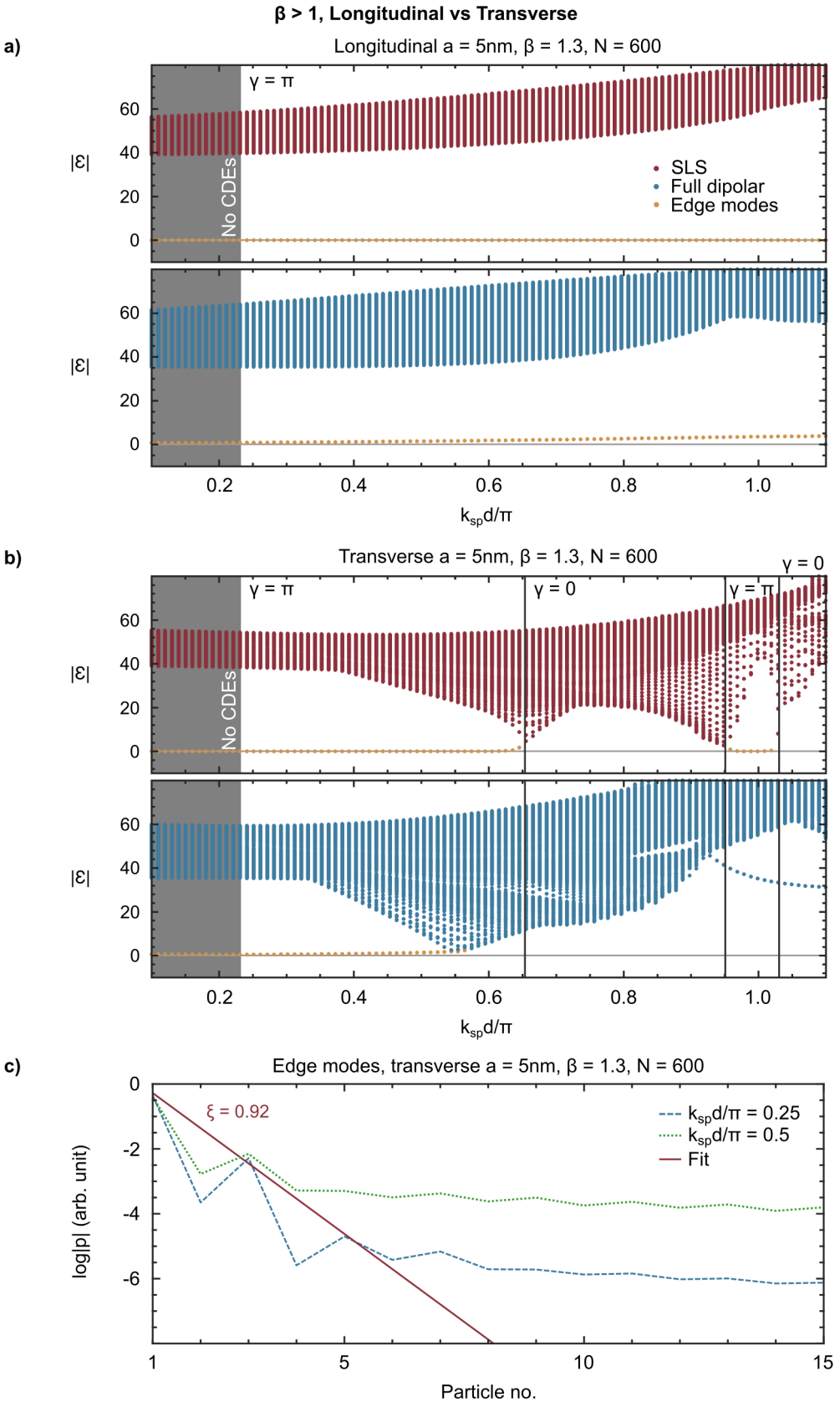

Figure 4.2: Eigenvalues of the SLS (red) and full dipolar (blue) topological plasmonic chain with changing $k_{sp}d$ for the (a) longitudinal and (b) transverse polarisations, with $\beta = 1.3$. Topologically protected edge modes are yellow. The dark grey area indicates the region where the CDEs are not valid as the particles are too closely spaced. Vertical black lines indicate Zak phase transitions as predicted by the closing of the bulk gap. (c) Edge mode profiles of (b) blue for different choices of $k_{sp}d$.

protection, the fact that their existence does not line up with the changing Zak phase indicates that BEC is still broken.

Fig 4.2(c) shows log plots of the dipole moments $|p|$ of two edge modes of the full-dipolar system, one far from the BEC breakdown at $k_{sp}d/\pi = 0.25$ and one close to the breakdown at $k_{sp}d/\pi = 0.5$. In an SLS system the edge modes are fully supported on one sublattice, which would in this case be the A sublattice. Due to the SLS breaking, edge modes spill into the B sublattice but we apply our exponential fit (red line) only to the A sublattice. Unlike the usual description of SSH model phase transitions, see subsection 2.1.2, the edge modes are not fully exponential. Instead, they appear to feature a highly localised edge part with localisation length ξ, which does not change as $k_{sp}d$ increases, and a bulk-like component that grows as $k_{sp}d$ increases. As BEC breakdown approaches there seems to be some mixing between the bulk and edge modes, possibly related to the non-Hermitian skin effect, or the nature of the long range hopping. In figure 4.2(a) and (b), the edge modes are highlighted based on how close they are to zero, how localised the edge part is, and how much larger the edge part is compared to the average of the bulk part.

Bulk-edge correspondence breakdown when β is less than 1

BEC breakdown is not a topological phase transition; edge modes are lost in the $\beta > 1$ case but not gained in the $\beta < 1$ case. We can see this by comparing a case where β is chosen symmetrically either side of $\beta = 1$, shown in figure 4.3 for $N = 600$ particle finite plasmonic chains, with (a) $\beta = 1.4$ and (b) $\beta = 0.6$.

First we note that the figures show retardation-induced Zak phase transitions at values symmetric around $\beta = 1$, as discussed in subsection 3.2.4. This is because the Zak phase is exactly opposite symmetrically either side of $\beta = 1$. In addition to this, the phase transitions happen for different $k_{sp}d$ in this case to the $\beta = 1.3$ case featured in figure 4.2(b), indicating that the location of the phase transitions depend on β, which will be explored further in chapter 5.

Considering the SLS (red) case for figure 4.3(a), we see that topologically protected edge modes exist in the regions where the Zak phase is $\gamma = \pi$, and do not in the regions where $\gamma = 0$. Again, this is the expected BEC. In the SLS case of figure 4.3(b) there is a slight discrepancy: the Zak phase transition occurs at $k_{sp}d/\pi = 0.81$ (2s.f.) and edge modes only reach zero at $k_{sp}d/\pi = 0.85$ (2s.f.), leading to a region where the Zak phase and edge modes don't agree. At $k_{sp}d/\pi = 0.85$ (2s.f.) and above the BEC is recovered. This discrepancy could be explained by the previously discussed non-Hermitian skin effect, which we discuss in more detail in section 4.6.

Now we examine the full dipolar (blue) case. In figure 4.3(a) the edge modes enter the bulk at $k_{sp}d/\pi = 0.68$ (2s.f.), well below the Zak phase transition. In figure 4.3(b) we see that edge modes don't appear at this same value of $k_{sp}d$, indicating that, although BEC breakdown leads to the disappearance of edge modes in the $\beta > 1$ case (a), it does not lead to the appearance of edge modes for the opposite $\beta < 1$ case in (b). This emphasises the difference between a phase transition and BEC breakdown.

Once again we observe, in the (blue) full dipolar case, the presence of modes outside the bulk for $\beta = 1.4$ which do not exist for $\beta = 0.6$, for $k_{sp}d/\pi > 0.91$ (2s.f.). Similarly to the $\beta = 1.3$ case in figure 4.2(b), these modes are localised to the edges of the chain but their existence does not agree with the Zak phase. In addition, they are far from $|\mathcal{E}| = 0$. Therefore, we do not label these as topologically protected

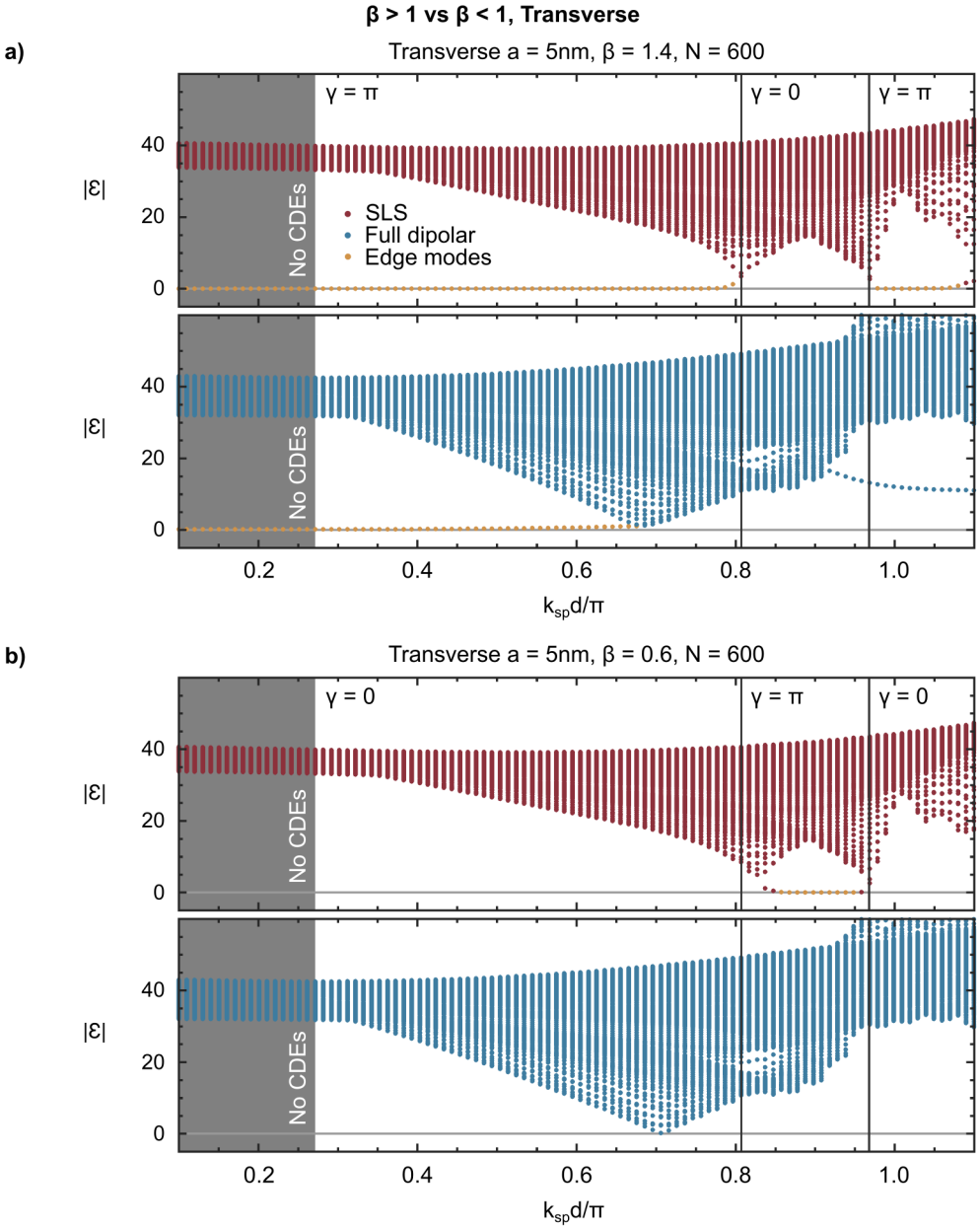

Figure 4.3: Eigenvalues of the SLS (red) and full dipolar (blue) topological plasmonic chain with changing $k_{sp}d$ for the transverse polarisation with (a) $\beta = 1.4$ and (b) $\beta = 0.6$. Topologically protected edge modes are yellow. The dark grey area indicates the region where the CDEs are not valid because the particles are too closely spaced. Vertical black lines indicate Zak phase transitions as predicted by the closing of the bulk gap.

edge states and consider the system to still have broken BEC. Although it appears that these are approaching the $|\mathcal{E}| = 0$ point in this plot, these modes actually move back up into the bulk as $k_{sp}d/\pi$ increases. This return and loss of modes outside of the band which do not correspond to the Zak phase continues to happen as $k_{sp}d/\pi$ increases.

Although, in the case of transverse polarisation, SLS is strongly broken as $k_{sp}d$ becomes large enough, the system still has a quantised Zak phase. This can be thought of as due to its inversion symmetry, represented by $\sigma_x \mathcal{G}(q_x)\sigma_x = \mathcal{G}(-q_x)$. While it no longer corresponds to the presence of edge modes, there is some evidence that the topological properties of inversion symmetric systems manifest in other ways [186, 187], and that there may be measurable consequences of topological phase, independent of the existence of edge modes [188]. We discuss this further in chapter 5.

4.3.2 Frequency plots

For completeness, we study the frequencies associated with the eigenvalues in the above figures. Figure 4.4 shows the real and imaginary parts of the frequency ω for a finite $N = 600$ chain with $a = 5\,\text{nm}$, $\beta = 1.4$ and varying $k_{sp}d$ on the x-axis. This corresponds exactly to the parameters in figure 4.3(a). Once again, SLS bulk modes are shown in red in (a) and full dipolar modes in blue in (b), with topologically protected edge modes coloured yellow. Black vertical lines correspond to phase transitions calculated from the bulk, with the Zak phase γ labelled.

In figure 4.4(a), we see that edge modes exist in a real valued gap up until just above $k_{sp}d/\pi = 0.8$ and again in an imaginary valued gap above $k_{sp}d/\pi = 0.96$. In the non-sublattice symmetric case, figure 4.4(b), edge modes disappear as the bulk crosses their path. It is a little difficult to make out where the edge modes disappear due to the projection, but we can check this using the equivalents in figure 4.3(a).

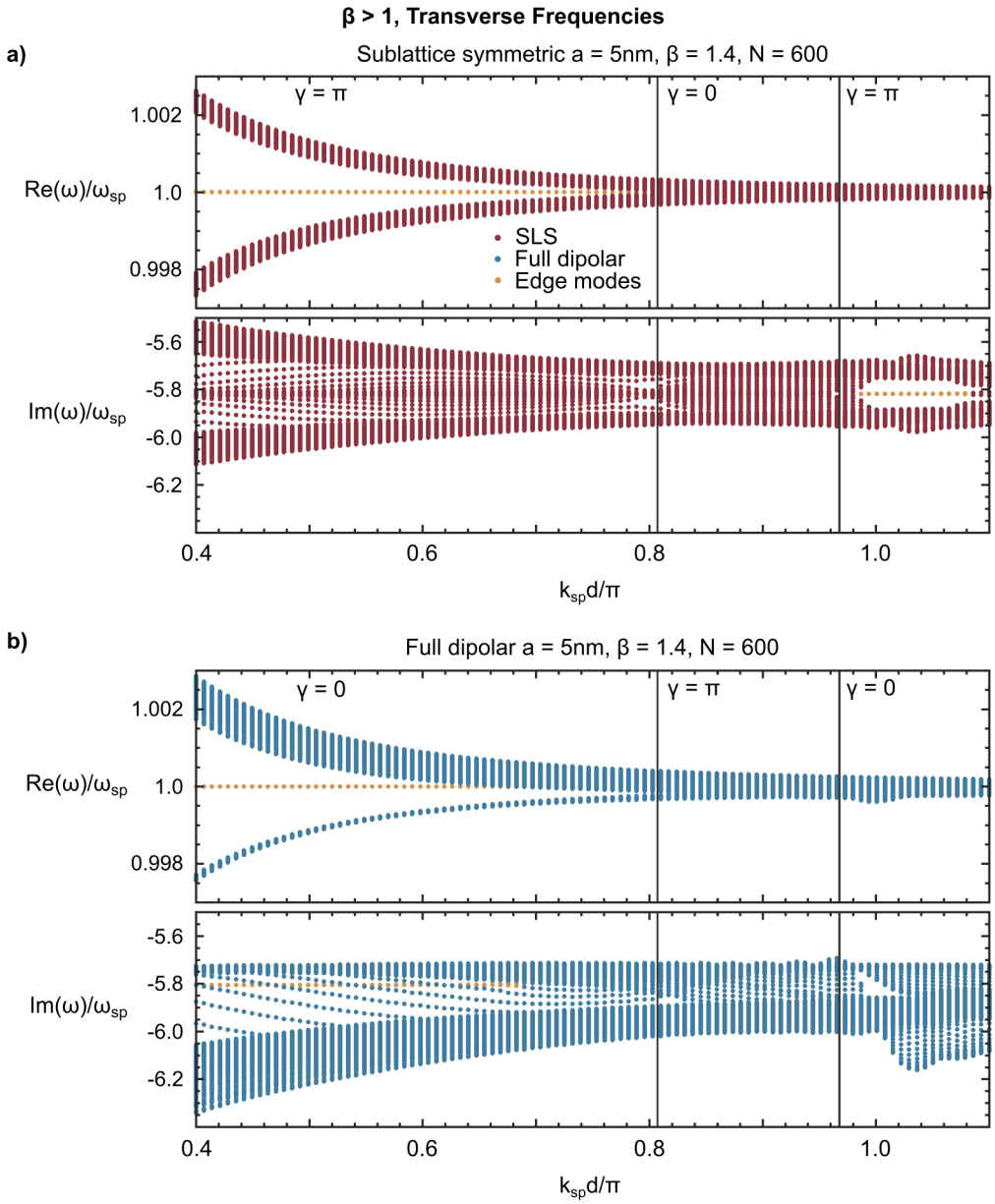

Figure 4.4: Frequencies of the SLS (red) and full dipolar (blue) topological plasmonic chain with changing $k_{sp}d$ for the transverse polarisations. Topologically protected edge modes are yellow. Vertical black lines indicate Zak phase transitions as predicted by the closing of the bulk gap.

4.4 NON-HERMITIAN NNN SSH MODEL

Missing from our current description of BEC breakdown is an understanding of exactly how the A to A and B to B hoppings have to behave to break down the topological protection of the system. In order to better understand the effect that 'trival' SLS breaking has on BEC, we take a slight mathematical diversion to study a much simpler non-Hermitian, next nearest neighbour (NNN), extension to the SSH model. This will aid us when we return to the plasmonic chain afterwards.

We consider an NNN SSH model, much like in a work by Pérez-González *et al.* [127], with the addition of symmetric complex valued hopping, as in figure 4.5(a),

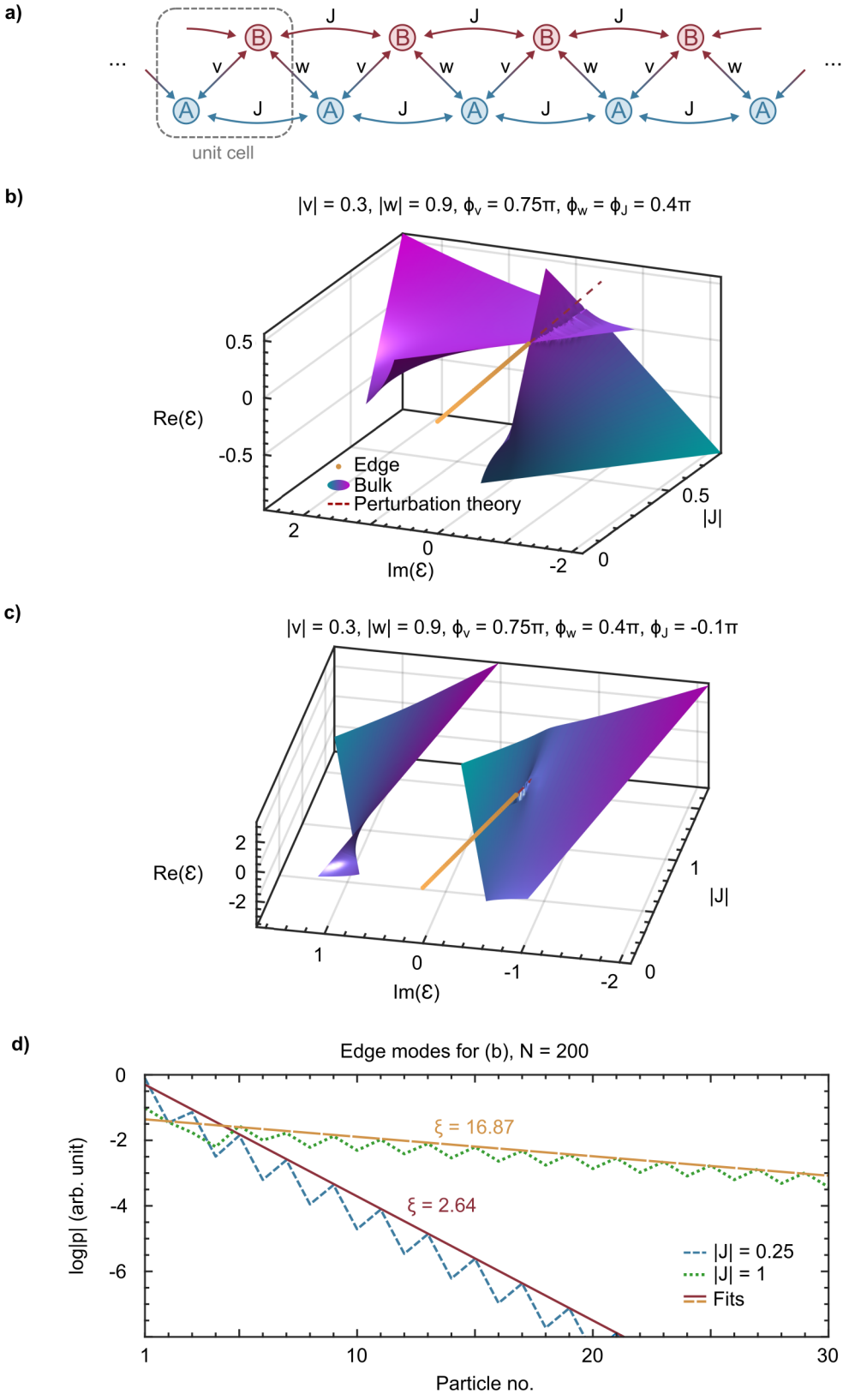

Figure 4.5: (a) Diagram of non-Hermitian NNN SSH model with complex hopping *v*, *w* and J. (b) and (c) Bulk (blue and pink surface) and edge mode (yellow) eigenvalues of the non-Hermitian NNN SSH model for changing values of |J|, for different choices of hopping parameters and phases in (b) and (c). Edge modes with larger |J| values are darker yellow. The red dashed line is given by perturbation theory. (d) Edge mode profiles for the choice of parameters given in (c) for different choices of |J|.

which makes the model non-Hermitian. This is a simplified version of a model studied by Li *et al.* [135]. Intracell hopping is given by $v = |v|e^{i\phi_v}$, intercell hopping by $w = |w|e^{i\phi_w}$, and A to A and B to B hopping by $J = |J|e^{i\phi_J}$. The Hamiltonian is given by

$$\begin{aligned} H = &\sum_{n=1}^{N} v\,[|n, A\rangle\langle n, B| + \text{H.c.}] \\ &+ \sum_{n=1}^{N-1} w\,[|n+1, A\rangle\langle n, B| + \text{H.c.}] \\ &+ \sum_{n=1}^{N-1} J[|n+1, A\rangle\langle n, A| + |n+1, B\rangle\langle n, B| + \text{H.c.}], \end{aligned} \tag{4.11}$$

where H.c. is the Hermitian conjugate. This model has bulk Bloch Hamiltonian

$$\mathcal{H}(q) = \begin{pmatrix} 2J\cos(q) & v + e^{-iq}w \\ v + e^{iq}w & 2J\cos(q) \end{pmatrix}. \tag{4.12}$$

This Hamiltonian has similarities to $\mathcal{G}$ in that it has inversion symmetry and SLS broken by an identity term, in this case proportional to the complex variable J. In fact, the SLS system that this model shares bulk eigenvectors with is exactly the non-Hermitian SSH model studied by Lieu [132]. The system has Zak phase $\gamma = \pi$ ($\gamma = 0$) when $|w| > |v|$ ($|w| < |v|$), with a topological phase transition at $|w| = |v|$.

4.4.1 NNN SSH finite chains

To study the breakdown of BEC in this system we calculate the eigenvalues for $J = 0$ in a finite system, then increase J slowly to see where the edge modes enter the bulk. There is no Zak phase transition with changing J, so the point where the edge modes enter the bulk can be considered the value of J for which BEC breakdown occurs.

Figures 4.5(b) and (c) show the evolution of finite chain eigenvalues $\mathcal{E}$ as $|J|$ increases for chains with $N = 200$ particles with $|v| = 0.3$, $|w| = 0.9$, $\phi_v = 0.75\pi$, $\phi_w = 0.4\pi$ and two different choices of phase for J, $\phi_J = 0.4\pi$ in (b) and $\phi_J = -0.1\pi$ in (c). Bulk modes are discrete values, but for the purposes of display are drawn as continuous surfaces shaded blue to pink, with pink having larger $\text{Re}(\mathcal{E})$. Edge modes are coloured yellow. The figure also features a red dashed line showing the predicted path of the edge modes according to perturbation theory, which we discuss in subsection 4.4.2.

As expected, we see that the edge modes enter the bulk for some value of $|J|$ and then disappear, marking the breakdown of BEC in the system. Figure 4.5(b) shows a choice of parameters where the bulk modes meet and cross the path of the edge modes, while figure 4.5(c) shows the case where the bulk does not close, and instead the edge modes move into one of the bulk bands to destroy BEC.

From these figures, we see that there are the two phenomena that appear to govern the destruction of BEC for long chains: the movement of the bulk, as in (b), and the movement of the edge modes, as in (c). In fact, there is a third case, where the bands

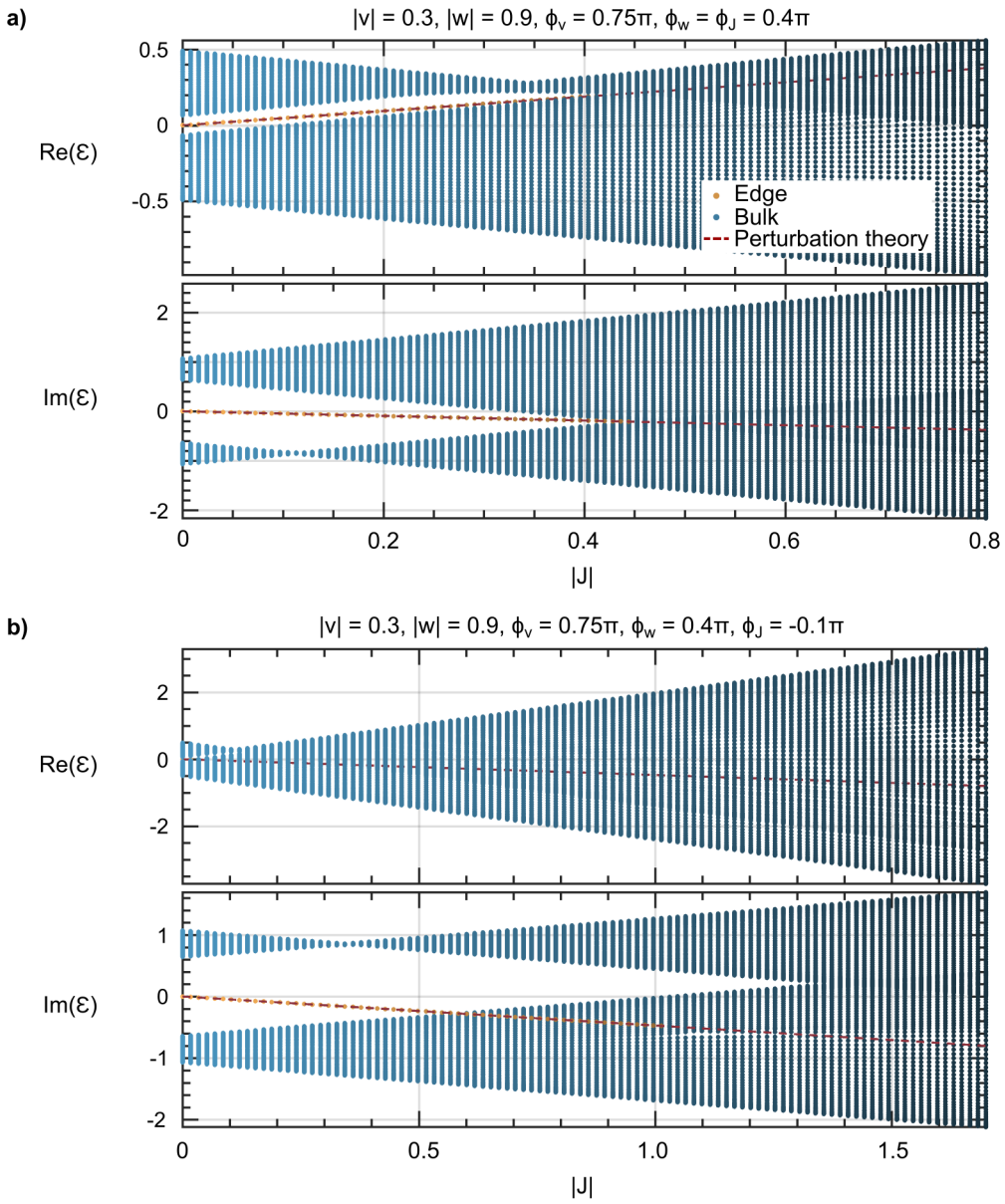

Figure 4.6: Bulk (blue) and edge mode (yellow) eigenvalues of the finite non-Hermitian NNN SSH model for changing values of |J|, for different choices of hopping parameters and phases, with (a) and (b) corresponding to figures 4.5(b) and (c) respectively. Darker coloured modes have larger |J| values.

close due to finite size effects, but we ignore this for now as we cannot quantify it with the bulk Hamiltonian, and its effect can be reduced by increasing the number of particles in the chain. For any set of parameters v, w and J, BEC breakdown is caused by a combination of these effects.

Figure 4.5(d) shows edge modes of figure 4.5(c), for particular choices of |J|. As before, they delocalise as we approach the BEC breakdown, but unlike the plasmonic topological insulator case they are completely exponential, and as |J| increases so does the localisation length ξ, until they are no longer localised.

For completeness, figure 4.6 shows the real and imaginary parts of the eigenvalues for figure 4.5(b) and (c). For the real part in Figure 4.6(b) the bulk obscures the edge

modes, but BEC doesn't break down until the edge modes disappear in the imaginary part plot.

4.4.2 NNN SSH phase diagrams

We have defined BEC breakdown as the first time the edge modes enter the bulk without a change of Zak phase. To understand where this happens in this system, we find a mathematical description for the bulk modes and edge modes. First, we solve the Bloch eigenvalue problem for the bulk Bloch eigenvalues,

$$\mathcal{E}_{bulk} = 2J\cos(q) \pm \sqrt{v^2 + w^2 + 2vw\cos(q)}. \tag{4.13}$$

The finite bulk eigenvalues behave in a similar manner to this, as long as the chain we consider is long enough.

Finding the variation of edge eigenvalues as we change J is a little trickier. Pérez-González *et al.* [127] used linear regression to estimate this in the Hermitian case, where v, w, and J are real, giving

$$\mathcal{E}_{edge} = -2J\frac{v}{w}. \tag{4.14}$$

We use perturbation theory to check the validity of this fit for the non-Hermitian case. We start by considering the model without the NNN terms, resulting in a symmetric, but non-Hermitian, Hamiltonian of the form

$$\begin{aligned} H^0 =& v\sum_{n=1}^{N} [|n, A\rangle\langle n, B| + \text{H.c.}] \\ &+ w\sum_{n=1}^{N-1} [|n+1, A\rangle\langle n, B| + \text{H.c.}]\,. \end{aligned} \tag{4.15}$$

This is the same as setting $J = 0$ in the NNN model. We treat the addition of the SLS breaking hopping terms as a perturbation by an operator $\mathcal{J}$, which features A to A and B to B hopping in the form

$$\mathcal{J} = J\sum_{n=1}^{N-1} [|n+1, A\rangle\langle n, A| + |n+1, B\rangle\langle n, B| + \text{H.c.}]. \tag{4.16}$$

We examine the matrix $H^1 = H^0 + \mathcal{J}$. Now J, which dictates the strength of the NNN hopping, is the small parameter in our perturbation theory. H^0 is symmetric, so its right and left eigenvectors are related simply by

$$H^0\mathbf{v}_n^0 = \mathcal{E}_n^0\mathbf{v}_n^0, \tag{4.17}$$

$$(\mathbf{v}_n^0)^T H^0 = \mathcal{E}_n^0(\mathbf{v}_n^0)^T, \tag{4.18}$$

with the orthogonality condition that $(\mathbf{v}_m^0)^T\mathbf{v}_n^0 = 0$ if $m \neq n$. We are interested in looking at the edge modes, which have $\mathcal{E}^0 = 0$. Working through the usual perturba-

tion theory using the symmetry properties tells us that, to first order, the energy of the perturbed edge modes will be given by

$$\mathcal{E}^1 = \frac{(\mathbf{v}^0)^T \mathcal{J} \mathbf{v}^0}{(\mathbf{v}^0)^T \mathbf{v}^0}. \tag{4.19}$$

As discussed in subsection 2.1.2 and *A Short Course on Topological Insulators* [46], in the thermodynamic limit the left and right edge modes of the unperturbed SSH chain are approximately given by the following:

$$|L\rangle = \sum_{m=1}^{N} a_m |m, A\rangle, \qquad |R\rangle = \sum_{m=1}^{N} b_m |m, B\rangle, \tag{4.20}$$

where a_m and b_m are given by

$$a_m = a_1 \left(\frac{-v}{w}\right)^{m-1} \tag{4.21}$$

$$b_m = b_N \left(\frac{-v}{w}\right)^{N-m} \qquad \forall m \in \{1, \ldots, N\}, \tag{4.22}$$

and a_1 and b_N fix normalisation.

First, we calculate the numerator of equation 4.19

$$|L\rangle^T \mathcal{J} |L\rangle = 2J \sum_{m=1}^{N-1} a_m a_{m+1}, \tag{4.23}$$

and use equation 4.21 to see that

$$|L\rangle^T \mathcal{J} |L\rangle = -2J \frac{v}{w} a_1^2 \sum_{m=1}^{N-1} \left(\frac{v}{w}\right)^{2m-2}. \tag{4.24}$$

Next we calculate the denominator of equation 4.19. For the left eigenvalues this is

$$|L\rangle^T |L\rangle = \sum_{m=1}^{N} a_m^2 \tag{4.25}$$

$$= a_1^2 \sum_{m=1}^{N} \left(\frac{v}{w}\right)^{2m-2}, \tag{4.26}$$

So the energy of the left edge mode, for small NNN hopping, is

$$\mathcal{E}_L = -2J \frac{v}{w} \frac{\sum_{m=1}^{N-1} \left(\frac{v}{w}\right)^{2m-2}}{\sum_{m=1}^{N} \left(\frac{v}{w}\right)^{2m-2}} \tag{4.27}$$

We note that, in the case where the Zak phase is $\gamma = \pi$ and BEC predicts the existence of edge modes, we have $|v/w| < 1$. Therefore, in the thermodynamic limit, $N \to \infty$, the energy of the left edge mode converges to

$$\mathcal{E}_L = -2J \frac{v}{w}, \tag{4.28}$$

as predicted for the Hermitian case by numerical methods [127].

For completeness, we perform the same calculation for the right edge mode. We have, for the numerator,

$$\langle R|^T \mathcal{J} |R\rangle = 2J \sum_{m=1}^{N-1} b_m b_{m+1}, \tag{4.29}$$

which, when combined with equation 4.22, is

$$\langle R|^T \mathcal{J} |R\rangle = 2J b_N^2 \sum_{m=1}^{N-1} \left(\frac{-v}{w}\right)^{2N-2m-1} \tag{4.30}$$

Next, we rearrange the sum by making the substitution $j = N - m$, at which point it becomes clear that the calculation is the same as for the left edge modes,

$$\langle R|^T \mathcal{J} |R\rangle = -2J \frac{v}{w} b_N^2 \sum_{m=1}^{N-1} \left(\frac{v}{w}\right)^{2m-2}. \tag{4.31}$$

For the right edge modes, the denominator of equation 4.19 is given by

$$\begin{aligned} \langle R|^T |R\rangle &= \sum_{m=1}^{N} b_m^2 && (4.32)\\ &= b_N^2 \sum_{m=1}^{N} \left(\frac{v}{w}\right)^{2N-2m} && (4.33)\\ &= b_N^2 \sum_{m=1}^{N} \left(\frac{v}{w}\right)^{2m-2}, && (4.34)\\ & && (4.35) \end{aligned}$$

As with the left eigenmode, the energy for small NNN hopping is given by

$$\mathcal{E}_R = -2J \frac{v}{w} \frac{\sum_{m=1}^{N-1} \left(\frac{v}{w}\right)^{2m-2}}{\sum_{m=1}^{N} \left(\frac{v}{w}\right)^{2m-2}}. \tag{4.36}$$

Again, given that $|v| < |w|$, in the thermodynamic limit, $N \to \infty$, this converges to

$$\mathcal{E}_R = -2J \frac{v}{w}. \tag{4.37}$$

We conclude that both edge modes have the same path in complex space as J, the NNN hopping parameter, changes.

We can use this information to find where the bulk and edge modes first intersect, if finite size effects are negligible, by solving $\mathcal{E}_{edge}(q) = \mathcal{E}_{bulk}(q)$ for $J(q)$. We then plot this value of J for each q in the BZ to construct phase diagrams, as in figure 4.7. Figure 4.7(a) shows the BEC phase diagram for the parameters used in figures 4.5(b) and (c). We can imagine starting with $|J| = 0$ and moving in a straight line in the complex plane by increasing the SLS breaking parameter $|J|$. Then, the direction we move in is dictated by ϕ_J. Eventually the edge modes and bulk meet when we cross the black line, moving from the white region to the green region. Therefore, the white

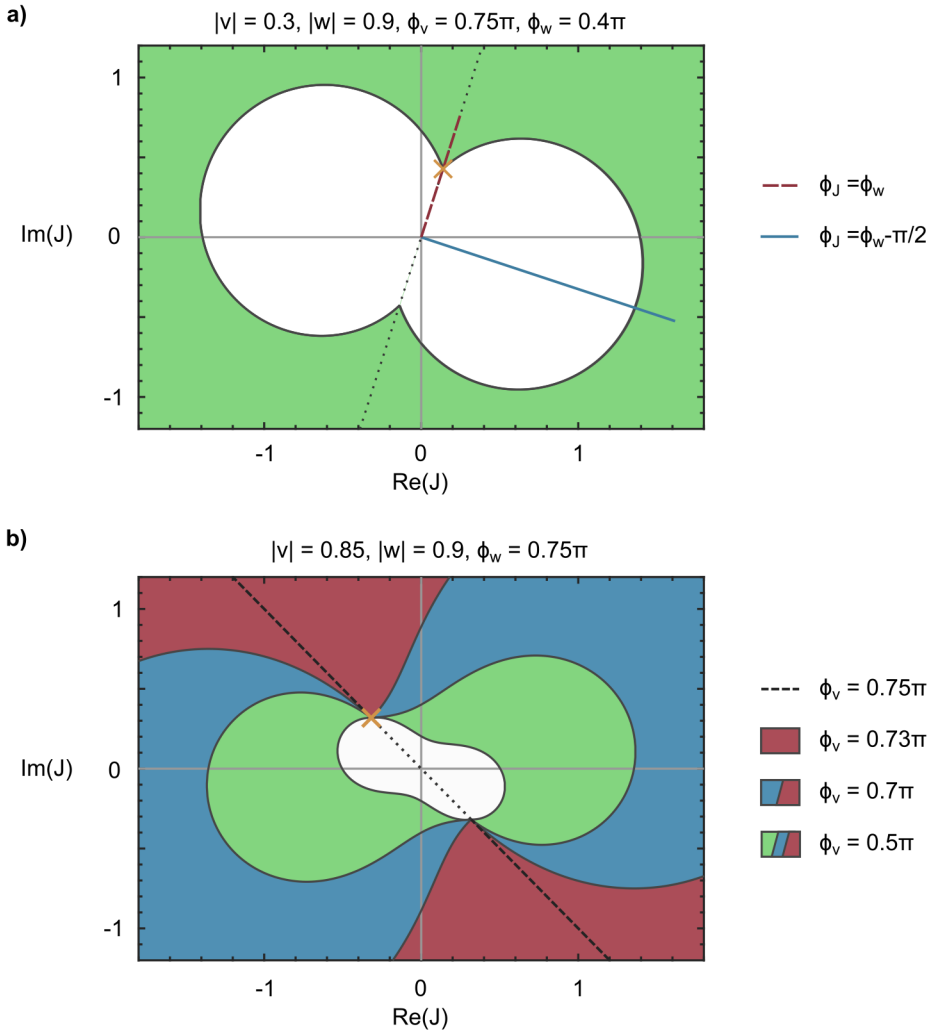

Figure 4.7: (a) BEC phase diagram with predicted region of bulk-edge correspondence (white) and its breakdown (green) for parameters of the chain from fig 4.5, with ϕ_J from fig 4.5(a) (red dashed line) and fig 4.5(b) (blue line), yellow cross at $w/2$ and dotted line along ϕ_w. (b) BEC phase diagrams for $|v| \sim |w|$ and varying ϕ_v. The red, blue and green colours represent different regions where BEC breakdown occurs for different choices of ϕ_v, with red for $\phi_v = 0.73\pi$, red and blue for $\phi_v = 0.7\pi$, and finally all of red, blue and green for $\phi_v = 0.5\pi$

region corresponds to the values of J with BEC and the green region corresponds to values where it is broken. The red dashed and blue solid lines correspond to choices of ϕ_J from figures 4.5(b) and (c) respectively.

We remind ourselves that, in figure 4.5(b), we see the bulk bands shifted directly towards $|\mathcal{E}| = 0$, whereas in figure 4.5(c), they do not move towards $|\mathcal{E}| = 0$, and instead BEC breakdown is caused by the movement of the edge modes into the bulk. The second of these happens at a higher $|J|$ value. This indicates that breakdown occurs for different degrees of SLS breaking, $|J|$, depending on the direction the bands are shifted due to choice of parameter ϕ_J. For $|v| << |w|$, as in figure 4.7(a), the phase corresponding to the smallest $|J|$ at which BEC breakdown occurs is $\phi_J = \phi_w$, and the transition happens at $J = w/2$ (yellow cross). Comparing figures 4.5 and 4.7(a) we see that, when $\phi_J \sim \phi_w$, BEC breakdown is dominated by bulk movement, and when ϕ_J is far from ϕ_w it is dominated by edge movement. In the Hermitian model,

$\phi_J = \phi_w$ always. Non-Hermiticity allows for complex J, and therefore leads to different behaviours depending on the 'path' of the bulk in complex space.

Figure 4.7(b) shows the case where $|v|$ is similar to, but still smaller than, $|w|$ for different values of ϕ_v. The colouring represents different regions where breakdown occurs for different choices of ϕ_v, with red for $\phi_v = 0.73\pi$, red and blue for $\phi_v = 0.7\pi$, and finally all of red, blue, and green for $\phi_v = 0.5\pi$. As ϕ_v gets closer to ϕ_w, the region of BEC becomes larger, until at $\phi_v = \phi_w$ it only appears to break down when $\phi_J = \phi_w$. However, for ϕ_J far from ϕ_w, the breakdown is dominated by finite size effects which shrink the BEC region. In this case, when ϕ_v is not similar to ϕ_w, we also see that the shortest path in J space is not necessarily along ϕ_w.

We briefly summarise the results which will be useful for our study of the plasmonic chain. Increasing A to A and B to B hopping causes both the bulk and edge modes to be shifted in complex space until one collides with the other, at which point BEC breakdown occurs. We have observed a system where, depending on the choices of parameter ϕ_J, either the bulk or edge mode movement acts as the dominant effect. The parameter chooses the direction in which the bands are shifted in complex space, which has a significant effect on exactly how much SLS breaking is required to cause BEC breakdown. This is an important question only in a non-Hermitian system, where eigenvalues are complex, because in a Hermitian system the 'direction parameter' is fixed along the real line.

4.5 BEC BREAKDOWN IN THE PLASMONIC CHAIN

Previous works have discussed the fact that a breakdown in BEC occurs in the transverse case, when the long range term in the Green's function becomes large enough that A to A and B to B hoppings are comparable to A to B and B to A hoppings [181, 182]. In the following, we elaborate on the conditions for BEC breakdown in these systems.

As discussed in the previous section, BEC breakdown can be dominated by the movement of the bulk or of the edge modes, depending on the parameters of a system. Although it is difficult to exactly align parameters of the plasmonic system with parameters from the NNN system, we can see from plots like figure 4.2(b) and 4.3(a) that, in the dipole-dipole system, the edge modes do not move far from $\mathcal{E} = 0$ relative to the size of the bulk values before entering the bulk. Therefore, the movement of the bulk dominates and it is reasonable to approximate $\mathcal{E}_{edge} = 0$.

The bulk bands,

$$\mathcal{E}^{\pm}_{bulk}(q_x) = \mathcal{G}^{11}(q_x) \pm \sqrt{\mathcal{G}^{12}(q_x)\mathcal{G}^{21}(q_x)} \tag{4.38}$$

are given by the off-diagonal terms of the bulk Bloch Hamiltonian equal to the bands of the SLS system, $\pm\sqrt{\mathcal{G}^{12}(q_x)\mathcal{G}^{21}(q_x)}$, plus a shift in complex space, $\mathcal{G}^{11}(q_x)$. In the Hermitian case [127], one of the bands crosses zero when, for some value of q_x in the BZ, the magnitude of the shift $\mathcal{G}^{11}(q_x)$ is equal to that of the SLS bands:

$$\left|\mathcal{G}^{11}(q_x)\right| = \left|\sqrt{\mathcal{G}^{12}(q_x)\mathcal{G}^{21}(q_x)}\right|. \tag{4.39}$$

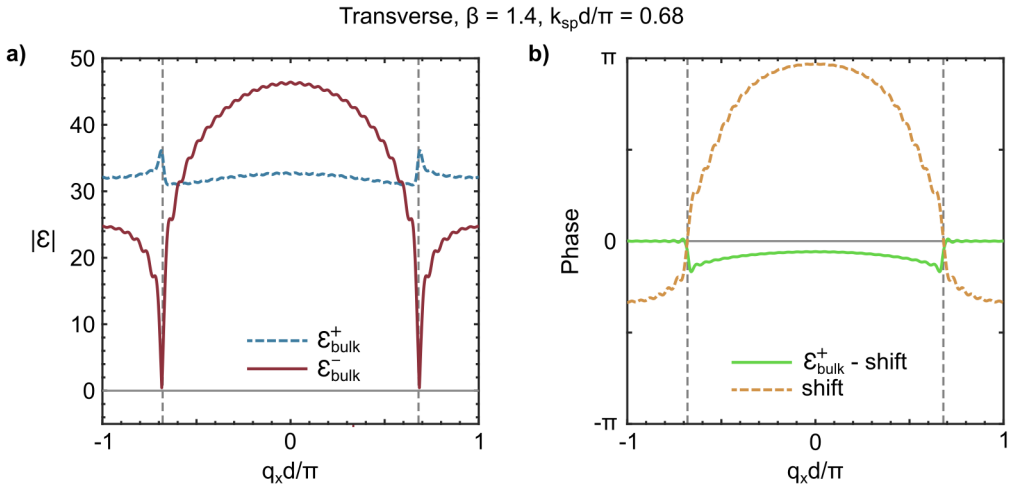

Figure 4.8: Bulk bands at the bulk-edge correspondence breakdown for $\beta = 1.4$. a) $\mathcal{E}$ for the bulk bands (blue dashed and red solid lines), showing that one of the bands approaches $\mathcal{E} = 0$ at the light lines (grey dashed lines). b) The phases of the SLS bands (green solid line) and the shift (yellow dashed line) compared. They cross near the light lines (grey dashed lines).

However, when considering a non-Hermitian system we must be careful because the shift and the SLS bands could have different phases, so that the bulk bands do not necessarily cross zero when this is true.

The plasmonic system's equivalent parameter to the NNN system's ϕ_J is the phase of the shift $\mathcal{G}^{11}$, which differs in that it has $k_{sp}d$ dependence. In much the same way that q_x was the parameter for the breakdown value of J in figure 4.7, we are interested in where in the BZ the bulk bands of the plasmonic system first cross $|\mathcal{E}| = 0$, in order to identify the direction in which the phase of $\mathcal{G}^{11}$ points. From observations of bulk band structures, we see that dips at the light line lead to the zero-line crossing as $k_{sp}d$ increases because these dips give the minimum $|\mathcal{E}|$ for one of the bands. An example of this is depicted in figure 4.8(a) for $\beta = 1.4$ at the BEC breakdown, $k_{sp}d/\pi = 0.68$. In this case $|\mathcal{E}^-_{bulk}|$, the red solid line, touches $|\mathcal{E}| = 0$ at the light lines, given by the grey dashed line. This means that, at the light line, the phases of the shift, $\mathcal{G}^{11}(q_x)$, and the square root part of equation 4.38, $\sqrt{\mathcal{G}^{12}(q_x)\mathcal{G}^{21}(q_x)}$, are approximately equal. This is depicted in figure 4.8(b) for $\beta = 1.4$ at the BEC breakdown, $k_{sp}d/pi = 0.68$. In fact, the phases are close to zero, and outside the light lines the SLS bands are approximately real valued. We will see that SLS bands have this property in other parameter regimes in chapter 5.

These observations tell us that the plasmonic system is in a situation roughly equivalent to the NNN $\phi_J \approx \phi_w \approx \phi_v$ case. The edge mode eigenvalues don't move significantly and, for certain q_x, the bulk bands move towards $|\mathcal{E}| = 0$ as $k_{sp}d$ increases. This means that, for certain q_x, when the shift $\mathcal{G}^{11}(q_x)$ is equal in magnitude to the SLS bands $\sqrt{\mathcal{G}^{12}(q_x)\mathcal{G}^{21}(q_x)}$ we expect the bands to cross $|\mathcal{E}| = 0$. In light of this, we define a measure of SLS breaking for this system,

$$\eta = \max_{q_x \in BZ} \frac{|\mathcal{G}^{11}(q_x)|}{|\sqrt{\mathcal{G}^{12}(q_x)\mathcal{G}^{21}(q_x)}|}. \tag{4.40}$$

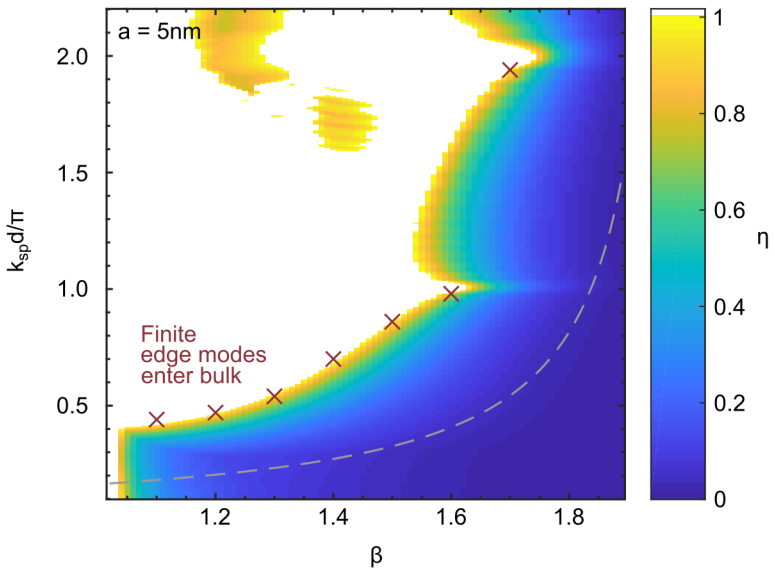

Figure 4.9: η for the transverse modes of the chain, for different β and $k_{sp}d$. The colour saturates so that values of $\eta > 1$ are white. Red crosses correspond to the locations where edge modes first enter the bulk in finite 600 particle chains, possibly indicating the BEC breakdown. The grey dashed line corresponds to the minimum value of $k_{sp}d/\pi$ for which the CDEs are a good approximation.

We plot η in figure 4.9 for changing $k_{sp}d$ versus β, for the transverse modes of the chain, overlaid with red crosses where the edge modes of finite chains of $N = 600$ first appear to enter the bulk. The colour saturates so that white corresponds to regions with $\eta > 1$. The grey dashed line is the minimum value of $k_{sp}d$ for which the CDEs are a good approximation. From the definition, when $\eta = 0$ the system is fully SLS. We consider η by fixing β, starting with small $k_{sp}d$, then increasing to see how the BEC breakdown occurs as we do so. For small $k_{sp}d$, when $\eta < 1$ the bulk cannot have crossed the zero line, so we expect the edge modes to still exist and for the system to have BEC. Approximately when $\eta = 1$, one of the bulk bands touches the zero line and therefore the edge modes have entered the bulk, with some small disagreement due to our aforementioned approximations. Finally, when $\eta > 1$ we expect BEC to have broken down because the edge modes have already entered the bulk. In figure 4.9 we see that $\eta = 1$ at roughly the same $k_{sp}d$ for which BEC breakdown occurs in the finite systems, again shown as red crosses. This supports the notion that η is a good measurement of BEC breaking for the system.

In figure 4.9, we see that, after the lowest values of $k_{sp}d$ such that $\eta > 1$, increasing $k_{sp}d$ sometimes leads to a region where $\eta < 1$, for example the yellow islands surrounded by white. We do not necessarily expect the return of exact BEC, as seen in finite chain simulations like those in figure 4.2(b). However, if η ever returns to $\eta = 0$ then BEC must return because the system must have SLS. This means it is difficult to claim anything certain about these particular cases. For example, in the $\beta = 1.6$ case, modes appear in the gap above $k_{sp}d/\pi = 1$, much like in figure 4.3(a), but it is difficult to ascertain how well protected these modes are.

Peaks at $k_{sp}d/\pi = n$, where n is an integer, seem to be due to the light lines meeting at the edge of the BZ and combining to cross $|\mathcal{E}| = 0$ for lower $k_{sp}d$. Finally,

for the longitudinal case, in this region and all regions examined we find $\eta < 1$, which agrees with the fact that we always expect BEC for the longitudinal polarisation.

From both the bulk measure η and finite systems (red crosses), we observe that for a given value of particle radius, here $a = 5\,\text{nm}$, as the period of the chain increases, BEC breaks down in agreement with our discussion of the breaking of SLS. The measure η is a useful measure of the SLS breaking in the system which can be used as a map for experimentalists to search for parameters of $k_{sp}d$ that can be expected to exhibit BEC. In the figure, $k_{sp}d/\pi = 1$ corresponds to $d = 184\,\text{nm}$, so for example a chain with $\beta = 1.4$ can be expected to retain bulk-edge correspondence up to approximately $d = 120\,\text{nm}$. For larger values of β, the value of the period for which BEC breakdown occurs increases. Hence, it would be experimentally favourable to choose larger values of β and larger periods d to observe topological edge modes in these plasmonic chains because the particles would not need to be very closely spaced, relaxing fabrication constraints. On the other hand, regarding particle size, we expect qualitatively similar results for particles up to 20 nm radius. Here, radiative effects would be more prominent but the topological properties would be qualitatively the same, as we described in subsection 3.2.4. Experimental techniques such as cathodoluminescence spectroscopy and non-linear light generation can be used to probe topological band structures in photonics [189, 190]. We expect the other dipolar systems discussed at the start of this chapter to exhibit similar topological behaviour because they feature the same type of dipole-dipole interactions [181, 182].

Beyond the topological plasmonic chain, individual systems featuring SLS breaking must be examined on a case-by-case basis to understand where BEC breakdown occurs, by considering the behaviour of the edge modes and bulk. As demonstrated by the above study, one can apply some of the knowledge gained from the simple non-Hermitian NNN SSH model to develop a measure for a more complicated system.

4.6 SINGULAR–VALUE DECOMPOSITION SPECTRA

As discussed at the start of this chapter, another method proposed to reconcile BEC in non-Hermitian systems is that of singular-value decomposition (SVD). This section features preliminary results regarding the SVD spectra of the one-dimensional plasmonic chain which have not previously been published.

First, we recall that the eigenvalue decomposition for a square matrix A is given by

$$A = Q\Lambda Q^{-1}, \tag{4.41}$$

where Λ is the diagonal matrix whose entries are the eigenvalues of A, and Q is the matrix whose columns are the corresponding eigenvectors. In the singular-value decomposition, a matrix, B, is written

$$B = USV^{\dagger}, \tag{4.42}$$

where S is a diagonal matrix with non-negative real numbers on the diagonal, called the singular values s of the matrix, and U and V are unitary matrices whose columns are corresponding left and right singular vectors. In general, B is not necessarily square. U and V are not uniquely defined, but up to ordering S and the product $Q = UV^{\dagger}$ are. Singular values can be calculated for a Hamiltonian in a similar way to

eigenvalues. In the Hermitian case, singular values are given by the absolute value of the eigenvalues, but this property breaks down in the case of non-Hermiticity.

Herviou *et al.* showed recently that, in non-Hermitian systems where BEC breakdown occurs due to the non-Hermitian skin effect, the correspondence can be recovered if singular values are considered instead of eigenvalues [122]. Topological protection is instead applied to singular values which exist at zero in a gap in the SVD spectrum.

For our system, we have argued that BEC breakdown is caused by A to A and B to B hoppings breaking the SLS, an effect which can occur in both Hermitian and non-Hermitian systems. In order to illustrate this, we feature plots of the singular values s for the transverse polarisation of the chain with $\beta = 1.4$ and $\beta = 0.6$ in figure 4.10(a) and (b) respectively. Zak phase transitions, still calculated from the eigenvalue decomposition, are marked by vertical black lines. We compare this figure with figure 4.3, which features eigenvalue plots for exactly the same parameters.

In the SLS toy model (red), singular values exist at $s = 0$ where the Zak phase $\gamma = \pi$, and enter the bulk for $\gamma = 0$, confirming a singular-value BEC in this case. In figure 4.3(b), we see that just above the phase transition to $\gamma = \pi$ at $k_{sp}d/\pi = 0.81$ (2s.f.) the edge modes reach zero at $k_{sp}d/\pi = 0.85$ (2s.f.), whereas the singular value modes reach zero at $k_{sp}d/\pi = 0.82$ (2s.f.). Therefore the SVD agrees with the calculated Zak phase better than the eigenvalues, suggesting that the disagreement in the SLS part of figure 4.3(b) may be due to the non-Hermitian skin effect, and that this issue could be resolved by the SVD approach.

In the full dipolar model (blue), for low $k_{sp}d/\pi$ there are singular values at $s = 0$ for $\beta = 1.4$ in figure 4.10(a) and no zero singular values for $\beta = 0.6$, indicating the existence of BEC. At $k_{sp}d/\pi = 0.68$ (2s.f.) the zero mode joins the bulk for $\beta = 1.4$, and no zero mode occurs for $\beta = 0.6$, indicating that this is not a topological phase transition but most likely a breakdown in BEC. The $k_{sp}d$ value for which this is predicted closely agrees with the occurrence of BEC breakdown for eigenvalues in figure 4.3. From these preliminary results, the SVD doesn't appear to fix the problem of BEC breakdown in this system. This is not too surprising for the reason we have argued throughout this chapter; the breakdown of BEC is due to SLS breaking rather than non-Hermiticity.

Above $k_{sp}d/\pi = 0.68$ (2s.f.), a mode exists separate from the bulk in figure 4.10(a) which is reminiscent of a mode which exists separate from the bulk in figure 4.3(a) and also figure 4.2(b). These are not zero modes, but their presence seems to be linked loosely to the Zak phase. There is even a mode which is separate from the bulk in figure 4.10(b) that is possibly related to the Zak phase, which does not appear in the eigenvalue case in figure 4.3(b). Since these modes are far from zero they are perhaps related to the notion that even though the system has undergone BEC there is still a sliding scale of how badly breakdown has occurred.

These early results have not addressed the question of calculating a topological number using the SVD or the possibility of using the SVD to create a new measure of SLS breaking, in a similar manner to η defined in the previous section. There is also potentially interesting information to be gleaned by studying the singular vectors in matrices to U and V, or applying the idea of entanglement spectra, as discussed by Herviou *et al.* [122].

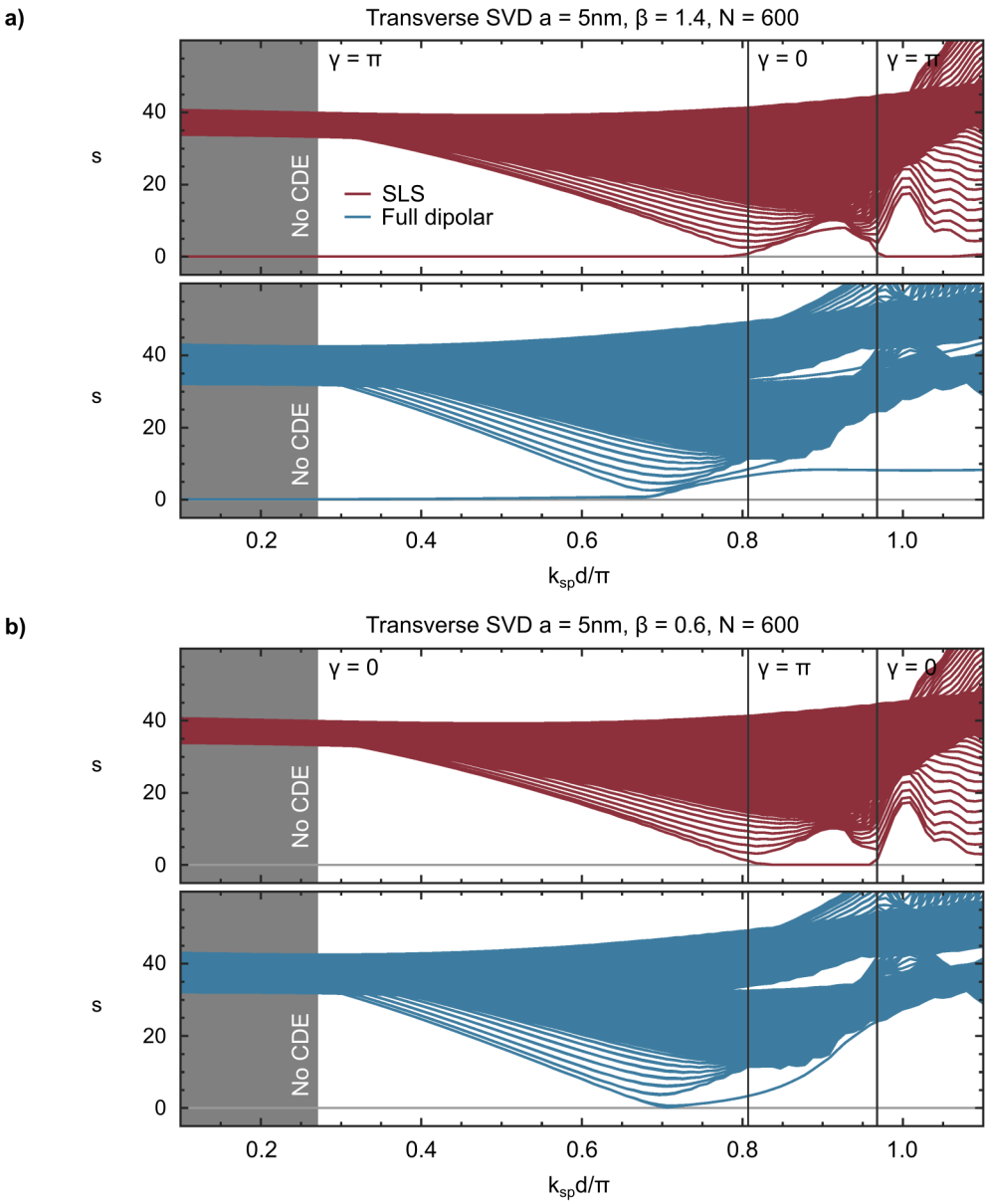

Figure 4.10: Singular values of the SLS (red) and full dipolar (blue) topological plasmonic chains with changing $k_{sp}d$ for the transverse polarisation with (a) $\beta = 1.4$ and (b) $\beta = 0.6$. The dark grey area indicates the region where the CDEs are not valid as the particles are too closely spaced. Vertical black lines indicate Zak phase transitions according to bulk eigenvalue calculations.

4.7 SUMMARY

In this chapter, we have broadened the discussion of BEC in non-Hermitian systems, elaborating on the question of what happens when SLS is broken in 1d systems. We have shown that the question of how strictly SLS must be obeyed in order to observe topological protection is an important one if we wish to be careful about real world topological insulators like the topological plasmonic chain.

We recalled the model for a chain of metallic nanoparticles with alternating spacing and discussed how such a chain has been shown to exhibit topological properties, such as a quantised Zak phase and topological protection of edge modes. Photonic

systems, like the plasmonic chain, are natural non-Hermitian systems and can provide a valuable tool for theoretical and experimental exploration of topological insulators. The chain was shown to exhibit a breakdown of BEC in the transverse-polarised case for large spacing.

We examined the non-Hermitian NNN SSH model to provide some basic intuition for the phenomenon of BEC breakdown, which is shown to be caused by the movement of the bulk, the edge modes, and finite size effects, the first two of which could be visualised with phase diagrams. This informed our study of the plasmonic chain, where we defined a measure of SLS breaking η to find a parameter regime for experimentalists to search for topologically protected transverse edge modes in the system.

Beyond the models considered in this chapter, we have provided a framework for assessing the breakdown of BEC in systems where the movement of the bulk dominates and is directed towards zero in eigenspace, or the bulk and edge modes move predictably.

One of the key messages of this chapter is that the transverse polarisation of the chain does not have BEC above a certain $k_{sp}d$ threshold. However, there is some evidence that inversion symmetric systems with non-trivial topological numbers can be interesting, even in the absence of edge modes. In the next chapter, we briefly touch on some of these ideas and present preliminary studies on the retardation-induced phase transitions featured in the transverse-polarised case.

5 TOPOLOGICAL PHASES OF THE LONG RANGE DIPOLAR CHAIN

Although the transverse polarisation of the staggered chain of metallic nanoparticles breaks SLS, it is still in possession of inversion symmetry. We discussed, in section 3.2, this inversion symmetry could be thought of as quantising the Zak phase of the system, although it does not lead to protected midgap edge modes.

Hughes *et al.* have indicated that inversion symmetric systems instead feature topological protection of their entanglement spectra [187]. In addition, Bello *et al.* reported interesting phenomena when quantum emitters coupled to a different photonic analogue of the SSH model [188]. Importantly, they found that the topological phases of the system affected the quantum emitters even in the case of an infinite system, where no edge modes could exist.

These examples serve to suggest that the topological phases of an inversion symmetric system might have real and measurable consequences in spite of a lack of BEC. This provides some motivation for the study of the topological phases of the transverse polarisation.

In addition to this, probably the largest motivation is simple curiosity. A large portion of the 1d TI models referenced in this thesis do not correspond to some realistic physical system. This doesn't change the fact that many have provided incredible insight in the field of non-Hermitian TIs.

The purpose of this short chapter is to cover some preliminary and unpublished results on the retardation-induced phase transitions of the transverse polarisation of the staggered dipole-dipole system. We introduce the idea of a minimal model for the system, which approximates the same topological phases but simplifies the maths. We construct a phase diagram using the minimal model concept, and present some early results on the properties of the bulk band structures of this model. Due to the early nature of this work, this chapter is a little more technical and unrefined than previous chapters.

5.1 MINIMAL MODEL

We are interested in the retardation-induced phase transitions, which are inherently non-Hermitian and unique to the transverse polarisation of the chain. We start with the linearised transverse-polarised Green's function dipolar model in the previous chapter, except without a cutoff for decoherence of the plasmons, taking hopping to be truly infinite. We then make two simplifying assumptions.

First, we remember that the full dipolar model and the SLS model in the previous chapter have identical topological phases due to their common eigenvectors. This is discussed in some detail in chapters 3 and 4. Second, we note that, for larger values of $k_{sp}d$, the long range term in the Green's function dominates. For these reasons, we would expect an SLS model with only the long range term to have very similar Zak phase properties to the full dipolar system.

To check this, we consider the transverse off diagonal reduced Green's function in equation 4.9. If we take the infinite sum, as opposed to the cut off introduced in section 4.2, we can write the expression in terms of Lerch transcendents as follows,

$$\begin{aligned}\sum_{n\in\mathbb{Z}} \tilde{g}(n\pm\beta/2)e^{iq_x dn} = -\frac{1}{4\pi\epsilon_0}\Bigg\{ & e^{ik_{sp}d\beta/2}\Phi\left(e^{i(k_{sp}d\pm q_x d)},3,\frac{\beta}{2}\right)\\ & + e^{-ik_{sp}d\beta/2}e^{i(k_{sp}d\mp q_x d)}\Phi\left(e^{i(k_s p d\mp q_x d)},3,1-\frac{\beta}{2}\right)\\ & - ik_{sp}d\Bigg[e^{ik_{sp}d\beta/2}\Phi\left(e^{i(k_{sp}d\pm q_x d)},2,\frac{\beta}{2}\right)\\ & + e^{-ik_{sp}d\beta/2}e^{i(k_{sp}d\mp q_x d)}\Phi\left(e^{i(k_{sp}d\mp q_x d)},2,1-\frac{\beta}{2}\right)\Bigg]\\ & - (k_{sp}d)^2\Bigg[e^{ik_{sp}d\beta/2}\Phi\left(e^{i(k_{sp}d\pm q_x d)},1,\frac{\beta}{2}\right)\\ & + e^{-ik_{sp}d\beta/2}e^{i(k_{sp}d\mp q_x d)}\Phi\left(e^{i(k_{sp}d\mp q_x d)},1,1-\frac{\beta}{2}\right)\Bigg]\Bigg\}.\end{aligned} \tag{5.1}$$

How do the short and medium range terms behave compared to the long range term? We can find some simple bounds by starting with the expression for the absolute value of the Lerch transcendent,

$$|\Phi(z,s,\nu)| = \left|\sum_{n=0}^{\infty}\frac{z^n}{(n+\nu)^s}\right|. \tag{5.2}$$

We then use the fact that we always have $|z|=1$ and apply the triangle inequality to get

$$|\Phi(z,s,\nu)| \leqslant \sum_{n=0}^{\infty}\frac{1}{(n+\nu)^s}. \tag{5.3}$$

Given that we require $0<\nu<1$,

$$|\Phi(z,s,\nu)| < \frac{1}{\nu^s}+\sum_{n=1}^{\infty}\frac{1}{n^s} = \frac{1}{\nu}+\zeta(s), \tag{5.4}$$

where $\zeta(s)$ is the Riemann zeta function. Evaluating this at $s=2$ for the medium range term and $s=3$ for the short range term, we have

$$\begin{aligned}|\Phi(z,2,\nu)| &< \frac{1}{\nu^2}+\frac{\pi^2}{6} \approx \frac{1}{\nu^2}+1.645,\\ |\Phi(z,3,\nu)| &< \frac{1}{\nu^3}+\zeta(3) \approx \frac{1}{\nu^3}+1.202.\end{aligned} \tag{5.5}$$

Of course, when $s=1$ there is no such upper bound because the sum diverges at the light line. Again, these inequalities are only true because $|z|=1$ and $0<\nu<1$.

These are not particularly good upper bounds but they have the benefit of being independent of z. Each of the short and medium range terms are a sum of two Lerch

transcendents, so we can apply the triangle inequality once more to find an upper bound for each term. These upper bounds both diverge at $\beta = 0$ and $\beta = 2$ because of the $1/\nu^s$ term, indicating that the short and medium range terms diverge at these values of β at the light line, where $z = 1$. However, so does the long range term. Overall, this indicates that, as long as $0 < \beta < 2$ and $k_{sp}d \gg 1$, we can make a rough statement that a model with only the long range term will have phases transitions located at approximately the same positions as the full dipolar model.

Based on this information, we define a minimal model with bulk Bloch Hamiltonian,

$$\mathcal{M}(q_x) = \begin{pmatrix} 0 & \sum_{n\in\mathbb{Z}} M(n+\beta/2)e^{iq_x dn} \\ \sum_{n\in\mathbb{Z}} M(n-\beta/2)e^{iq_x dn} & 0 \end{pmatrix}, \tag{5.6}$$

where M is proportional to the long range component of the reduced Green's function in equation 4.7, and is given by

$$M(\bar{r}) = \frac{e^{ik_{sp}d|\bar{r}|}}{|\bar{r}|}. \tag{5.7}$$

As in the case of equation 4.7, $\bar{r}$ is a dimensionless number equal to the distance between particles divided by the unit cell length, d.

The purpose of this minimal model is to provide the simplest possible system which features similar topological phase properties to the transverse polarisation of the full dipolar model for the plasmonic chain. The fact that M is proportional, rather than exactly equal, to the reduced Green's function is unimportant for Zak phase properties. The prefactors can be thought of as absorbed into the eigenvalues of $\mathcal{M}(q_x)$, which are given by

$$\mathcal{E}_\pm(q_x) = \pm\left[\sum_{n\in\mathbb{Z}} M(n+\beta/2)e^{iq_x dn}\sum_{m\in\mathbb{Z}} M(m-\beta/2)e^{iq_x dm}\right]^{1/2}. \tag{5.8}$$

The bulk bands represented by $\mathcal{E}_+$ and $\mathcal{E}_-$ are $\pm$ pairs due to SLS, and the bands are also symmetric in q_x due to inversion symmetry. This is discussed in some detail in section 2.1.

Finally, we note that the components of the matrix $\mathcal{M}(q_x)$ can be written in terms of the Lerch transcendent as follows,

$$\begin{aligned}\sum_{n\in\mathbb{Z}} M(n\pm\beta/2)e^{iq_x dn} &= e^{ik_{sp}d\beta/2}\Phi(e^{i(k_{sp}d\pm q_x d)},1,\beta/2) \\ &\quad + e^{-ik_{sp}d\beta/2}e^{i(k_{sp}d\mp q_x d)}\Phi(e^{i(k_{sp}d\mp q_x d)},1,1-\beta/2).\end{aligned} \tag{5.9}$$

5.2 PHASE DIAGRAM

Phase transitions occur when the bulk band gap is zero. This happens when, for some β, q_x and $k_{sp}d$, the eigenvalues given by equation 5.8 are zero. In this section we construct a phase diagram for the minimal model using this information.

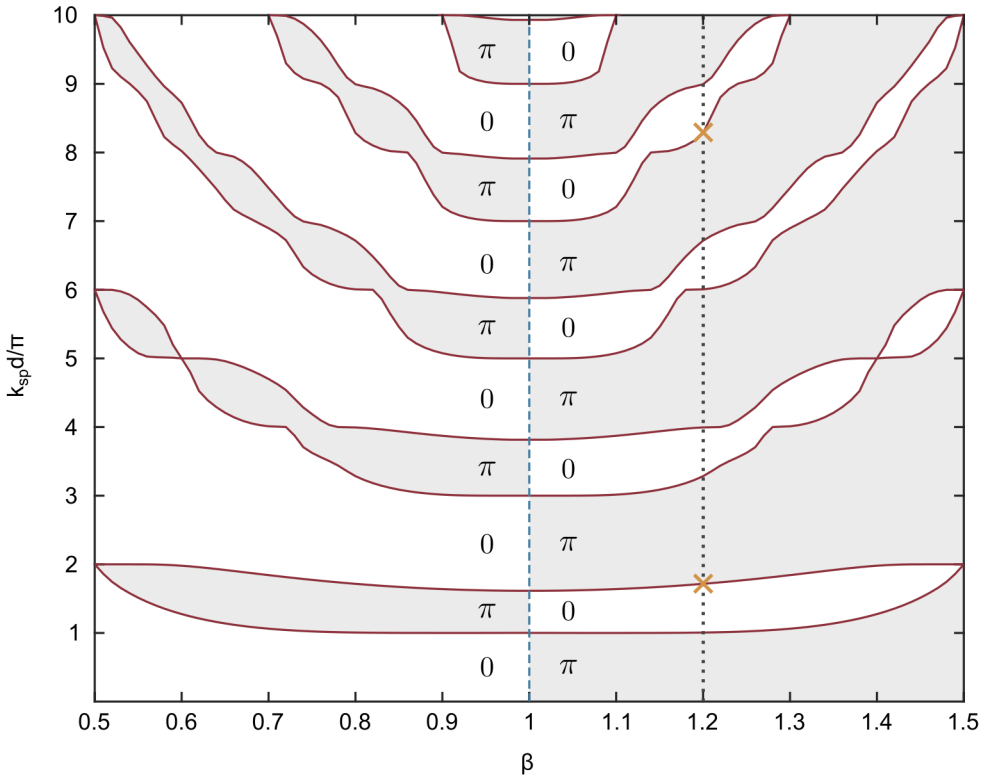

Figure 5.1: Phase diagram for the minimal model up to $k_{sp}d/\pi = 10$. The blue dashed line is the $\beta = 1$ phase transition and the red solid line are retardation-induced phase transitions. Regions with Zak phase $\gamma = \pi$ are coloured grey, and regions with Zak phase $\gamma = 0$ are white.

First we note that a phase transition occurs at $\beta = 1$, $q_x d = \pm\pi$ for all $k_{sp}d$. It is simple to see this using equation 5.9. This is the typical SSH model phase transition that occurs also for the longitudinal polarisation of the full dipolar model.

We are interested in the retardation-induced phase transitions first presented in chapter 3 and discussed in more detail in chapter 4. To find these we fix some $\beta \neq 1$ and use a zero solver to search for points where the eigenvalues are zero. The bulk eigenvalues are symmetric around $\beta = 1$, so we can restrict to only searching for $\beta < 1$ and use the symmetry to find zeros for $\beta > 1$. In addition, inversion symmetry gives $\mathcal{E}(q_x) = \mathcal{E}(-q_x)$, so we only need to search one half of the Brillouin Zone (BZ) for zeros. One can confirm that these zeros are indeed phase transitions by looking at the finite chain and examining the existence or non-existence of edge modes, because we have already shown in chapter 4 that the SLS system has good BEC.

The results, up to $k_{sp}d/\pi = 10$, are presented in the phase diagram in figure 5.1. The blue dashed line is the $\beta = 1$ phase transition and the red solid line represents retardation-induced phase transitions. Grey regions represent parameters with Zak phase π and white regions represent parameters with Zak phase 0. We observe that retardation-induced phase transitions are rarer as β is further from one, likely because the gap relating to the $\beta = 1$ phase transition becomes larger as β moves further from one, so that large enough long range terms to close the gap become rarer. There also appears to be a link between phase transitions and integer values of $k_{sp}d/\pi$, with lots of plateaus in β occurring at near integer values.

In addition to the numerics, we can use equations 5.8 and 5.9 to find some patterns in the phase diagram. Due to the exponentials outside of the Lerch transcendent in equation 5.9, when $k_{sp}d\beta/2$ and $k_{sp}d(1-\beta/2)$ are equal modulo 2π, the eigenvalues begin to repeat. For example, when $\beta = 1.2$ the eigenvalues have a $k_{sp}d$ periodicity of 10π. When $\beta = 1.4$ the eigenvalues have a $k_{sp}d$ periodicity of 20π. This periodic pattern to the eigenvalues in $k_{sp}d$ exists for all rational β, but does not exist at all for irrational β.

The Lerch transcendent also has the following property,

$$\Phi(z^*, s^*, \nu^*) = \Phi(z, s, \nu)^*, \tag{5.10}$$

where * represents complex conjugation. This can be used to show that the eigenvalues are also symmetric in $k_{sp}d = 0$. Because the eigenvalues are periodic for rational β, they are symmetric in the periodicity. For example, the vertical dotted line in figure 5.1 shows a cut for $\beta = 1.2$. A yellow cross marks where a phase transition occurs at $k_{sp}d = 1.72\pi$, indicating another transition at $k_{sp}d = 10\pi - 1.72\pi = 8.28\pi$, also indicated by a yellow cross. Both of these transitions are confirmed using the numerical zero solver.

In the case of a retardation-induced phase transition, there are critical parameters q_x^c, $(k_{sp}d)^c$ and $\beta^c \neq 1$ where the gap is closed, and only one of the off diagonals is zero. For example,

$$\mathcal{M}(q_x^c) = \sum_{n\in\mathbb{Z}} M(n+\beta^c/2)e^{iq_x^c dn}\begin{pmatrix}0 & 1\\ 0 & 0\end{pmatrix}. \tag{5.11}$$

Since the system is inversion symmetric we have a closing of the gap for $\beta = |2-\beta^c|$ at $q_x = -q_x^c$, where the Hamiltonian becomes

$$\mathcal{M}(q_x^c) = \sum_{n\in\mathbb{Z}} M(n-\beta^c/2)e^{iq_x^c dn}\begin{pmatrix}0 & 0\\ 1 & 0\end{pmatrix}. \tag{5.12}$$

In these cases the Hamiltonian becomes defective and has only one eigenvector. Exceptional points are a strictly non-Hermitian property, meaning these retardation-induced phase transitions are a consequence of non-Hermiticity of the system. The full dipolar model has the same behaviour for its exceptional points.

5.3 BULK BANDS AT PHASE TRANSITIONS

In this section we make some additional observations about the bulk bands in the minimal model at phase transitions. First we study band behaviour at the $\beta = 1$ phase transition.

5.3.1 Equispaced chains

First we examine band structures equivalent to an equispaced chain, when $\beta = 1$. Figure 5.2 shows the real and imaginary part of eigenvalues $\mathcal{E}$ for some $\beta = 1$ minimal model band structures. From these figures it is apparent that the real part closes at

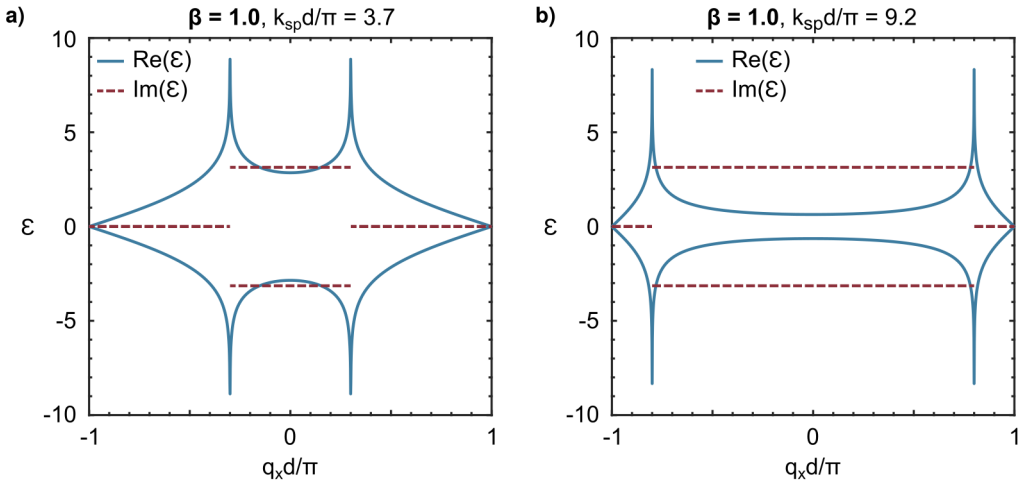

Figure 5.2: Minimal model bulk band structures for $\beta = 1$ with real (blue) and imaginary (red dashed) parts for a) $k_{sp}d/\pi = 3.7$ and b) $k_{sp}d/\pi = 9.2$.

$q_x d = \pm\pi$ as expected. The imaginary part is zero for a region and $\pm\pi$ for another region. This discontinuity in the imaginary part occurs at the light lines.

How might we understand this behaviour? First note that the Maclaurin series for arctanh is

$$\operatorname{arctanh}(z) = \sum_{n=1}^{\infty} \frac{z^{2n-1}}{2n-1}. \tag{5.13}$$

If we compare this to the sum defining the Lerch transcendent,

$$\Phi(z, s, \nu) := \sum_{k=0}^{\infty} \frac{z^k}{(k+\nu)^s}, \tag{5.14}$$

we see that we have the relation

$$\Phi(e^{ix}, 1, 1/2) = 2e^{-ix/2} \operatorname{arctanh}(e^{ix/2}). \tag{5.15}$$

We substitute $\beta = 1$ into equation 5.8, square and expand the brackets. Then we convert to arctanh using equation 5.15, and take the square root. We find that the eigenvalues at $\beta = 1$ are given by

$$\mathcal{E}(k_{sp}, q_x) = \pm 2 \left[\operatorname{arctanh}\left(e^{i(k_{sp}d + q_x d)/2}\right) + \operatorname{arctanh}\left(e^{i(k_{sp}d - q_x d)/2}\right) \right]. \tag{5.16}$$

There are two branch cuts for arctanh in the complex plane, at $(-\infty, -1]$ and $[1, \infty)$. In the above equation we are confined to the unit circle in the complex plane, crossing the point -1 when the arguments of the exponentials are $(2n-1)\pi i$ and the point 1 when the arguments are $2n\pi i$.

It turns out that on the upper unit semicircle the imaginary part of arctanh is $\pi/4$, and on the lower unit semicircle it is $-\pi/4$. We can see how there will be regions of $q_x d$ where the imaginary part of the two arctanh terms in the eigenvalue equation will cancel out. In fact, for $2\pi(n-1) + k_{sp}d < q_x d < 2\pi n - k_{sp}d$, the imaginary

part of the eigenvalues is zero. Notably the limits of this inequality correspond to the light lines. Outside of this region the imaginary parts add up and give $\pm\pi$.

Written in terms of the arctanh expansion, the minimal model Hamiltonian is given by,

$$\mathcal{M}_{\beta=1}(q_x) = \begin{pmatrix} 0 & e^{-iq_x d/2}A \\ e^{iq_x d/2}A & 0 \end{pmatrix}, \tag{5.17}$$

where

$$A = 2\left[\operatorname{arctanh}\left(e^{i(k_{sp}d+q_x d)/2}\right) + \operatorname{arctanh}\left(e^{i(k_{sp}d-q_x d)/2}\right)\right]. \tag{5.18}$$

For $2\pi(n-1)+k_{sp}d < q_x d < 2\pi n - k_{sp}d$, we have A is real, and therefore $\mathcal{M}_{\beta=1} = \mathcal{M}^{\dagger}_{\beta=1}$. The Hamiltonian is Hermitian for these specific q_x values.

Outside of these q_x values the Hamiltonian can be written,

$$\mathcal{M}_{\beta=1}(q_x) = \begin{pmatrix} 0 & e^{-iq_x d/2}[\mathrm{Re}(A) \pm i\pi] \\ e^{iq_x d/2}[\mathrm{Re}(A) \pm i\pi] & 0 \end{pmatrix}. \tag{5.19}$$

5.3.2 Nearly equispaced chains

We can use this arctanh representation and perturbation theory to study small deviations from $\beta = 1$. We write $\beta = 1 + 2\Delta\beta$ and find that

$$\Phi(z, 1, 1/2+\Delta\beta) = \sum_{n=0}^{\infty} (-\Delta\beta)^n \Phi(z, n, 1/2), \tag{5.20}$$

Referring back to equation 5.9 we can expand the Lerch transcendents around $\beta = 1$ as follows,

$$\begin{aligned}\sum_{n\in\mathbb{Z}} \frac{e^{ik_{sp}d|n+\beta/2|\pm iq_x dn}}{|n+\beta/2|} &= e^{ik_{sp}d/2}e^{ik_{sp}d\Delta\beta}\Phi(e^{i(k_{sp}d\pm q_x d)}, 1, 1/2) \\ &+ e^{-ik_{sp}d/2}e^{-ik_{sp}d\Delta\beta}e^{i(k_{sp}d\mp q_x d)}\Phi(e^{i(k_{sp}d\mp q_x d)}, 1, 1/2) \\ &- \Delta\beta\Big[e^{ik_{sp}d/2}e^{ik_{sp}d\Delta\beta}\Phi(e^{i(k_{sp}d\pm q_x d)}, 2, 1/2) \\ &- e^{-ik_{sp}d/2}e^{-ik_{sp}d\Delta\beta}e^{i(k_{sp}d\mp q_x d)}\Phi(e^{i(k_{sp}d\mp q_x d)}, 2, 1/2)\Big] \\ &+ \mathcal{O}(\Delta\beta^2).\end{aligned} \tag{5.21}$$

We didn't expand the exponential function $\exp(ik_{sp}d\beta)$, so even the term which features the $n = 0$ term in the expansion of the Lerch transcendents has some $\Delta\beta$ dependence. Using equation 5.15 we examine this 'zero order' Hamiltonian first. We have

$$\mathcal{M}^0(q_x) = \begin{pmatrix} 0 & e^{-iq_x d/2}A^0_- \\ e^{iq_x d/2}A^0_+ & 0 \end{pmatrix}, \tag{5.22}$$

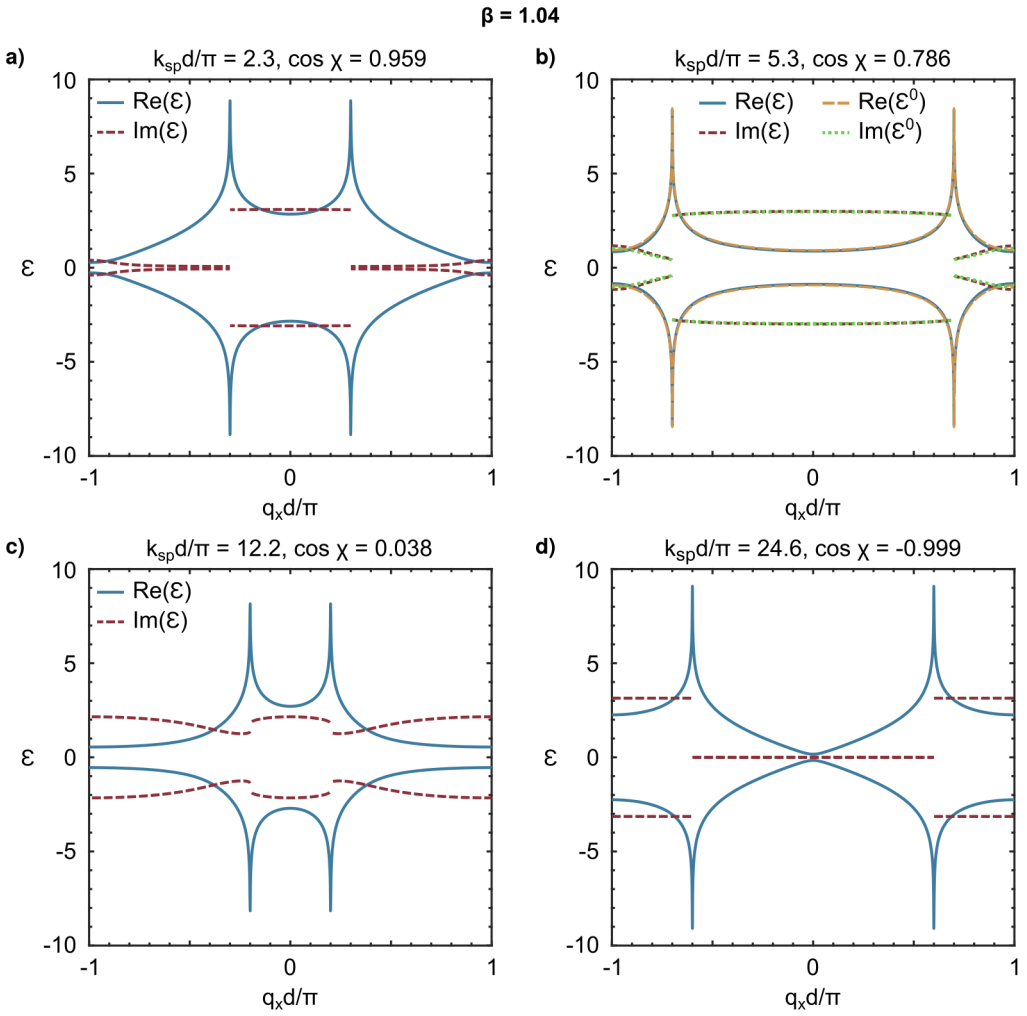

Figure 5.3: Minimal model bulk band structures for $\beta = 1.04$ with real (blue) and imaginary (red dashed) parts for a) $k_{sp}d/\pi = 2.3$, b) $k_{sp}d/\pi = 5.3$, c) $k_{sp}d/\pi = 12.2$ and d) $k_{sp}d/\pi = 24.6$. b) includes the 0^{th} order approximation of the eigenvalues in yellow dashed lines, for real parts and green dotted lines for imaginary parts.

where

$$A^0_\pm = 2\Big[e^{\mp i k_{sp} d \Delta\beta} \operatorname{arctanh}\left(e^{i(k_{sp}d + q_x d)/2}\right) + e^{\pm i k_{sp} d \Delta\beta} \operatorname{arctanh}\left(e^{i(k_{sp}d - q_x d)/2}\right)\Big]. \tag{5.23}$$

This is very similar to the $\beta = 1$ case in equation 5.18 except for the addition of complex prefactors for the arctanh terms which break the the q_x specific Hermiticity of the $\beta = 1$ matrix. However, for certain values of $k_{sp}d$ similar properties are recovered. If $k_{sp}d\Delta\beta = \pi n$, the matrix becomes Hermitian for $2\pi(n-1) + k_{sp}d < q_x d < 2\pi n - k_{sp}d$, exactly like the $\beta = 1$ case. When $k_{sp}d\Delta\beta = \pi(n + 1/2)$, the matrix becomes Hermitian for the opposite region, $2\pi(n-1) - k_{sp}d < q_x d < 2\pi n + k_{sp}d$, a property not seen in the $\beta = 1$ case.

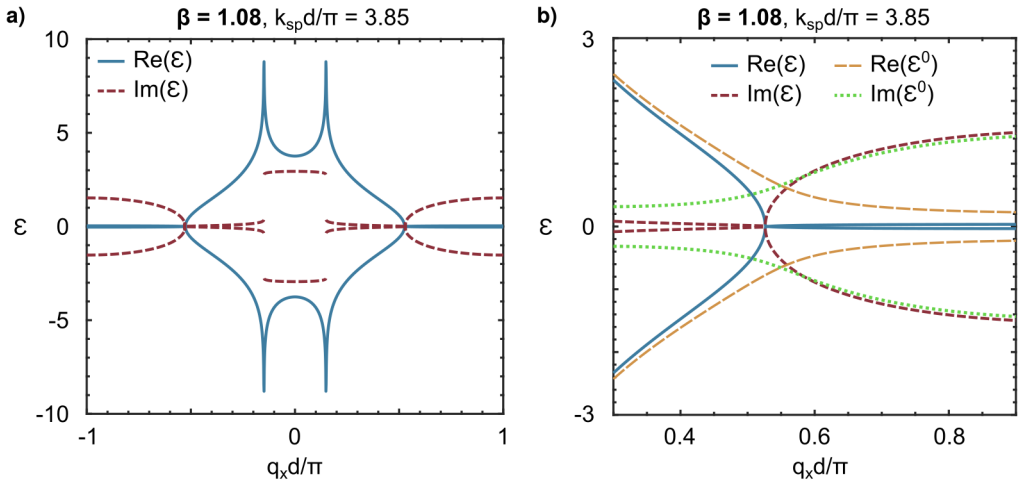

Figure 5.4: a) Minimal model bands for $\beta = 1.08$ at a retardation-induced phase transition $k_{sp}d/\pi = 3.85$ with real (blue) and imaginary (red dashed) parts. b) The same bands zoomed in on the right exceptional point with the 0^{th} order approximation of the eigenvalues in yellow dashed lines, for real parts and green dotted lines for imaginary parts.

It is a little easier to see why this is from the eigenvalues of the Hamiltonian, given by

$$\mathcal{E}^0(k_{sp}, q_x)^2 = 4\,\mathrm{arctanh}^2\left(e^{i(k_{sp}d+q_x d)/2}\right) + 4\,\mathrm{arctanh}^2\left(e^{i(k_{sp}d-q_x d)/2}\right) + 8\cos(2k_{sp}d\Delta\beta)\,\mathrm{arctanh}\left(e^{i(k_{sp}d+q_x d)/2}\right)\mathrm{arctanh}\left(e^{i(k_{sp}d-q_x d)/2}\right). \tag{5.24}$$

We see that the eigenvalues are real in a region of q_x when the cosine is ± 1 with $2k_{sp}d\Delta\beta = n\pi$. We therefore have approximately real valued eigenvalues in the expected regions when $k_{sp}d\Delta\beta$ is chosen so that the cosine is nearly ± 1, or more specifically when $(2k_{sp}d\Delta\beta - n\pi)^2/2 \ll 1$. When the cosine is 0, with $2k_{sp}d\Delta\beta = (n+1/2)\pi$, the eigenvalues are furthest from the real case.

These results are visualised in figures 5.3(a)-(d), where the parameter $\chi = 2k_{sp}d\Delta\beta$ is used to measure the state of the system. Figure 5.3(a) shows the case where $\cos(\chi) \approx 1$, so that the system is similar to the $\beta = 1$ case. Figure 5.3(d) shows the opposite $\cos(\chi) \approx -1$, where the Hermitian and non-Hermitian regions of q_x are on opposite sides of the light line. Figures 5.3(b) and (c) show intermediate values, with figure 5.3(c) at $\cos(\chi) \approx 0$ the furthest from the two instances with real eigenvalues. Figure 5.3(b) also includes the real (yellow dashed) and imaginary (green dotted) parts of $\mathcal{E}^0$, the 0^{th} order approximation for the bands. We see that this approximation works very well in this case.

In figure 4.8 we saw that the full SLS band structure for a specific choice of $\beta = 1.4$, $k_{sp}d = 0.68\pi$ features eigenvalues which are approximately real valued outside of the light line. For these parameters, $\cos(\chi) = 0.66$ (2s.f.), which seems to contradict the results above. However, the value of β is large enough that the small $\Delta\beta$ approximation is not valid.

Figure 5.4(a) shows the bands at a retardation-induced phase transition $\beta = 1.08$, $k_{sp}d/\pi = 3.85$. There is an exceptional point in the matrix $\mathcal{M}$ for a specific q_x value where the phase transition occurs, where the eigenvalues go from approximately real valued to an imaginary pair. This is very similar to the $\mathcal{PT}$ unbroken and broken phases discussed in chapter 1, and suggests the presence of a pseudo-Hermitian symmetry of the matrix in q_x. Overlaid on figure 5.4(b) is the 0^{th} order approximation described in equation 5.21. Although this level of approximation worked well away from exceptional points, as evidenced by figure 5.3(b), it does not properly describe the exceptional point. It is therefore necessary to consider at least the 1^{st} order expansion to examine this phenomenon.

5.3.3 Further comments

It is also possible to examine band structures for β further from one, but we no longer have the benefit of a small perturbation from a simple function to guide insight. The Lerch transcendent is a tricky beast to tame, and even the first order perturbation in equation 5.21 features a Lerch transcendent which can no longer be written in terms of arctanh, but rather the Legendre chi function. It is unclear that doing so would be of much benefit.

Although these band structures relate specifically to the minimal model, finding symmetry properties should help to better understand the full dipolar system. As we have seen in chapter 1 and throughout, symmetry properties of bulk Bloch Hamiltonians are extremely important in determining physical behaviour of the corresponding system.

5.4 SUMMARY

In this chapter, we have presented a minimal model which approximately replicates the Zak phase behaviour of the transverse polarisation of the topological plasmonic chain and any other similarly dipole-dipole interacting system. This includes a phase diagram for $0.5 \leqslant \beta \leqslant 1.5$ and $k_{sp}d/\pi \leqslant 10$, and some symmetry properties of the phase diagram which can help to locate other phase transitions. In addition, we have provided preliminary studies of the band structure of the minimal model in an effort to understand symmetry properties of the full system a little better. These include simplifications of the, otherwise rather opaque, Lerch transcendent functions for $\beta = 1$ and $\beta = 1 + 2\Delta\beta$, where $\Delta\beta$ is small.

6 CONCLUSION

Over the course of this thesis we have studied the staggered chain of metallic nanoparticles, a system which exhibits many exciting topological properties. All of these are the result of the way light interacts with small metallic particles and propagates through space, combined with the geometry of the system. These simple ingredients led to a realistic system which exhibits topological protection, BEC breakdown, and surprising non-Hermitian phase transitions.

In chapter 1, we provided an accessible overview of TIs, including its photonic and non-Hermitian branches. This provides essential context for the research presented in later chapters, and also acts as a potential introductory resource for anyone entering the exciting and rewarding field of TIs. Chapter 2 builds on this, with greater focus on the applicable theory for the topological plasmonic chain, including details on the interaction of light with small particles. The SSH model description could also provide a useful basis for any new student of TIs.

Chapter 3 provided the first results on the staggered chain, using full dipolar Green's functions to present band structures and Zak phase calculations for both the longitudinal and transverse polarisation of the chain. For the longitudinal modes, the chain has topologically protected plasmonic hotspots, which exist at the edges of chains with non-trivial topology and at the interface of two chains with opposite Zak phase. We saw that they are protected from positional disorder in the axis of the chain. The chapter also introduced some preliminary work on extinction cross sections of the topological chain, which could be expanded upon to provide even more insight.

The next chapters focused on the transverse polarisation, which exhibits many surprising results compared to the longitudinal case. To simplify calculations, we used a linearised Green's function treatment. In chapter 4, we saw that the system exhibits a breakdown in BEC. This is not due to the non-Hermitian skin effect but rather the breaking of SLS by dipole-dipole interactions on the same sublattice which grow large as the spacing of the chain increased. We characterised this SLS breaking by comparing the system to a non-Hermitian NNN extension of the SSH model. This led to a measure of the SLS breaking which uses the Bloch bands in its calculation.

Closely related to the BEC breakdown are the retardation-induced phase transitions. These occur at exceptional points in the Hamiltonian of the staggered chain, and are therefore non-Hermitian by nature. Although first highlighted in chapter 3, and noted in chapter 4, they receive a more complete treatment in chapter 5. These phase transitions are caused by very slowly decaying terms in the dipole-dipole interaction, a fact used to motivate a minimal model; a system with simplest possible mathematics that closely mimics the phases of the transverse polarisation of the chain. Using this, we constructed a phase diagram and presented preliminary results on the properties of the minimal model band structure, which could be useful for the study of extremely long range hopping in non-Hermitian systems, like our topological plasmonic chain.

At the time of writing, the possibility of lasing using the edge states of the system is already being explored. We also saw that some results in the thesis have provided mathematical tools and motivation to others studying similar dipole-dipole interacting topological systems, and may continue to do so. This is a small but much appreciated validation of many hours spent studying this beautiful, intriguing system. It has been the author's privilege to contribute to the wider field of TIs in this way.

REFERENCES

[1] S. R. Pocock, X. Xiao, P. A. Huidobro, and V. Giannini, "Topological plasmonic chain with retardation and radiative effects", ACS Photonics **5**, 2271–2279 (2018).

[2] M. He, H. Sun, and Q. L. He, "Topological insulator: spintronics and quantum computations", Frontiers of Physics **14**, 43401 (2019).

[3] S. Zou and G. C. Schatz, "Theoretical studies of plasmon resonances in one-dimensional nanoparticle chains: narrow lineshapes with tunable widths", Nanotechnology **17**, 2813–2820 (2006).

[4] P. St-Jean, V. Goblot, E. Galopin, A. Lemaître, T. Ozawa, L. Le Gratiet, I. Sagnes, J. Bloch, and A. Amo, "Lasing in topological edge states of a one-dimensional lattice", Nature Photonics **11**, 651–656 (2017).

[5] H. T. Rekola, T. K. Hakala, and P. Törmä, "One-dimensional plasmonic nanoparticle chain lasers", ACS Photonics **5**, 1822–1826 (2018).

[6] F. J. G. de Abajo, "Colloquium: light scattering by particle and hole arrays", Rev. Mod. Phys. **79**, 1267–1290 (2007).

[7] B. Auguié and W. L. Barnes, "Collective resonances in gold nanoparticle arrays", Phys. Rev. Lett. **101**, 143902 (2008).

[8] S. J. Barrow, D. Rossouw, A. M. Funston, G. A. Botton, and P. Mulvaney, "Mapping bright and dark modes in gold nanoparticle chains using electron energy loss spectroscopy.", Nano Lett. **14**, 3799–3808 (2014).

[9] L. Wang, R. Y. Zhang, M. Xiao, D. Han, C. T. Chan, and W. Wen, "The existence of topological edge states in honeycomb plasmonic lattices", New J. Phys. **18**, 103029 (2016).

[10] J. R. Hook and H. E. Hall, *Solid state physics*, 2nd ed. (John Wiley & Sons, 1991).

[11] M. Z. Hasan and C. L. Kane, "Colloquium: topological insulators", Rev. Mod. Phys. **82**, 3045–3067 (2010).

[12] X.-L. Qi and S.-C. Zhang, "Topological insulators and superconductors", Rev. Mod. Phys. **83**, 1057–1110 (2011).

[13] S.-Q. Shen, "The family of topological phases in condensed matter", National Science Review **1**, 49–59 (2013).

[14] L. Lu, J. D. Joannopoulos, and M. Soljačić, "Topological states in photonic systems", Nature Physics **12**, 626 (2016).

[15] Y. Wu, C. Li, X. Hu, Y. Ao, Y. Zhao, and Q. Gong, "Applications of topological photonics in integrated photonic devices", Advanced Optical Materials **5**, 1700357 (2017).

[16] T. Ozawa, H. M. Price, A. Amo, N. Goldman, M. Hafezi, L. Lu, M. C. Rechtsman, D. Schuster, J. Simon, O. Zilberberg, and I. Carusotto, "Topological photonics", Rev. Mod. Phys. **91**, 015006 (2019).

[17]K. v. Klitzing, G. Dorda, and M. Pepper, "New method for high-accuracy determination of the fine-structure constant based on quantized hall resistance", Phys. Rev. Lett. **45**, 494–497 (1980).

[18]K. von Klitzing, "The quantized hall effect", Rev. Mod. Phys. **58**, 519–531 (1986).

[19]E. H. Hall, "On a new action of the magnet on electric currents", American Journal of Mathematics **2**, 287–292 (1879).

[20]T. J. B. M. Janssen, J. M. Williams, N. E. Fletcher, R. Goebel, A. Tzalenchuk, R. Yakimova, S. Lara-Avila, S. Kubatkin, and V. I. Fal'ko, "Precision comparison of the quantum hall effect in graphene and gallium arsenide", Metrologia **49**, 294–306 (2012).

[21]M. Büttiker, "Absence of backscattering in the quantum hall effect in multiprobe conductors", Phys. Rev. B **38**, 9375–9389 (1988).

[22]J. Schurr, *The quantum hall resistance*, (2016) `https://www.ptb.de/cms/en/ptb/fachabteilungen/abt2/fb-26/ag-262/the-quantum-hall-resistance.html` (visited on 06/13/2019).

[23]F. D. M. Haldane, "Nobel lecture: topological quantum matter", Rev. Mod. Phys. **89**, 040502 (2017).

[24]D. J. Thouless, M. Kohmoto, M. P. Nightingale, and M. den Nijs, "Quantized hall conductance in a two-dimensional periodic potential", Phys. Rev. Lett. **49**, 405–408 (1982).

[25]D. R. Hofstadter, "Energy levels and wave functions of Bloch electrons in rational and irrational magnetic fields", Phys. Rev. B **14**, 2239–2249 (1976).

[26]B. Simon, "Holonomy, the quantum adiabatic theorem, and berry's phase", Phys. Rev. Lett. **51**, 2167–2170 (1983).

[27]M. Kohmoto, "Topological invariant and the quantization of the hall conductance", Ann. Phys. **160**, 343–354 (1985).

[28]Y. Hatsugai, "Edge states in the integer quantum hall effect and the riemann surface of the bloch function", Phys. Rev. B **48**, 11851–11862 (1993).

[29]Y. Hatsugai, "Chern number and edge states in the integer quantum hall effect", Phys. Rev. Lett. **71**, 3697–3700 (1993).

[30]D. C. Tsui, H. L. Stormer, and A. C. Gossard, "Two-dimensional magnetotransport in the extreme quantum limit", Phys. Rev. Lett. **48**, 1559–1562 (1982).

[31]R. B. Laughlin, "Anomalous quantum hall effect: an incompressible quantum fluid with fractionally charged excitations", Phys. Rev. Lett. **50**, 1395–1398 (1983).

[32]J. P. Eisenstein and H. L. Stormer, "The fractional quantum hall effect", Science **248**, 1510–1516 (1990).

[33]J. Martin, S. Ilani, B. Verdene, J. Smet, V. Umansky, D. Mahalu, D. Schuh, G. Abstreiter, and A. Yacoby, "Localization of fractionally charged quasi-particles", Science **305**, 980–983 (2004).

[34]E. H. Hall, "On the rotational coefficient in nickel and cobalt", Philos. Mag. **12**, 157–172 (1881).

[35]K. S. Novoselov, A. K. Geim, S. V. Morozov, D. Jiang, Y. Zhang, S. V. Dubonos, I. V. Grigorieva, and A. A. Firsov, "Electric field effect in atomically thin carbon films", Science **306**, 666–669 (2004).

[36]Y. Aharonov and D. Bohm, "Significance of electromagnetic potentials in the quantum theory", Phys. Rev. **115**, 485–491 (1959).

[37]K. Ohgushi, S. Murakami, and N. Nagaosa, "Spin anisotropy and quantum hall effect in the kagomé lattice: chiral spin state based on a ferromagnet", Phys. Rev. B **62**, R6065–R6068 (2000).

[38]C.-X. Liu, X.-L. Qi, X. Dai, Z. Fang, and S.-C. Zhang, "Quantum anomalous hall effect in $Hg_{1-y}Mn_yTe$ quantum wells", Phys. Rev. Lett. **101**, 146802 (2008).

[39]R. Yu, W. Zhang, H.-J. Zhang, S.-C. Zhang, X. Dai, and Z. Fang, "Quantized anomalous hall effect in magnetic topological insulators", Science **329**, 61–64 (2010).

[40]C.-Z. Chang, J. Zhang, X. Feng, J. Shen, Z. Zhang, M. Guo, K. Li, Y. Ou, P. Wei, L.-L. Wang, Z.-Q. Ji, Y. Feng, S. Ji, X. Chen, J. Jia, X. Dai, Z. Fang, S.-C. Zhang, K. He, Y. Wang, L. Lu, X.-C. Ma, and Q.-K. Xue, "Experimental observation of the quantum anomalous hall effect in a magnetic topological insulator", Science **340**, 167–170 (2013).

[41]C. L. Kane and E. J. Mele, "Z2 topological order and the quantum spin hall effect", Phys. Rev. Lett. **95**, 146802 (2005).

[42]C. L. Kane and E. J. Mele, "Quantum spin hall effect in graphene", Phys. Rev. Lett. **95**, 226801 (2005).

[43]B. A. Bernevig, T. L. Hughes, and S.-C. Zhang, "Quantum spin hall effect and topological phase transition in HgTe quantum wells", Science **314**, 1757–1761 (2006).

[44]N. M. A. 2019, *The nobel prize in physics 2016*, (2016) https://www.nobelprize.org/prizes/physics/2016/summary/ (visited on 06/20/2019).

[45]N. M. A. 2019, *The nobel prize in physics 1985*, (1985) https://www.nobelprize.org/prizes/physics/1985/summary/ (visited on 06/20/2019).

[46]J. K. Asbóth, L. Oroszlány, and A. Pályi, *A short course on topological insulators, Band structure and edge states in one and two dimensions* (Springer International Publishing, Switzerland, 2016).

[47]R. Jackiw and C. Rebbi, "Solitons with fermion number 1/2", Phys. Rev. D **13**, 3398–3409 (1976).

[48]W. P. Su, J. R. Schrieffer, and A. J. Heeger, "Solitons in polyacetylene", Phys. Rev. Lett. **42**, 1698–1701 (1979).

[49]J. E. Moore and L. Balents, "Topological invariants of time-reversal-invariant band structures", Phys. Rev. B **75**, 121306 (2007).

[50]L. Fu, C. L. Kane, and E. J. Mele, "Topological insulators in three dimensions", Phys. Rev. Lett. **98**, 106803 (2007).

[51]R. Roy, "Topological phases and the quantum spin hall effect in three dimensions", Phys. Rev. B **79**, 195322 (2009).

[52]M. Z. Hasan and J. E. Moore, "Three-dimensional topological insulators", Annual Review of Condensed Matter Physics **2**, 55–78 (2011).

[53]A. Kitaev, "Periodic table for topological insulators and superconductors", AIP Conference Proceedings **1134**, 22–30 (2009).

[54]S. Ryu, A. P. Schnyder, A. Furusaki, and A. W. W. Ludwig, "Topological insulators and superconductors: tenfold way and dimensional hierarchy", New Journal of Physics **12**, 065010 (2010).

[55]A. P. Schnyder, S. Ryu, A. Furusaki, and A. W. W. Ludwig, "Classification of topological insulators and superconductors in three spatial dimensions", Phys. Rev. B **78**, 195125 (2008).

[56]A. Altland and M. R. Zirnbauer, "Nonstandard symmetry classes in mesoscopic normal-superconducting hybrid structures", Phys. Rev. B **55**, 1142–1161 (1997).

[57]A. Schnyder, S. Ryu, A. Furusaki, and A. W. W. Ludwig, "Classification of topological insulators and superconductors", AIP Conference Proceedings **1134**, 10 (2009).

[58]X. Zhang, M. Xiao, Y. Cheng, M.-H. Lu, and J. Christensen, "Topological sound", Communications Physics **1**, 97 (2018).

[59]L. Lu, J. D. Joannopoulos, and M. Soljačić, "Topological photonics", Nature Photonics **8**, 821 (2014).

[60]X.-C. Sun, C. He, X.-P. Liu, M.-H. Lu, S.-N. Zhu, and Y.-F. Chen, "Two-dimensional topological photonic systems", Progress in Quantum Electronics **55**, 52–73 (2017).

[61]M. S. Rider, S. J. Palmer, S. R. Pocock, X. Xiao, P. Arroyo Huidobro, and V. Giannini, "A perspective on topological nanophotonics: current status and future challenges", Journal of Applied Physics **125**, 120901 (2019).

[62]A. Yang, A. J. Hryn, M. R. Bourgeois, W.-K. Lee, J. Hu, G. C. Schatz, and T. W. Odom, "Programmable and reversible plasmon mode engineering", PNAS **113**, 14201–14206 (2016).

[63]E. Yablonovitch, "Inhibited spontaneous emission in solid-state physics and electronics", Phys. Rev. Lett. **58**, 2059–2062 (1987).

[64]S. John, "Strong localization of photons in certain disordered dielectric superlattices", Phys. Rev. Lett. **58**, 2486–2489 (1987).

[65]S. Y. Lin, J. G. Fleming, D. L. Hetherington, B. K. Smith, R. Biswas, K. M. Ho, M. M. Sigalas, W. Zubrzycki, S. R. Kurtz, and J. Bur, "A three-dimensional photonic crystal operating at infrared wavelengths", Nature **394**, 251–253 (1998).

[66]E. Yablonovitch and T. J. Gmitter, "Photonic band structure: the face-centered-cubic case", Phys. Rev. Lett. **63**, 1950–1953 (1989).

[67]K. M. Ho, C. T. Chan, and C. M. Soukoulis, "Existence of a photonic gap in periodic dielectric structures", Phys. Rev. Lett. **65**, 3152–3155 (1990).

[68]F. D. M. Haldane and S. Raghu, "Possible realization of directional optical waveguides in photonic crystals with broken time-reversal symmetry", Phys. Rev. Lett. **100**, 013904 (2008).

[69]S. Raghu and F. D. M. Haldane, "Analogs of quantum-hall-effect edge states in photonic crystals", Phys. Rev. A **78**, 033834 (2008).

[70]Z. Wang, Y. D. Chong, J. D. Joannopoulos, and M. Soljačić, "Reflection-free one-way edge modes in a gyromagnetic photonic crystal", Phys. Rev. Lett. **100**, 013905 (2008).

[71]Y. D. Chong, X.-G. Wen, and. Solja či ć, "Effective theory of quadratic degeneracies", Phys. Rev. B **77**, 235125 (2008).

[72]Z. Wang, Y. Chong, J. D. Joannopoulos, and M. Soljačić, "Observation of unidirectional backscattering-immune topological electromagnetic states", Nature **461**, 772 (2009).

[73]M. C. Rechtsman, J. M. Zeuner, Y. Plotnik, Y. Lumer, D. Podolsky, F. Dreisow, S. Nolte, M. Segev, and A. Szameit, "Photonic floquet topological insulators", Nature **496**, 196 (2013).

[74]A. B. Khanikaev, S. H. Mousavi, W.-K. Tse, M. Kargarian, A. H. MacDonald, and G. Shvets, "Photonic topological insulators", Nat. Materials **12**, 233–239 (2013).

[75]L.-H. Wu and X. Hu, "Scheme for achieving a topological photonic crystal by using dielectric material", Phys. Rev. Lett. **114**, 223901 (2015).

[76]Y. Yang, Y. F. Xu, T. Xu, H.-X. Wang, J.-H. Jiang, X. Hu, and Z. H. Hang, "Visualization of a unidirectional electromagnetic waveguide using topological photonic crystals made of dielectric materials", Phys. Rev. Lett. **120**, 217401 (2018).

[77]A. Szameit and S. Nolte, "Discrete optics in femtosecond-laser-written photonic structures", Journal of Physics B: Atomic, Molecular and Optical Physics **43**, 163001 (2010).

[78]A. Slobozhanyuk, A. V. Shchelokova, X. Ni, S. Hossein Mousavi, D. A. Smirnova, P. A. Belov, A. Alù, Y. S. Kivshar, and A. B. Khanikaev, "Near-field imaging of spin-locked edge states in all-dielectric topological metasurfaces", Applied Physics Letters **114**, 031103 (2019).

[79]J.-W. Dong, X.-D. Chen, H. Zhu, Y. Wang, and X. Zhang, "Valley photonic crystals for control of spin and topology", Nature Materials **16**, 298 (2017).

[80]J. Noh, S. Huang, K. P. Chen, and M. C. Rechtsman, "Observation of photonic topological valley hall edge states", Phys. Rev. Lett. **120**, 063902 (2018).

[81]M. Xiao, Z. Q. Zhang, and C. T. Chan, "Surface impedance and bulk band geometric phases in one-dimensional systems", Phys. Rev. X **4**, 021017 (2014).

[82]A. P. Slobozhanyuk, A. N. Poddubny, A. E. Miroshnichenko, P. A. Belov, and Y. S. Kivshar, "Subwavelength topological edge states in optically resonant dielectric structures", Phys. Rev. Lett. **114**, 123901 (2015).

[83]D. D. Solnyshkov, A. V. Nalitov, and G. Malpuech, "Kibble-zurek mechanism in topologically nontrivial zigzag chains of polariton micropillars", Phys. Rev. Lett. **116**, 046402 (2016).

[84]S. A. Maier, *Plasmonics: fundamentals and applications*, 1st ed. (Springer US, 2007).

[85]K. Y. Bliokh, D. Smirnova, and F. Nori, "Quantum spin Hall effect of light", Science **348**, 1448–1451 (2015).

[86]D. Jin, T. Christensen, M. Soljačić, N. X. Fang, L. Lu, and X. Zhang, "Infrared topological plasmons in graphene", Phys. Rev. Lett. **118**, 245301 (2017).

[87]S. Yves, R. Fleury, T. Berthelot, M. Fink, F. Lemoult, and G. Lerosey, "Crystalline metamaterials for topological properties at subwavelength scales", Nature Communications **8**, 16023 (2017).

[88]Creative Commons, *CC BY 4.0*, https://creativecommons.org/licenses/by/4.0/legalcode [accessed 11-10-2019].

[89]V. Giannini, A. I. Fernández-Domínguez, S. C. Heck, and S. A. Maier, "Plasmonic nanoantennas: fundamentals and their use in controlling the radiative properties of nanoemitters", Chem. Rev. **111**, 3888–3912 (2011).

[90]B. S. Hoener, S. R. Kirchner, T. S. Heiderscheit, S. S. Collins, W.-S. Chang, S. Link, and C. F. Landes, "Plasmonic sensing and control of single-nanoparticle electrochemistry", Chem **4**, 1560–1585 (2018).

[91]R. Bardhan, W. Chen, C. Perez-Torres, M. Bartels, R. M. Huschka, L. L. Zhao, E. Morosan, R. G. Pautler, A. Joshi, and N. J. Halas, "Nanoshells with targeted simultaneous enhancement of magnetic and optical imaging and photothermal therapeutic response", Advanced Functional Materials **19**, 3901–3909 (2009).

[92]Y. B. Zheng, B. Kiraly, P. S. Weiss, and T. J. Huang, "Molecular plasmonics for biology and nanomedicine", Nanomedicine **7**, 751–770 (2012).

[93]C. Hrelescu, T. K. Sau, A. L. Rogach, F. Jäckel, and J. Feldmann, "Single gold nanostars enhance raman scattering", Applied Physics Letters **94**, 153113 (2009).

[94]X. Wu, Y. Meng, J. Tian, Y. Huang, H. Xiang, D. Han, and W. Wen, "Direct observation of valley-polarized topological edge states in designer surface plasmon crystals", Nature Communications **8**, 1304 (2017).

[95]A. Poddubny, A. Miroshnichenko, A. Slobozhanyuk, and Y. Kivshar, "Topological majorana states in zigzag chains of plasmonic nanoparticles", ACS Photonics **1**, 101–105 (2014).

[96]C. W. Ling, M. Xiao, C. T. Chan, S. F. Yu, and K. H. Fung, "Topological edge plasmon modes between diatomic chains of plasmonic nanoparticles", Opt. Express **23**, 2021–2031 (2015).

[97]D. E. Gómez, Y. Hwang, J. Lin, T. J. Davis, and A. Roberts, "Plasmonic edge states: an electrostatic eigenmode description", ACS Photonics **4**, 1607–1614 (2017).

[98]N. Moiseyev, *Non-Hermitian quantum mechanics* (Cambridge University Press, Cambridge, 2011).

[99]C. M. Bender and S. Boettcher, "Real spectra in non-Hermitian Hamiltonians having $\mathcal{PT}$ symmetry", Phys. Rev. Lett. **80**, 5243–5246 (1998).

[100]I. Rotter, "A non-Hermitian Hamilton operator and the physics of open quantum systems", Journal of Physics A: Mathematical and Theoretical **42**, 153001 (2009).

[101]L. Feng, R. El-Ganainy, and L. Ge, "Non-Hermitian photonics based on parity–time symmetry", Nature Photonics **11**, 752–762 (2017).

[102]S. Longhi, "Parity-time symmetry meets photonics: a new twist in non-Hermitian optics", EPL (Europhysics Letters) **120**, 64001 (2018).

[103]B. Midya, H. Zhao, and L. Feng, "Non-Hermitian photonics promises exceptional topology of light", Nature Communications **9**, 2674 (2018).

[104]V. M. Martinez Alvarez, J. E. Barrios Vargas, M. Berdakin, and L. E. F. Foa Torres, "Topological states of non-Hermitian systems", The European Physical Journal Special Topics **227**, 1295–1308 (2018).

[105]K. Kawabata, K. Shiozaki, M. Ueda, and M. Sato, "Symmetry and topology in non-hermitian physics", Phys. Rev. X **9**, 041015 (2019).

[106]H. Zhou and J. Y. Lee, "Periodic table for topological bands with non-hermitian symmetries", Phys. Rev. B **99**, 235112 (2019).

[107]W. Heiss and H. Harney, "The chirality of exceptional points", The European Physical Journal D - Atomic, Molecular, Optical and Plasma Physics **17**, 149–151 (2001).

[108]W. Heiss, Czechoslovak Journal of Physics **54**, 1091–1099 (2004).

[109]L. Feng, Z. J. Wong, R.-M. Ma, Y. Wang, and X. Zhang, "Single-mode laser by parity-time symmetry breaking", Science **346**, 972–975 (2014).

[110]Z. Lin, H. Ramezani, T. Eichelkraut, T. Kottos, H. Cao, and D. N. Christodoulides, "Unidirectional invisibility induced by $\mathcal{PT}$-symmetric periodic structures", Phys. Rev. Lett. **106**, 213901 (2011).

[111]W. Chen, Ş. Kaya Özdemir, G. Zhao, J. Wiersig, and L. Yang, "Exceptional points enhance sensing in an optical microcavity", Nature **548**, 192 (2017).

[112]K. Esaki, M. Sato, K. Hasebe, and M. Kohmoto, "Edge states and topological phases in non-Hermitian systems", Phys. Rev. B **84**, 205128 (2011).

[113]S. Lieu, "Topological symmetry classes for non-Hermitian models and connections to the bosonic Bogoliubov–de Gennes equation", Phys. Rev. B **98**, 115135 (2018).

[114]Z. Gong, Y. Ashida, K. Kawabata, K. Takasan, S. Higashikawa, and M. Ueda, "Topological phases of non-Hermitian systems", Phys. Rev. X **8**, 031079 (2018).

[115]H. Shen, B. Zhen, and L. Fu, "Topological band theory for non-Hermitian Hamiltonians", Phys. Rev. Lett. **120**, 146402 (2018).

[116]Y. Xiong, "Why does bulk boundary correspondence fail in some non-Hermitian topological models", Journal of Physics Communications **2**, 035043 (2018).

[117]L. Jin and Z. Song, "Bulk-boundary correspondence in a non-Hermitian system in one dimension with chiral inversion symmetry", Phys. Rev. B **99**, 081103 (2019).

[118]R. Chen, C.-Z. Chen, B. Zhou, and D.-H. Xu, "Finite-size effects in non-Hermitian topological systems", Phys. Rev. B **99**, 155431 (2019).

[119]S. Yao and Z. Wang, "Edge states and topological invariants of non-Hermitian systems", Phys. Rev. Lett. **121**, 086803 (2018).

[120]F. K. Kunst, E. Edvardsson, J. C. Budich, and E. J. Bergholtz, "Biorthogonal bulk-boundary correspondence in non-Hermitian systems", Phys. Rev. Lett. **121**, 026808 (2018).

[121]C. H. Lee and R. Thomale, "Anatomy of skin modes and topology in non-hermitian systems", Phys. Rev. B **99**, 201103 (2019).

[122]L. Herviou, J. H. Bardarson, and N. Regnault, "Defining a bulk-edge correspondence for non-Hermitian Hamiltonians via singular-value decomposition", Phys. Rev. A **99**, 052118 (2019).

[123]J. Zak, "Berry's phase for energy bands in solids", Phys. Rev. Lett. **62**, 2747–2750 (1989).

[124]C. Yin, H. Jiang, L. Li, R. Lü, and S. Chen, "Geometrical meaning of winding number and its characterization of topological phases in one-dimensional chiral non-hermitian systems", Phys. Rev. A **97**, 052115 (2018).

[125]B.-H. Chen and D.-W. Chiou, "A rigorous proof of bulk-boundary correspondence in the generalized Su-Schrieffer-Heeger model", arXiv e-prints, arXiv:1705.06913, arXiv:1705.06913 (2017).

[126]L. Li, Z. Xu, and S. Chen, "Topological phases of generlized Su-Schrieffer-Heeger models", Phys. Rev. B **89**, 085111 (2014).

[127]B. Pérez-González, M. Bello, Á. Gómez-León, and G. Platero, "Interplay between long-range hopping and disorder in topological systems", Phys. Rev. B **99**, 035146 (2019).

[128]P. Delplace, D. Ullmo, and G. Montambaux, "Zak phase and the existence of edge states in graphene", Phys. Rev. B **84**, 195452 (2011).

[129]F. Liu and K. Wakabayashi, "Novel topological phase with a zero berry curvature", Phys. Rev. Lett. **118**, 076803 (2017).

[130]M. S. Rudner and L. S. Levitov, "Topological transition in a non-hermitian quantum walk", Phys. Rev. Lett. **102**, 065703 (2009).

[131]S. Malzard, C. Poli, and H. Schomerus, "Topologically protected defect states in open photonic systems with non-Hermitian charge-conjugation and parity-time symmetry", Phys. Rev. Lett. **115**, 200402 (2015).

[132]S. Lieu, "Topological phases in the non-Hermitian Su-Schrieffer-Heeger model", Phys. Rev. B **97**, 045106 (2018).

[133]B. Zhu, R. Lü, and S. Chen, "Pt symmetry in the non-Hermitian Su-Schrieffer-Heeger model with complex boundary potentials", Phys. Rev. A **89**, 062102 (2014).

[134]X. Z. Zhang and Z. Song, "Partial topological zak phase and dynamical confinement in a non-Hermitian bipartite system", Phys. Rev. A **99**, 012113 (2019).

[135]Z.-Z. Li, X.-S. Li, L.-L. Zhang, and W.-J. Gong, *$\mathcal{PT}$ symmetry of the Su-Schrieffer-Heeger model with imaginary boundary potentials and next-nearest-neighboring coupling*, arXiv:1901.10688, 2019.

[136]M. Atala, M. Aidelsburger, J. T. Barreiro, D. Abanin, T. Kitagawa, E. Demler, and I. Bloch, "Direct measurement of the zak phase in topological bloch bands", Nature Physics **9**, 795 (2013).

[137]I. S. Sinev, I. S. Mukhin, A. P. Slobozhanyuk, A. N. Poddubny, A. E. Miroshnichenko, A. K. Samusev, and Y. S. Kivshar, "Mapping plasmonic topological states at the nanoscale", Nanoscale **7**, 11904–11908 (2015).

[138]H. Schomerus, "Topologically protected midgap states in complex photonic lattices", Opt. Lett. **38**, 1912–1914 (2013).

[139]J. M. Zeuner, M. C. Rechtsman, Y. Plotnik, Y. Lumer, S. Nolte, M. S. Rudner, M. Segev, and A. Szameit, "Observation of a topological transition in the bulk of a non-hermitian system", Phys. Rev. Lett. **115**, 040402 (2015).

[140]F. Bleckmann, Z. Cherpakova, S. Linden, and A. Alberti, "Spectral imaging of topological edge states in plasmonic waveguide arrays", Phys. Rev. B **96**, 045417 (2017).

[141]M. Pan, H. Zhao, P. Miao, S. Longhi, and L. Feng, "Photonic zero mode in a non-hermitian photonic lattice", Nature Communications **9**, 1308 (2018).

[142]C. A. Downing and G. Weick, "Topological plasmons in dimerized chains of nanoparticles: robustness against long-range quasistatic interactions and retardation effects", ArXiv e-prints (2018).

[143]C. A. Downing, E. Mariani, and G. Weick, "Retardation effects on the dispersion and propagation of plasmons in metallic nanoparticle chains", J. Phy. Condens. Matter **30**, 025301 (2018).

[144]I. Freestone, N. Meeks, M. Sax, and C. Higgitt, "The lycurgus cup — a roman nanotechnology", Gold Bulletin **40**, 270–277 (2007).

[145]J. W. Strutt, "On the scattering of light by small particles", The London, Edinburgh, and Dublin Philosophical Magazine and Journal of Science **41**, 447–454 (1871).

[146]M. Kerker, *The scattering of light and other electromagnetic radiation: physical chemistry: a series of monographs*, Vol. 16 (Academic press, 2013).

[147]G. Mie, "Beiträge zur optik trüber medien, speziell kolloidaler metallösungen", Annalen der Physik **330**, 377–445 (1908).

[148]C. F. Bohren and D. R. Huffman, *Absorption and scattering of light by small particles* (John Wiley & Sons, 2008).

[149]D. Tzarouchis and A. Sihvola, "Light scattering by a dielectric sphere: perspectives on the Mie resonances", Applied Sciences **8** (2018).

[150]S. Y. Park and D. Stroud, "Surface-plasmon dispersion relations in chains of metallic nanoparticles: an exact quasistatic calculation", Phys. Rev. B **69**, 125418 (2004).

[151]L. Novotny and B. Hecht, *Principles of nano-optics* (Cambridge university press, 2012).

[152]K. L. Kelly, E. Coronado, L. L. Zhao, and G. C. Schatz, "The optical properties of metal nanoparticles: the influence of size, shape, and dielectric environment", The Journal of Physical Chemistry B **107**, 668–677 (2003).

[153]A. Moroz, "Depolarization field of spheroidal particles", J. Opt. Soc. Am. B **26**, 517–527 (2009).

[154]M. Meier and A. Wokaun, "Enhanced fields on large metal particles: dynamic depolarization", Opt. Lett. **8**, 581–583 (1983).

[155]K. Markowicz, *Radiative codes*, (2007) `http://www.igf.fuw.edu.pl/~kmark/stacja/kody.php` (visited on 01/16/2020).

[156]H. U. Yang, J. D'Archangel, M. L. Sundheimer, E. Tucker, G. D. Boreman, and 3. B. Raschke, "Optical dielectric function of silver", Phys. Rev. B **91**, 235137 (2015).

[157]V. Markel, "Coupled-dipole approach to scattering of light from a one-dimensional periodic dipole structure", Journal of Modern Optics **40**, 2281–2291 (1993).

[158]S. A. Maier, P. G. Kik, H. A. Atwater, S. Meltzer, E. Harel, B. E. Koel, and A. A. Requicha, "Local detection of electromagnetic energy transport below the diffraction limit in metal nanoparticle plasmon waveguides", Nature materials **2**, 229 (2003).

[159]S. Zou, N. Janel, and G. C. Schatz, "Silver nanoparticle array structures that produce remarkably narrow plasmon lineshapes", The Journal of Chemical Physics **120**, 10871–10875 (2004).

[160]W. H. Weber and G. W. Ford, "Propagation of optical excitations by dipolar interacitons in metal nanoparticle chains", Phys. Rev. B **70**, 125429 (2004).

[161]R. A. Shore and A. D. Yaghjian, "Travelling electromagnetic waves on linear periodic arrays of lossless spheres", Electronics Letters **41**, 578–580 (2005).

[162]C. R. Simovski, A. J. Viitanen, and S. A. Tretyakov, "Resonator mode in chains of silver spheres and its possible application", Phys. Rev. E **72**, 066606 (2005).

[163]D. S. Citrin, "Plasmon-polariton transport in metal-nanoparticle chains embedded in a gain medium", Opt. Lett. **31**, 98–100 (2006).

[164]A. F. Koenderink and A. Polman, "Complex response and polariton-like dispersion splitting in periodic metal nanoparticle chains", Phys. Rev. B **74**, 033402 (2006).

[165]A. Vial, A.-S. Grimault, D. Macias, D. Barchiesi, and M. L. de la Chapelle, "Improved analytical fit of gold dispersion: application to the modeling of extinction spectra with a finite-difference time-domain method", Phys. Rev. B **71**, 085416 (2005).

[166]X. Zhu, C. Vannahme, E. Højlund-Nielsen, N. A. Mortensen, and A. Kristensen, "Plasmonic colour laser printing", Nat. Nanotechnol **11**, 325–329 (2015).

[167]M. B. Ross, C. A. Mirkin, and G. C. Schatz, "Optical properties of one-, two-, and three-dimensional arrays of plasmonic nanostructures", The Journal of Physical Chemistry C **120**, 816–830 (2016).

[168]P. Genevet, F. Capasso, F. Aieta, M. Khorasaninejad, and R. Devlin, "Recent advances in planar optics: from plasmonic to dielectric metasurfaces", Optica **4**, 139–152 (2017).

[169]P. J. Compaijen, V. A. Malyshev, and J. Knoester, "Surface-mediated light transmission in metal nanoparticle chains", Phys. Rev. B **87**, 205437 (2013).

[170]P. J. Compaijen, V. A. Malyshev, and J. Knoester, "Engineering plasmon dispersion relations: hybrid nanoparticle chain -substrate plasmon polaritons", Opt. Express **23**, 2280–2292 (2015).

[171]F. Todisco, M. Esposito, S. Panaro, M. De Giorgi, L. Dominici, D. Ballarini, A. I. Fernández-Domínguez, V. Tasco, M. Cuscunà, A. Passaseo, C. Ciracì, G. Gigli, and D. Sanvitto, "Toward cavity quantum electrodynamics with hybrid photon gap-plasmon states", ACS Nano **10**, 11360–11368 (2016).

[172]I. S. Gradshteyn, I. M. Ryzhik, A. Jeffrey, and D. Zwillinger, *Table of integrals, series and products, 7th edition* (Academic Press, US, 2007).

[173]A. Mostafazadeh, "A new class of adiabatic cyclic states and geometric phases for non-Hermitian Hamiltonians", Phys. Lett. A **264**, 11–17 (1999).

[174]G. van Miert, C. Ortix, and C. M. Smith, "Topological origin of edge states in two-dimensional inversion-symmetric insulators and semimetals", 2D Materials **4**, 015023 (2017).

[175]V. A. Markel and A. K. Sarychev, "Propagation of surface plasmons in ordered and disordered chains of metal nanospheres", Phys. Rev. B **75**, 085426 (2007).

[176]J. Le Gall, M. Olivier, and J.-J. Greffet, "Experimental and theoretical study of reflection and coherent thermal emissionby a sic grating supporting a surface-phonon polariton", Phys. Rev. B **55**, 10105–10114 (1997).

[177]P. B. Johnson and R. W. Christy, "Optical constants of the noble metals", Phys. Rev. B **6**, 4370–4379 (1972).

[178]L. Inc., *Simulation methodology*, (2018) https://kb.lumerical.com/en/index.html?diffractive_optics_pc_simulation_methodology.html (visited on 04/04/2018).

[179]L. Inc., *Simulations with loss*, (2018) https://kb.lumerical.com/en/diffractive_optics_pc_simulations_with_loss.html (visited on 04/04/2018).

[180]T. K. Hakala, H. T. Rekola, A. I. Väkeväinen, J.-P. Martikainen, M. Nečada, A. J. Moilanen, and P. Törmä, "Lasing in dark and bright modes of a finite-sized plasmonic lattice", Nat. Comm **8**, 13687 (2017).

[181]B. X. Wang and C. Y. Zhao, "Topological photonic states in one-dimensional dimerized ultracold atomic chains", Phys. Rev. A **98**, 023808 (2018).

[182]B. X. Wang and C. Y. Zhao, "Topological phonon polaritons in one-dimensional non-Hermitian silicon carbide nanoparticle chains", Phys. Rev. B **98**, 165435 (2018).

[183]R. P. H. Wu, Y. Zhang, K. F. Lee, J. Wang, S. F. Yu, and K. H. Fung, "Dynamic long range interaction induced topological edge modes in dispersive gyromagnetic lattices", Phys. Rev. B **99**, 214433 (2019).

[184]S. R. Pocock, P. A. Huidobro, and V. Giannini, "Bulk-edge correspondence and long-range hopping in the topological plasmonic chain", Nanophotonics **8**, 1337–1347 (2019).

[185]R. Resta, "Manifestations of Berry's phase in molecules and condensed matter", Journal of Physics: Condensed Matter **12**, R107–R143 (2000).

[186]L. Fu and C. L. Kane, "Topological insulators with inversion symmetry", Phys. Rev. B **76**, 045302 (2007).

[187]T. L. Hughes, E. Prodan, and B. A. Bernevig, "Inversion-symmetric topological insulators", Phys. Rev. B **83**, 245132 (2011).

[188]M. Bello, G. Platero, J. I. Cirac, and A. González-Tudela, "Unconventional quantum optics in topological waveguide qed", Science Advances **5** (2019).

[189]S. Kruk, A. Poddubny, D. Smirnova, L. Wang, A. Slobozhanyuk, A. Shorokhov, I. Kravchenko, B. Luther-Davies, and Y. Kivshar, "Nonlinear light generation in topological nanostructures", Nature Nanotechnology (2018).

[190]S. Peng, N. J. Schilder, X. Ni, J. van de Groep, M. L. Brongersma, A. Alù, A. B. Khanikaev, H. A. Atwater, and A. Polman, "Probing the band structure of topological silicon photonic lattices in the visible spectrum", Phys. Rev. Lett. **122**, 117401 (2019).